Università degli Studi di Milano-Bicocca

Dipartimento di Scienza dei Materiali

Ph.D. School in Nanostructures and Nanotechnologies

XXVI Cycle 2011-2013

Scanning Tunneling Microscopy Investigation of III-V Compound Semiconductors and Novel 2D Nanolattices

Tutor: Prof. Marco Fanciulli
Co-Tutor: Dr. Alessandro Molle
Coordinator: Prof. Gianfranco Pacchioni

Candidate:
Carlo Grazianetti
Matr. 744994

Milano, January 16th 2014

An online record is available on: www.boa.unimib.it

© 2013 Carlo Grazianetti and Laboratorio MDM (CNR-IMM)
All rights reserved. This work may not be translated or copied in whole or in part without the written permission of the author.

The candidate confirms that the work submitted is his own and that appropriate credit has been given where reference has been made to the work of others.

This thesis was typeset with LaTeXby the author.

To my family

There are more things in heaven and earth, Horatio,
than are dreamt of in your philosophy
Hamlet

Contents

1 Introduction **1**
1.1 Motivations and thesis outline 1
1.2 High-mobility materials for logic devices 3
1.3 III-V semiconductors 6
1.4 2D materials 8
1.5 Why use STM? 11

2 Scanning Tunneling Microscopy **17**
2.1 History 17
2.2 Principles of tunneling 18
2.3 STM - Operating principle 20
2.4 Topography: Surface structure 20
2.5 Spectroscopy: Electronic properties 22
2.6 Instrumental setup 24
2.6.1 The UHV system 24
2.6.2 Variable-temperature STM (VT-STM) 25
2.6.3 X-ray Photoelectron Spectroscopy 26
2.6.4 Raman Spectroscopy 27

3 InGaAs **33**
3.1 III-V semiconductors 33
3.2 $In_{0.53}Ga_{0.47}As$ (2×4) and (4×2) reconstructions 35
3.3 Chemical reactivity of $In_{0.53}Ga_{0.47}As$ surfaces 38
3.4 Al_2O_3 deposition by ALD 39
3.5 Al_2O_3 deposition by MBE 40
3.6 Effect of electric dipoles on Fermi level position 44
3.7 Conclusions 47

4 2D materials: overview **53**
4.1 From 3D to 2D materials 53
4.2 Flatland 54
4.3 Graphene 55
4.4 Beyond graphene 57

5 Silicene on Ag(111) **63**
5.1 Theoretical background 63
5.2 First experimental evidences 64
5.3 Morphological properties 65
5.4 Electronic properties 70
5.5 Chemical properties 76
5.6 Silicene encapsulation 78
5.7 Raman spectroscopy characterization 81
5.8 Conclusions and perspectives 87

6 Conclusions **95**

Publications **99**

Conferences **101**

Acknowledgements **103**

List of Tables

3.1 XPS core levels differences for $Al_2O_3/In_{0.53}Ga_{0.47}As$ interfaces 45

5.1 Silicene superstructures properties 70

List of Figures

1.1 MOSFET model 4

2.1 Tunnel effect in one dimension 19
2.2 STM schematic depiction 21
2.3 Tunneling process during STS and relationship to LDOS 24
2.4 UHV experimental setup 26
2.5 XPS process 27

3.1 STM of $In_{0.53}Ga_{0.47}As(001)$-$(2 \times 4)$ and (4×2) reconstructions 36
3.2 STS of $In_{0.53}Ga_{0.47}As(001)$–$(2 \times 4)$ and (4×2) reconstructions 38
3.3 XPS of air-exposed $In_{0.53}Ga_{0.47}As(001)$ 39
3.4 XPS of ALD-grown Al_2O_3 40
3.5 STM of Al_2O_3 on $In_{0.53}Ga_{0.47}As(001)$ 41
3.6 STS of $Al_2O_3/In_{0.53}Ga_{0.47}As$ interfaces 42
3.7 XPS of MBE-grown Al_2O_3 43
3.8 XPS core levels for VBO determination 46

5.1 STM of Ag(111) surface 66
5.2 STM images of three different Si coverages 67
5.3 Silicene superstructures 69
5.4 STM images of $(4/\sqrt{3} \times 4/\sqrt{3})$ superstructure 71
5.5 STS spectra of Ag(111) and Si domains 72
5.6 STS spectra of (4×4) and $(\sqrt{13} \times \sqrt{13})$-I superstructures . . . 73
5.7 Symmetry breaking models 74
5.8 XPS Si $2p$ core level 76
5.9 Si $2p$ core level after exposure to O_2 and to air 77
5.10 Real time RHEED patterns of Al deposition on silicene 79
5.11 XPS of principal core levels involved in the encapsulation process 80
5.12 STM images of the two Raman-probed configurations 83
5.13 Raman spectra of capped, uncapped silicene, and $Al_2O_3/Ag(111)$ 84
5.14 Computed Raman spectra of silicene superstructures 85
5.15 Experimental Raman spectra 86

Chapter 1

Introduction

> Many such saviours have come and gone, yet the reliable silicon CMOS continues to be scaled and to reach even higher performance levels
>
> D. Ferry

1.1 Motivations and thesis outline

The research activity described throughout this thesis aims at investigating the fundamental properties of some innovative materials of interest for a post-Si era of electronic devices. The scope is not to conceive any kind of device prototype, but to understand the intimate properties of those materials that sooner or later might potentially replace the nowadays commonly used materials. The relentless demand for faster and smaller electronic devices today requires an incessant effort in finding novel high performance solutions. In the last decades, condensed matter physics, nanotechnology, and materials science provided several examples of phenomena and materials whose applications (could) revolutionize our lives. Among them, it is worth noting the discovery of giant magnetoresistance by Fert and Grünberg (Nobel prize awarded in 2007), the invention of CCD sensor by Boyle and Smith (Nobel prizewinners in 2009), and the discovery of graphene's supreme properties by Geim and Novoselov (Nobel prize in 2010). These few examples show that the gap between research and technology is rapidly shortening. However, as highlighted by Ferry's quote, in the logic devices field there has not been yet a disruptive advance in order to replace silicon as active channel material (see the following section for a detailed discussion). Nonetheless, there is consensus that silicon is approaching its ultimate scaling limit. There are many reasons to explain this situation. The most important is of economic nature since that even the famous Moore's law imply economic reasons. In 1965, Moore observed that the transistor density exponentially increased in the early days of integrated

electronics [1], but his true insight was the understanding of the economics behind microelectronics, because the goal is not shrinking transistor size per se, but diminishing transistor cost. Transistor scaling makes this possible, but only up to the point at which the increased complexity starts raising manufacturing yields. However, there is nothing unique about silicon. In the not too far away future it may no longer make economic sense to shrink silicon transistors further [2]. There are two main approaches for going beyond silicon. They are labeled as *More Moore* and *More than Moore* as reported in the International Technology Roadmap for Semiconductors (ITRS) [3]. The idea of a technology roadmap for semiconductors can be traced back to the paper by Moore [1]. The ITRS, updated by scientific community and semiconductor companies, provides targets and guidelines for the future technology nodes. Further progress in the "miniaturization" and its associated benefits in terms of performances sustained by the incorporation into devices of new materials and the application of new transistor concepts is usually referred to as *More Moore* approach. The second trend, i.e. *More than Moore*, is characterized by functional diversification of semiconductor-based devices. These non-digital functionalities contribute to the miniaturization of electronic systems, although they do not necessarily scale at the same rate as the one that describes the development of digital functionality. Since the present research is not focused on the applicative device realization, the adopted approach can be considered in a *More Moore*-like direction, in the sense that the study of novel high-mobility materials is carried out in the framework of the usually expected requirements of standard logic devices materials, i.e. bearing in mind the layout of a classical transistor architecture. Once defined the subject of interest, it should be established how to address the purpose. Among many characterization techniques available in material science, the choice of Scanning Tunneling Microscope (STM) fits better to the shrinking dimensions of nano-devices as well as it provides multiple informations. For what concerns the survey among high-mobility materials, STM represents an ideal instrument to assess both structural and electronic properties. For this purpose, the main results of the present thesis are obtained by means of STM. Its strength relies on the ability to scrutinize the properties of materials up to the atomic scale with an unprecedented spatial and energetic resolution. Hence, the main goal of this research activity is devoted to foresee potentially suitable candidates for future electronic devices by means of an atomistic characterization of their properties. In this framework, the choice of candidates would ideally follow the timeline dictated by the progressive shrinking of devices dimensions. In this context, two classes of materials represent possible future options in nano-electronic technology: III-V semiconductors and two-dimensional (2D) materials. The former class features a near future option, while the latter is still in its infancy. For both classes, a promising representative candidate has been chosen and studied, $In_{0.53}Ga_{0.47}As(001)$ and silicene, respectively. Their structural, electronic, and even chemical properties have been analyzed in a complementary way.

This thesis is organized as follows. In this introductory chapter a description of the present state of the art and a justification of the choice of above mentioned candidates are reported. Chapter 2 reports on the basic theoretical and practical aspects of STM and on the experimental setup. In Chapters 3 and 5 the main results obtained with my group, at Laboratorio MDM in Agrate Brianza, in these last three years are presented. Ideally following the trend highlighted in this introduction, a first example of post-Si material is presented in Chapter 3 where electric phenomena at the Al_2O_3 / $In_{0.53}Ga_{0.47}As$ interface are scrutinized. As mentioned above, $In_{0.53}Ga_{0.47}As$ represents a suitable candidate for the near future implementation of III-V semiconductors into logic devices. Even if early studies on III-V semiconductors started in the 1960s, some aspects, e.g. Fermi level pinning and interface passivation, are still unclear. From this point of view, the combined STM and X-ray Photoelectron Spectroscopy (XPS) analysis of the Al_2O_3 / $In_{0.53}Ga_{0.47}As$ interface allows to get through these aspects. Moving forward the ideal roadmap, Chapter 4 will provide a brief introduction to 2D materials in order to elucidate basic aspects. In particular, the fundamental properties of graphene are summarized in order to facilitate the comparison with silicene, the Si-based counterpart of graphene. Silicene belongs to the class of materials *beyond graphene*, i.e. it is a prototypical material which is intended to overcome the to date applicative limitations of graphene. In Chapter 5, the study of silicene on Ag(111) is reported considering structural, electronic, and chemical properties. Finally, the results of the measurements presented in this thesis are summarized (Chapter 6).

1.2 High-mobility materials for logic devices

Since its birth, the electronic era has been mainly characterized by one single material: silicon. Silicon and silicon dioxide were, but somewhat they still are, the principal elements for micro-electronic's fundamental building block, the metal-oxide-semiconductor field effect transistor (MOSFET), which acts as a tiny switch, when it comes to logic operations. Following Moore's law [1], semiconductor mainstream electronics (processors, memories, etc.) experienced a very dynamic evolution over decades. The key point of this success was the continuous scaling of the Si MOSFETs. As these transistors got smaller over the years, more of them could fit on a chip without raising its overall cost. Today, Si MOSFETs with 20 nm gates are in mass production and, for the year 2020, the ITRS, the strategic planning document for the semiconductor industry, requires 10 nm MOSFETs [3]. In addition to the source and drain electrodes, a MOSFET (schematically depicted in Fig. 1.1) also contains a gate electrode that is used to control the conductivity of the channel by means of the electric field effect. The gate electrode and the active channel are separated by the gate dielectric. One successful aspect of Si MOSFET is related to the beneficial use of SiO_2 as a gate dielectric. The discovery of a stable SiO_2

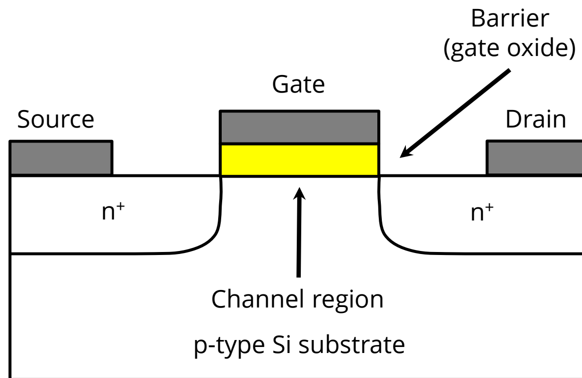

Figure 1.1: Cross-section of an n-channel Si MOSFET. When the voltage applied between the source and gate electrodes exceeds a threshold voltage, a conducting channel is formed and a drain current starts to flow. The length of the channel is defined by the length of the gate electrode; the thickness of the gate-controlled channel region is the depth to which the electronic properties of the semiconductor (p-doped Si in this case) are influenced by the gate.

dielectric-passivation scheme on silicon with a very low interface trap density by Atalla's research group at Bell Laboratories in 1959 [4] was perhaps the most important finding in semiconductor device physics since the original invention of the transistor by Bardeen, Brattain, and Shockley (Nobel prize in physics awarded in 1956) and the invention of integrated circuit (IC) by Kilby (Nobel prize in 2000). Subsequently, this high quality gate-dielectric process was used to fabricate the first FET. The Si MOSFET was much more scalable than the bipolar junction transistor and became the key building block in IC and microprocessor manufacturing [5]. Indeed, silicon dioxide is a native oxide of silicon, a naturally forming coat that grows when silicon is exposed to oxygen. Silicon dioxide makes an excellent chemical bond with silicon: only one out of 10^5 silicon atoms at the interface fails to bond with the adjacent silicon dioxide atoms, leaving what is called a dangling bond. These dangling bonds disrupt the flow of electrons in the channel, but at the SiO_2/Si interface they are rare enough that they do not degrade the overall performance of a transistor. The operation of a conventional MOSFET relies on the control of the channel conductivity, namely the source-drain current, by a voltage, applied between the gate and source. Hence, an important role is played by the channel material which, in a MOSFET, is usually a semiconductor and it needs to meet a number of requirements. First, it must be possible to switch off the device, otherwise it is useless for digital logic, which means that the semiconductor used to make the channel should, preferably, have a bandgap of $\sim$0.4 eV or more. Second, to obtain high power gain, the drain current should saturate as the voltage applied across the source and drain electrodes is increased. Third, short-channel effects must be suppressed, otherwise the performance of the transistor will

be degraded. It has been shown that short-channel effects can be reduced if the channel and the gate dielectric are very thin. Fourth and finally, a high carrier mobility in the channel is needed to increase the switching speed of the transistor [6]. Modern logic circuits are based on two kinds of transistors with complementary characteristics. They are referred to as n-type and p-type MOSFETs (NMOS and PMOS transistors). Together they are known as complementary metal–oxide–semiconductor (CMOS) transistors and have been the dominant logic family because their simplicity and their unique low power characteristics have allowed the synthesis of very dense ICs with many functionalities. A logic transistor operates as a switch that toggles between an *on* state and an *off* state. For fast switching, a high on-state (with a large on-current, I_{ON}) is desired. To limit standby power consumption, the off-state (with a small off-current, I_{OFF}) must be minimized. It is in terms of I_{ON} and I_{OFF} that the suitability of a transistor for logic should be assessed [2]. An important goal of scaling is to maximize I_{ON} while maintaining an acceptable I_{OFF}. The ability of Si MOSFETs to switch off enables Si CMOS to offer extremely low static power dissipation, which is the reason why Si CMOS has bested all competing logic technologies. Thus, any successor to the Si MOSFET, that is to be used in CMOS-like logic, must have excellent switching capabilities, as well as an on–off ratio, I_{ON} / I_{OFF}, of between 10^4 and 10^7 [3]. Both NMOS and PMOS transistors with reasonably matched performance are required for CMOS logic circuits. The PMOS transistors are based on holes and tend to be inferior to NMOS transistors because of their generally lower mobility. Success of Si MOSFET can thus be found in the combination of three elements: low power consumption, presence of a natural gate oxide, and high I_{ON}/ I_{OFF} ratio. For the last 50 years, the exponential rise in the power of electronics has been achieved by increasing the density of CMOS and improving their performances. Indeed, CMOS logic characteristics improve as their dimensions are reduced, following the motto “smaller is better” [2]. However, there is a consensus in the electronic community that Si MOSFET scaling is approaching its physical limit and that, in the long term, it will be necessary to introduce new technology boosters (new materials such as high-mobility semiconductors or new device concepts) to ensure that performance continues to improve [7]. Unfortunately, it becomes more and more difficult to further scale the Si MOSFET and simultaneously achieve the needed device performance. Major problems are parameter fluctuations of nominally identical transistors due to the discreteness of matter, short-channel effects, and the deteriorating parasitic effects [8]. To alleviate these problems, considerable efforts are spent on the development of nonclassical MOSFET architectures and on research of novel materials. While these measures help for the moment, they will only delay the moment when further MOSFET scaling becomes impractical. The problems in scaling have already led to a slowdown of long lasting and desirable exponential trends in semiconductor electronics in the more recent years. Therefore, to extend the lifetime of Moore’s law and to ensure an evolution of semiconductor electronics in

the future, researchers and chipmakers are intensively working on new materials and device concepts. To complicate the challenge, a technological breakthrough, such as one that incorporates new materials, will need to deliver substantially better performance (at least 30–50% better) than the silicon alternative. It must also promise to deliver more than one future scaled generation. All this must be achieved with cost-effective manufacturing and unprecedented reliability. One possible solution for going beyond silicon is to introduce a new channel material in which charge carriers travel at a much higher velocity than in silicon. This would allow a reduction in voltage without a loss of performance and this is why attention is turning to other materials such as III–V compound semiconductors and 2D materials. Using group III–V semiconductors or 2D materials in CMOS technology only makes sense if they allow further transistor scaling and provide better performance than any of the alternatives. Before this can happen, several critical problems have to be addressed. Indeed, thinning down the channel is not without drawbacks. For high speed applications, MOSFETs should respond quickly to variations in applied voltage; this requires short gates and fast carriers in the channel. Unfortunately, MOSFETs with short gates frequently suffer from degraded electrostatics and other problems (collectively known as short-channel effects) [7]. The barriers facing the take-up of a new channel material for CMOS technology are huge. In the following two possible solutions will be considered. These options involve the study of III–V semiconductors and 2D materials as potentially active channel in future logic devices. The former class represents a viable option compatible with Si-based processing while the latter represents an innovative approach which could probably involve even different device concepts. Indeed, a successor of the Si MOSFET for future high performance logic will most likely be an entirely new device based on an alternate operating principle [8]. Presumably, it will be not sufficient to further shrink MOSFET only changing the channel material, but it will be necessary to move from *More Moore* to *More than Moore* and *beyond CMOS* strategies.

1.3 III-V semiconductors

Practically ever since the Si MOSFET was invented in 1960, device engineers have been attempting to conceive a similar transistor with a gallium arsenide version suitable for large scale ICs. Basically, the main important aspect is that in III-V semiconductors the electron mobility is more than 10 times higher than in silicon, with several of them showing an n-type mobility of more than 10.000 $cm^2\ V^{-1}\ s^{-1}$ [2, 5]. However, the III-V integration appeared immediately not easy. As Ye reported [9], the repeated failures have led to the oldest joke in Silicon Valley about gallium arsenide: "it is the technology of the future and it always will be". This skepticism arose from the failures in finding the suitable insulator as gate oxide. Indeed, when GaAs oxidizes, it forms a complex mixture of native oxides like Ga_2O_3, As_2O_3, and As_2O_5. Similarly to the SiO_2/Si case,

researchers tried to use these native oxides for a gate insulator, but the results were poor because those oxides create many kinds of defects at the interface with the GaAs, which are detrimental for the electrical conductivity of the adjacent channel. Clearly, a better material was needed to be found if there was any hope of making gallium arsenide MOSFETs. But for decades there were no good gate insulators available for GaAs. Researchers tested silicon dioxide, silicon nitride, silicon oxynitride, and aluminum oxide, among other candidates. They also tried adding a third material, such as sulfur, silicon, or germanium, between the substrate, i.e. the channel, and the insulator to avoid the detrimental effects of electrically active traps that pin the semiconductor Fermi level [10]. Yet the results always proved so disappointing that most investigators had simply given up. But, researchers, after several work, realized that a related III-V semiconductor, InGaAs, would serve better for the channel [9]. In this compound, In atoms substitute for Ga atoms to a degree that can be adjusted arbitrarily, varying the In concentration. Tinkering with the In content allowed engineering the electronic properties of substrate as required. After much experimentation, a composition with 65% of In content was chosen. With this configuration, Ye and collaborators were able to build a MOSFET that carried more than 1 Amm^{-1} of channel width, that was the highest current density ever produced in four decades of work on III-V MOSFETs [9]. That test paved the way to bringing III-V semiconductors into what has long been the sole domain of silicon. Unfortunately, there is a serious problem about the large imbalance between electron and hole mobilities in III–V compounds. This difference arises from their considerably larger valence-band effective mass, together with their higher carrier scattering rate for hole transport than for electrons [5]. For this purpose, it is unlikely to expect an all–III-V microprocessor soon. Although III-V semiconductors allow electrons to move through them especially easily, they do not offer any advantage over silicon for positive charge carriers (holes). Hence, it would be very difficult to make a high performance PMOS using III-V compounds. The current consensus is that the semiconductor industry will probably employ germanium or antimonide based III-V materials, such as GaSb, for those transistors [2, 5, 9]. Indeed, Ge has the highest p-type mobility of all the known semiconductor materials and is therefore an attractive option as a silicon PMOS replacement in future logic applications [5]. In this framework, the greatest challenge is the preparation of a hybrid substrate for NMOS and PMOS transistors that incorporates blocks of two different materials with different lattice constants placed side by side. However, over the past few years, considerable research progress has been made in demonstrating the viability of III–V channel materials as a replacement for silicon in low power logic devices. Several key research breakthroughs have been achieved including the integration of such materials on a silicon substrate and the development of a high quality gate-dielectric interface with a scaled effective oxide thickness, a low interface state density (D_{it}), and controlled short-channel effects. Furthermore, InGaAs transistors have been demonstrated to outperform the silicon state of the art

due to their high carrier mobility [2]. These results prove that the substantial mobility gains obtained by using III–V channel materials can provide major performance and power-consumption improvements over Si devices for future technology nodes [5].
The aforementioned problems related to the interfaces between gate oxides and III-V semiconductors should be carefully analyzed in an atomistic view. Indeed, the SiO_2/Si interface clearly demonstrates that an adequate passivation of semiconductor surface is of paramount importance. These aspects are here considered at the interface between the III-V semiconductor candidate, $In_{0.53}Ga_{0.47}As$, and the high-κ Al_2O_3.

1.4 2D materials

Since its recent re-discovery, graphene, a 2D carbon-based material, has attracted a lot of attention from physicists for its fundamental properties but also from device engineers for its potential use in devices. In 2004, groups from Manchester University and from Georgia Institute of Technology published two pioneering papers on the preparation of graphene and the occurrence of the field effect in their samples [11, 12]. Moreover, high carrier mobilities have been observed in graphene [11]. These two papers not only started a revolution in solid-state physics but also fueled speculations that graphene could be used for transistors with scaling limits and operating speeds well beyond those of conventional state of the art transistors. Already in 2007, graphene found its place in the Emerging Research Devices chapter of the ITRS, which considers graphene to be among the candidates materials for post-Si electronics [3]. Graphene is potentially well suited to device-oriented applications because of its promising carrier transport properties and its purely 2D structure. Scaling theory predicts that a MOSFET with a thin barrier and a thin gate-controlled region will be robust against short-channel effects down to very short gate lengths [13]. The possibility of having channels that are just one atomic layer thick is perhaps the most attractive feature of graphene for use in transistors. The most frequently stated advantage of graphene is its high carrier mobility at room temperature. Mobilities of 10.000 – 15.000 $cm^2\ V^{-1}\ s^{-1}$ are routinely measured for exfoliated graphene on SiO_2-covered silicon wafers [11, 14], and upper limits of between 40.000 and 70.000 $cm^2\ V^{-1}\ s^{-1}$ have been suggested [14]. Moreover, in the absence of charged impurities and ripples, mobilities of 200.000 $cm^2\ V^{-1}\ s^{-1}$ have been predicted [15] and a mobility of $10^6\ cm^2V^{-1}s^{-1}$ was recently reported for suspended graphene [16]. For large-area graphene grown on nickel and transferred to a substrate, mobilities greater than 3.700 $cm^2\ V^{-1}\ s^{-1}$ have been measured [17]. Finally, for epitaxial graphene on silicon carbide, the mobility depends on whether the graphene is grown on the silicon face or the carbon face of SiC. Although graphene grown on the carbon face has higher mobility (values of ∼5.000 $cm^2\ V^{-1}\ s^{-1}$ have been reported

[18], compared with $\sim$1.000 cm^2 V^{-1} s^{-1} for graphene grown on the silicon face [18, 19]), it is easier to grow single layer and bilayer graphene on the silicon face, which makes the silicon face of SiC more suited for electronic applications. These mobility numbers are impressive, but they require closer inspection. The high mobilities mentioned above are related to large-area graphene, which is a semimetal, i.e. it is gapless. A general trend for conventional semiconductors is that the electron mobility decreases as the bandgap increases. The concurrent opinion is that graphene will not replace Si or the III–V compounds soon or in the mid-term future. A key issue here is the lack of a semiconducting bandgap allowing for a field effect. While all conventional semiconductors have a sizeable bandgap (e.g. Si 1.1 eV, Ge 0.7 eV, GaAs 1.4 eV), graphene is a zero-gap material and the missing gap has consequences for the operation of graphene transistors. The most obvious effect discussed already in the early days of graphene transistors is that MOSFETs with gapless channels do not switch off and, therefore, are not suited for complex logic circuits. Although the high mobilities offered by graphene can increase the speed of devices, they come at the expense of making it difficult to switch devices off, thus removing one of the main advantages of the CMOS configuration, i.e. its low static power consumption. However, the bandstructure of graphene can be modified and it is possible to open a bandgap in three different ways: by constraining large-area graphene in one dimension to form graphene nanoribbons, by biasing bilayer graphene, and by applying strain to graphene. Thus, although there are a number of techniques for opening a bandgap in graphene, they are all at the moment far away from being suitable for use in applications. Despite the low on–off ratios make use in logic devices unrealistic, transistors with large-area graphene channels are promising candidates for radiofrequency (RF) applications because RF MOSFETs are not required to switch off and can benefit from the high mobilities offered by large-area graphene. However, the absence of drain-current saturation will limit the RF performance of graphene transistors [7]. The high carrier mobility almost attracts the attention of the electronic community since it is one of the preconditions for fast transistors. On the other hand, other properties of graphene relevant for electronic devices received much less attention. The reduction of graphene only to its high mobility focused the discussion on the prospects of graphene into an unfortunate direction and led to misleading assessments. Graphene has been acclaimed as the perfect material for ultra-fast high performance transistors and designated as the successor of Si in mainstream electronics and of the III–V compounds in the RF field. Unfortunately, these high expectations graphene cannot meet, at least not in the short and medium term. Similar high expectations were devoted, as previously mentioned, in the 1970s and early 1980s, to GaAs which has been considered the semiconductor material of the future and akin discussions on carbon nanotubes in the 1990s had a similar optimistic tone [8]. However, this should not dissuade strong efforts in materials research since they are justified by a rather flexible scenario. In fact, in the semiconductor electronics

field, a radical transition from one semiconductor material to another is not impossible in general and indeed happened. Decades ago, Ge was the only semiconductor used, while later it has entirely been replaced by Si. However, the present situation is hardly comparable to the one when the transition from Ge to Si happened. Today, the chip industry is focused on Si CMOS to such an extent that it will be extremely difficult for a new material or device concept to compete and to make inroads into the Si CMOS world unless the new concept offers a dramatically significant advance. The early discussions on the potential of graphene had a prevailing positive optimism, mainly based on the high carrier mobilities observed in this material. This has repeatedly led to very optimistic assessments of the potential of graphene transistors and to an underestimation of their problems. For this purpose, researchers devoted their studies to find new materials with the useful compromise between reduced dimensionality and adequate electronic properties. Indeed, even if graphene is undoubtedly the best-known 2D material, it is by far not the only one [20–24]. Already in 2005, the Manchester group reported the preparation of single layer materials other than graphene [25]. It has been shown that semiconducting single layers of different transition metal dichalcogenides, e.g. MoS_2, $MoSe_2$, $MoTe_2$, and WS_2, can be produced by mechanical [26] and/or liquid [27] exfoliation. Recently, the first experimental MoS_2 MOSFETs have been demonstrated [28, 29]. These devices show reasonable mobilities and excellent switch-off. Monolayers of MoS_2 were studied earlier [25], including the demonstration of the electric field effect, but they received little attention until devices with switching on-off ratios of 10^8 and room temperature mobility of $\sim 100\,\mathrm{cm}^2\ \mathrm{V}^{-1}\ \mathrm{s}^{-1}$ were reported [28]. Although these mobilities are much lower than in graphene, they are still remarkably high compared with thin film semiconductors. Theoretical studies qualitatively confirm the experimental results and predict very high on–off ratios and excellent immunity to short-channel effects for MOSFETs with monolayer dichalcogenide channels [30, 31]. This rapid increase in feasible solutions about MOSFETs suggests that 2D materials, most notably graphene but dichalcogenides as well, will remain a hot topic and that these materials will find their place in future electronics. However, some practical issues should be considered when dealing to large scale production. Indeed, the fabrication of ICs is highly complex, since semiconductor fabrication plants are extremely expensive (typically several billion US dollars). Furthermore, because scaling alone has provided the needed performance improvements from one generation of ICs to the next, there has been little motivation for the chipmakers to introduce devices based on a fundamentally different physics or on another material than silicon. These aspects lead to the fascinating question whether there is the possibility to merge the unique properties related to 2D character with a compatible silicon-based technology. One such 2D lattice with graphene-like properties but made of silicon (or germanium) atoms, namely silicene (or germanene), might offer better compatibility with silicon processing and might provide solutions for some of the graphene's problems associated with

the lack of a gap. This survey is the main objective of the European Project *2D Nanolattices* [32]. The *2D Nanolattices* project is focused on finding ways to induce and stabilize 2D Si and Ge and prove for the first time that silicene has a physical existence. Indeed, in contrast to graphene, silicene does not exist in nature. This effort in silicene synthesis should be combined with similar 2D dielectrics which could offer a template for silicene and germanene growth and, at the same time, serve as gate insulators which are necessary for charge and current control in the 2D semiconductors. The ideal situation would be to obtain a sequence of dielectric/silicene alternating monolayers which are weakly bonded between each other in the vertical direction via van der Waals forces [25, 33]. In this framework silicene, together with other 2D atomic crystals and their heterostructures, represents an intriguing off-road opportunity with respect to the recently proposed roadmap for graphene [34].
Here, synthesis and identification of silicene on Ag(111) are reported. The fundamental aspects related to its structural and electronic characterization are examined, resulting in a more complicated picture with respect to graphene.

1.5 Why use STM?

There is another quite important aspect, beside the materials properties. Since devices dimensions are shrinking, even reaching the atomic scale [35], materials have to be studied in their peculiar properties with suitable probes. In this framework, the Scanning Probe Microscopy techniques, in particular the one exploiting the quantum-mechanical tunnel effect (usually denoted as STM), represent a viable solution to study novel materials on the atomic scale. Indeed, throughout the history of materials used in micro- and nano-electronics, a relevant role has been played by STM in determining their properties. STM allows studying both morphological and electronic properties of surfaces up to the atomic scale. These aspects are fundamental when dealing with the study of high-mobility materials since interface aspects are very important. Considering the aforementioned materials, which represent the evolution of Si MOSFETs active channel, it is possible to notice that STM deeply helped to characterize them. In particular, the silicon surface was the first test after the invention of STM. Binnig and collaborators resolved in real space for the first time the (7×7) reconstruction of Si(111) surface which was eventually solved by Takayanagi *et al.* with the Dimer-Adatom Stacking fault model [36, 37]. Similar investigations were performed on other Si reconstructions [38] and Ge [39]. The large family of III-V semiconductors has been also intensively scrutinized by means of STM [40–46]. This expertise has strengthened the STM role in surface science thus making its application to 2D materials straightforward [47–51]. Remarkably, the in-depth knowledge acquired, in particular on graphene grown on metal substrates [49], suggests the potential role that STM could play to elucidate the atomic structure of silicene. Hence, STM satisfies the

request of suitable probe to investigate both the paradigmatic materials here considered.

Bibliography

[1] G. E. Moore, *Electronics* **38**, 114 (1965)

[2] J. A. del Alamo, *Nature* **479**, 317 (2011)

[3] ITRS: The International Technology Roadmap for Semiconductors (www.itrs.net)

[4] M. M. Atalla, E. Tannenbaum, and E. J. Scheibner, *Bell Syst. Tech. J.* **38**, 749 (1959)

[5] R. Pillarisetty, *Nature* **479**, 324 (2011)

[6] F. Schwierz, *Nature Nanotech.* **6**, 135 (2011)

[7] F. Schwierz, *Nature Nanotech.* **5**, 487 (2010)

[8] F. Schwierz, *Proc. IEEE* **101**, 1567 (2013)

[9] P. D. Ye, *IEEE Spectrum* **45**, 42 (2008)

[10] H. Hasegawa, M. Akazawa, A. Domanowska, and B. Adamowicz, *Appl. Surf. Sci.* **256**, 5698 (2010)

[11] K. S. Novoselov, A. K. Geim, S. V. Morozov, D. Jiang, Y. Zhang, S. V. Dubonos, I. V. Grigorieva, and A. A. Firsov, *Science* **306**, 666 (2004)

[12] C. Berger, Z. Song, T. Li, X. Li, A. Y. Ogbazghi, R. Feng, Z. Dai, A. N. Marchenkov, E. H. Conrad, P. N. First, and W. A. de Heer, *J. Phys. Chem. B* **108**, 19912 (2004)

[13] D. J. Frank, Y. Taur, and H. S. P. Wong, *IEEE Electron Dev. Lett.* **19**, 385 (1998)

[14] J. H. Chen, C. Jang, S. Xiao, M. Ishigami, and M. S. Fuhrer, *Nature Nanotech.* **3**, 206 (2008)

[15] S. V. Morozov, K. S. Novoselov, M. I. Katsnelson, F. Schedin, D. C. Elias, J. A. Jaszczak, and A. K. Geim, *Phys. Rev. Lett.* **100**, 016602 (2008)

[16] D. C. Elias, R. V. Gorbachev, A. S. Mayorov, S. V. Morozov, A. A. Zhukov, P. Blake, L. A. Ponomarenko, I. V. Grigorieva, K. S. Novoselov, F. Guinea, and A. K. Geim, *Nature Phys.* **7**, 701 (2013)

[17] K. S. Kim, Y. Zhao, H. Jang, S. Y. Lee, J. M. Kim, K. S. Kim, J. H. Ahn, P. Kim, J. Y. Choi, and B. H. Hong, *Nature* **457**, 706 (2009)

[18] J. Kedzierski, P. L. Hsu, P. Healey, P. W. Wyatt, C. L. Keast, M. Sprinkle, C. Berger, and W. A. de Heer, *IEEE Trans. Electron Dev.* **55**, 2078 (2008)

[19] K. V. Emtsev, A. Bostwick, K. Horn, J. Jobst, G. L. Kellogg, L. Ley, J. L. McChesney, T. Ohta, S. A. Reshanov, J. Röhrl, E. Rotenberg, A. K. Schmid, D. Waldmann, H. B. Weber, and T. Seyller, *Nature Mater.* **8**, 203 (2009)

[20] A. H. Castro Neto and K. Novoselov, *Rep. Prog. Phys.* **74**, 082501 (2011)

[21] Q. H. Wang, K. Kalantar-Zadeh, A. Kis, J. N. Coleman, and M. S. Strano, *Nature Nanotech.* **7**, 699 (2012)

[22] S. Z. Butler, S. M. Hollen, L. Cao, Y. Cui, J. A. Gupta, H. R. Gutierrez, T. F. Heinz, S. S. Hong, J. Huang, A. F. Ismach, E. Johnston-Halperin, M. Kuno, V. V. Plashnitsa, R. D. Robinson, R. S. Ruoff, S. Salahuddin, J. Shan, L. Shi, M. G. Spencer, M. Terrones, W. Windl, and J. E. Goldberger, *ACS Nano* **7**, 2898 (2013)

[23] Q. Tang and Z. Zhou, *Prog. Mat. Sci.* **58**, 1244 (2013)

[24] M. Xu, T. Liang, M. Shi, and H. Chen, *Chem. Rev.* **113**, 3766 (2013)

[25] K. S. Novoselov, D. Jiang, F. Schedin, T. J. Booth, V. V. Khotkevich, S. V. Morozov, and A. K. Geim, *Proc. Nat. Acad. Sci.* **102**, 10451 (2005)

[26] C. Lee, Q. Li, W. Kalb, X. Z. Liu, H. Berger, R. W. Carpick, and J. Hone, *Science* **328**, 76 (2010)

[27] J. N. Coleman, M. Lotya, A. O'Neill, S. D. Bergin, P. J. King, U. Khan, K. Young, A. Gaucher, S. De, R. J. Smith, I. V. Shvets, S. K. Arora, G. Stanton, H. Y. Kim, K. Lee, G. T. Kim, G. S. Duesberg, T. Hallam, J. J. Boland, J. J. Wang, J. F. Donegan, J. C. Grunlan, G. Moriarty, A. Shmeliov, R. J. Nicholls, J. M. Perkins, E. M. Grieveson, K. Theuwissen, D. W. McComb, P. D. Nellist, and V. Nicolosi, *Science* **331**, 568 (2011)

[28] B. Radisavljevic, A. Radenovic, J. Brivio, V. Giacometti, and A. Kis, *Nature Nanotech.* **6**, 147 (2011)

[29] H. Liu and P. D. Ye, *IEEE Electron Dev. Lett.* **33**, 546 (2012)

[30] L. B. Kumar, Y. Ouyang, and J. Guo, *IEEE Trans. Electron Dev.* **58**, 3042 (2011)

[31] Y. Yoon, K. Ganapathi, and S. Salahuddin, *Nano Lett.* **11**, 3768 (2011)

[32] 2D NANOLATTICES: A research project funded by the Seventh Framework Program of the European Commission – Future and Emerging Technologies (FET) (www.2dnanolattices.eu)

[33] A. K. Geim and I. V. Grigorieva, *Nature* **499**, 419 (2013)

[34] K. S. Novoselov, V. I. Fal'ko, L. Colombo, P. R. Gellert, M. G. Schwab, and K. Kim, *Nature* **490**, 192 (2012)

[35] M. Fuechsle, J. A. Miwa, S. Mahapatra, H. Ryu, S. Lee, O. Warschkow, L. C. L. Hollenberg, G. Klimeck, and M. Y. Simmons, *Nature Nanotech.* **7**, 242 (2012)

[36] G. Binnig, H. Rohrer, Ch. Gerber, and E. Weibel, *Phys. Rev. Lett.* **50**, 120 (1983)

[37] K. Takayanagi, Y. Tanishiro, S. Takahashi, and M. Takahashi, *Surf. Sci.* **164**, 367 (1985)

[38] J. A. Stroscio, R. M. Feenstra, and A. P. Fein, *Phys. Rev. Lett.* **57**, 2579 (1986)

[39] H. J. W. Zandvliet, *Phys. Rep.* **388**, 1 (2003)

[40] R. M. Feenstra and J. A. Stroscio, *J. Vac. Sci. Technol. B* **5**, 923 (1987)

[41] J. A. Stroscio, R. M. Feenstra, D. M. Newns, and A. P. Fein, *J. Vac. Sci. Technol. A* **6**, 499 (1988)

[42] D. K. Biegelsen, R. D. Bringans, J. E. Northrup, and L. E. Swartz, *Phys. Rev. B* **41**, 5701 (1990)

[43] M. D. Pashley, K. W. Haberern, R. M. Feenstra, and P. D. Kirchner, *Phys. Rev. B* **48**, 4612 (1993)

[44] J. A. Kubby and J. J. Boland, *Surf. Sci. Rep.* **26**, 61 (1996)

[45] Q. K. Xue, T. Hashizume, and T. Sakurai, *Prog. Surf. Sci.* **56**, 1 (1997)

[46] V. P. LaBella, M. R. Krause, Z. Ding, and P. M. Thibado, *Surf. Sci. Rep.* **60**, 1 (2005)

[47] Y. Zhang, V. W. Brar, F. Wang, C. Girit, Y. Yayon, M. Panlasigui, A. Zettl, and M. F. Crommie, *Nature Phys.* **4**, 627 (2008)

[48] Y. Pan, H. Zhang, D. Shi, J. Sun, S. Du, F. Liu, and H. J. Gao, *Adv. Mater.* **21**, 2777 (2009)

[49] J. Wintterlin and M. L. Bocquet, *Surf. Sci.* **603**, 1841 (2009)

[50] L. Gao, J. R. Guest, and N. P. Guisinger, *Nano Lett.* **10**, 3512 (2010)

[51] M. Morgenstern, *Phys. Status Solidi B* **248**, 2423 (2011)

Chapter 2

Scanning Tunneling Microscopy

> The appeal and the impact of STM lie not only in the observation of surfaces atom by atom, but also in its widespread applicability, its conceptual and instrumental simplicity, and its affordability, all of which have resulted in a relaxed and almost casual perception of atoms and atomic structures
>
> G. Binnig and H. Rohrer

2.1 History

After 27 months its conception, in the night of 16 March 1981 at IBM Zürich, Binnig, Rohrer, and Gerber finally proved the exponential dependence of the tunnel current between a sharp tungsten tip and a platinum sample. Scanning Tunneling Microscopy (STM) was born [1–4]. After long efforts, they eventually achieved the idea that should "not have worked in principle" [5]. Since that night STM started to grow and in a short time to attract increasing interest. The first STM atomically resolved images were obtained on Au(110) surface [5]. However, a definite consideration from the scientific community occurred with the first STM images of Si(111)-(7×7) reconstruction [4]. Scientific results came meanwhile many other technical aspects, maybe less spectacular but nonetheless significant, were solved and performances improved. The STM allows to image atomic structures directly in real space, thus giving the opportunity to make the atomic aspects of nature "visible". Nowadays, the most important strength of STM is the correlation of structural, electronic and magnetic properties with high spatial and energy resolution. Additional techniques were developed starting from the STM concept. Scanning Probe Microscopy (SPM) sums up all the experimental techniques related to the invention of the STM. This class

of microscopes can now provide information about nanometer-scale properties of matter which is often inaccessible by any other experimental technique. Therefore, SPM has become an important experimental tool in a vast number of fields including biology, chemistry and, of course, physics. Starting from STM, SPM evolved into several probe-based techniques which rely on various physical principles based on almost every kind of interaction between a tip and a sample, such as force feedback, magnetic or capacitive detection [6]. SPM has also become a key characterization tool in nanotechnology and, in particular, STM has been critical in observing new phenomena on the atomic scale and has played a key role in surface science over the last 30 years. During this time, extraordinary developments of STM allowed to perform atoms manipulation [7, 8], reach extremely low temperature measurements (even at 10 mK) [9], view chemical reactions in single molecule [10], realize atomic-scale system performing logic operations [11], and many more...

2.2 Principles of tunneling

The basic mechanism of STM is the quantum tunneling of electrons, which describes the motion of electrons through a potential barrier of finite height and width. In classical mechanics particles with an energy lower than the barrier height are completely reflected from the barrier itself and forbidden to move across it (Fig. 2.1); however, within quantum mechanics, they can penetrate the barrier with non-zero probability. In order to understand the tunneling concept, first consider electron tunneling in a one-dimensional (1D) potential for simplicity [6]. The problem is to deduce the elastic motion of an electron with an energy E lower than the height V_0 of a rectangular potential barrier of width d, as shown in Fig. 2.1. This problem can be analytically solved using the time-independent Schrödinger equation in each region with respect to the barrier:

Region I:	$z < 0$	$V(z) = 0$	in front of the barrier,
Region II:	$0 \leqslant z \leqslant d$	$V(z) = V_0$	inside the barrier,
Region III:	$z > d$	$V(z) = 0$	behind the barrier.

$$\left[-\frac{\hbar^2}{2m}\frac{\mathrm{d}^2}{\mathrm{d}z^2} + V(z) \right] \psi(z) = E\psi(z) \tag{2.1}$$

where $\hbar$ is the Planck's constant divided by 2π, m is the free electron mass, and ψ is the electron wavefunction. The solution of the wavefunction in each region is given by:

$$\begin{aligned} \psi_I &= e^{ikz} + Ae^{-ikz} \\ \psi_{II} &= Be^{-\kappa z} + Ce^{\kappa z} \\ \psi_{III} &= De^{ikz} \end{aligned} \tag{2.2}$$

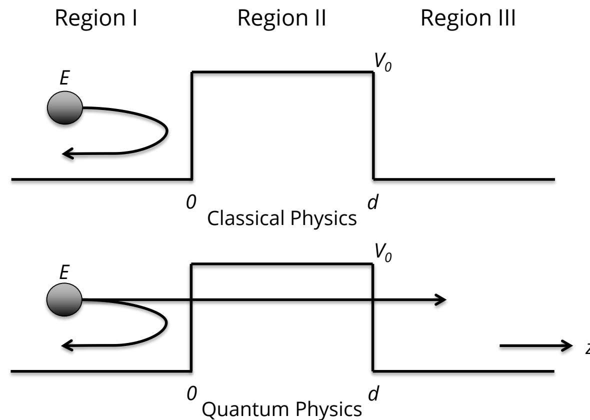

Figure 2.1: Tunnel effect in one dimension. In classical physics (top) a particle of energy E is reflected by a potential barrier if $E < V_0$; in quantum physics (bottom) the probability to move across the barrier is instead non-zero.

where $k^2 = 2mE/\hbar^2$ and $\kappa^2 = 2m(V_0 - E)/\hbar^2$. To quantify the probability that an electron will tunnel across the barrier, the percentage of the wavefunction that will be reflected by the tunneling barrier and the percentage that will be transmitted must be calculated. The probability of an electron tunneling is related to the transmission coefficient T. T is calculated by using the solutions of Schrödinger equation for each region (I, II, III) and matching the boundary conditions. With the given solutions (Eq. 2.2), the probability of transmission is given by:

$$T = |D|^2 = \frac{1}{1 + \frac{(k^2+\kappa^2)^2}{4k^2\kappa^2}\sinh^2(\kappa d)}. \tag{2.3}$$

If the barrier is high or wide enough that $\kappa d \gg 1$, then the wavefunction would be strongly attenuated leading to

$$T \approx \frac{16k^2\kappa^2}{(k^2+\kappa^2)^2} \cdot e^{-2\kappa d}. \tag{2.4}$$

The most significant finding here is the exponential dependence of the transmission coefficient on the barrier width d. Typically, $\kappa \approx 0.1\,\text{Å}^{-1}$ leading to the drop of the tunneling current by one order of magnitude as the distance increases by only 1 Å. This ensures the high spatial sensitivity of the STM. This simple model demonstrates the basic concept of the electron tunneling and how it is related to the barrier's parameters. In reality, a tunneling barrier is three-dimensional (3D), but the principles of a 1D potential illustrate the basic concepts of tunneling. Furthermore, both the probe and sample (regions I and III) have electronic structure which will dramatically alter the tunneling probability. This cannot be approximated using this simple model. More

complex models were derived by Bardeen [12] and Tersoff and Hamann [13, 14].

2.3 STM - Operating principle

Although the STM principle sounds simple in theory, implementation is challenging. In order to measure a tunneling current, typically on the order of 0.1 - 1 nA, the metallic tip has to be maintained at distance of about few Å above the surface of interest. Therefore, to acquire atomic scale informations, it is necessary to produce surfaces atomically smooth and nearly defects free. For this purpose STM, like many other surface science techniques, requires Ultra-High Vacuum (UHV) environment. A tunneling junction is achieved by placing a conducting tip atomically close to a biased surface. Sub-atomic positioning are obtained by means of piezoelectric scanners. When a voltage is applied to a piezoelectric material, it elongates or contracts, depending on the polarity. In this way a precise control of the three coordinates (x, y and z) can be achieved. Fig. 2.2 schematically shows how the feedback loop controls the position of the tip while scanning the sample. Commonly used tips are made of W or PtIr. W is typically used because it can be easily electrochemical etched by NaOH or KOH solutions to produce sharp tips with favourable aspect ratios [15, 16]. However, W oxidizes and further *in situ* cleaning procedures are needed before STM used. PtIr are also used because it is relatively inert to oxidation compared to W.

2.4 Topography: Surface structure

In their model, Tersoff and Hamann considered a tip with a local spherical symmetry, namely s-type tip wavefunctions, whereas contributions from tip wavefunctions with angular dependence have been neglected [13, 14]. They first considered the limits of low temperature and small applied bias voltage (lower than the work function of both tip and sample [17]) for which the tunneling current (within the s-wave approximation) can be expressed as:

$$I \propto V \cdot \rho_t(E_F) \cdot e^{2\kappa R} \underbrace{\sum_s |\psi_s(r_0)|^2 \cdot \delta(E_s - E_F)}_{\rho_s(E_F, r_0)} \tag{2.5}$$

with the decay rate $\kappa = \sqrt{2m\phi_{eff}}/\hbar$ where ϕ_{eff} is the effective local potential barrier height (in good approximation equal to the average of the tip and sample workfunctions), $\rho_t(E_F)$ is the density of states at the Fermi level for the tip, R is the effective tip radius and r_0 is the center of curvature of the tip and $\rho_s(E_F, r_0)$ can be identified with the surface local density of states (LDOS) at the Fermi level. Therefore, the STM images obtained at low bias in the constant current mode (see below) are contour maps of constant surface LDOS at Fermi

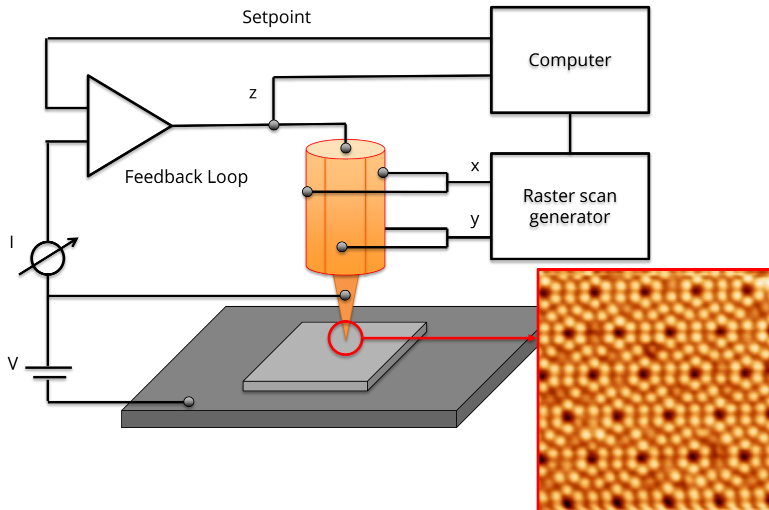

Figure 2.2: Principle of STM in the topography (or constant-current) mode. While the tip, controlled by the scan generator, laterally scans across the surface, the tunneling current is kept constant at the tunnel current setpoint. This is done by the feedback loop adjusting the z position of the tip. The respective tip displacement in z is then recorded as a function of the lateral position (x, y). STM images are obtained by plotting $z(x, y)$ in a color code as, for example, shown for the Si(111)-(7 × 7) reconstruction.

level, provided that the s-wave approximation for the tip can be justified. Since the wavefunctions decay exponentially in vacuum (z direction normal to the surface):

$$\psi_s(r) \propto e^{-\kappa z} \tag{2.6}$$

so the tunneling current depends on the distance d between tip and surface:

$$I \propto e^{-2\kappa d}. \tag{2.7}$$

This interpretation is no longer valid for high bias or for tip wavefunction with angular dependence. At larger bias voltage the tunneling current can be represented by a weighted integral over a range of energies:

$$I \propto \int_0^{eV} \rho_s(E) \cdot \rho_t(E, eV) \cdot T(E, eV)\, \mathrm{d}E \tag{2.8}$$

with a transmission factor

$$T(E, eV) = exp\left[-d \cdot \sqrt{\frac{4m}{\hbar^2}(\phi_t + \phi_s + eV - 2E)} \right]. \tag{2.9}$$

As discussed in Sec. 2.3, W and PtIr tips are the most widely used in STM experiments. For these materials the density of states at the Fermi level is

dominated by d states rather than s states [18]. Hence, evaluation of tunneling current can be obtained from a *derivative rule*, as discussed more in detail in Refs. [6, 18]. However, often a Tersoff-Hamann approach is enough to compare experimental and simulated STM images.
Eq. 2.7 demonstrates how sample surface topography can be recovered. Indeed, the exponential relationship between tunneling current and tip-sample separation allows to determine the surface topography. There are two different modes to scan the sample surface, the constant-height and the constant-current mode. In constant-height mode the vertical position of the tip is held constant while scanning and the resulting tunneling current between tip and sample is measured. Otherwise, in the constant-current mode, a feedback loop provides a constant tunneling current between tip and sample at every position (x, y). This means that the z position of the tip has to be adjusted during scanning. By recording the z movements, the surface topography can be then recovered. However, in practice, none of them can be realized experimentally and it is only possible to approximate one or the other by properly choosing the appropriate parameters for the feedback loop gain and scan speed. The most commonly used STM mode is under conditions close to constant-current imaging. In this mode, the feedback loop is enabled. In order to obtain an image, commonly referred to as *topography*, the piezoelectric scanner is set into an oscillating motion in the (x, y) plane. Typically, motion is broken up into a fast scan direction and a slow scan direction where each direction is orthogonal to each other. The scanner moves along the fast scan direction forward and backward, then moves one unit forward in the slow scan direction and repeats. During (x, y) motion, the negative feedback circuit applies voltages to the scanner (z-direction) in order to maintain a constant current. These applied voltages are recorded at each (x, y) position as well as the changes in voltage applied to the z position. From these data, a matrix can be constructed, where each matrix element location represents an (x, y) position. Since changes in the voltage applied to the scanner would typically result from a topographic feature (assuming no changes in the LDOS), this matrix will represent the topography $z(x, y)$ of the surface. This matrix is displayed with a color coding (e.g. grayscale) which helps to get an impression of the sample surface topography. Therefore, STM can be used in this mode to acquire atomic scale topographic information of a surface. Examples of topography images will be illustrated in subsequent chapters.

2.5 Spectroscopy: Electronic properties

Scanning Tunneling Spectroscopy (STS) is the most powerful STM related capability. It allows for atomic-scale characterization of the LDOS of a system of interest. It is possible to observe that differentiating Eq. 2.8, with the

approximation of constant ρ_t, results in:

$$\frac{\mathrm{d}I}{\mathrm{d}V} \propto \rho_t(0)\,\rho_s(eV)\,T(E,eV) + \int_0^{eV} \rho_s(E)\rho_t(eV-E)\frac{\mathrm{d}T(E,eV)}{\mathrm{d}V}\,\mathrm{d}E. \quad (2.10)$$

The second term can be often neglected since, under the assumption of monotonic variation of $T(eV)$, it contributes a smoothly varying *background* on which the spectroscopic information is superimposed and then the differential conductance $\mathrm{d}I/\mathrm{d}V$ is roughly proportional to the energy-dependent density of states of the sample [6, 19]. Experimentally, this concept involves measuring changes in current in response to some applied change in voltage. This is realized by positioning the tip above the surface with stabilized parameters. Then the feedback loop is disengaged and the voltage is typically swept between ranges of negative and positive energies relative to Fermi level (zero bias condition), meanwhile the tunneling current is acquired with the z position held constant. This gives informations about $I(V)$. A more comprehensive measure is the differential conductance $\mathrm{d}I/\mathrm{d}V$. Indeed, as demonstrated above, this value is directly proportional to the LDOS of the surface (when tip effects are neglected [20]). From the $I(V)$ curves, $\mathrm{d}I/\mathrm{d}V$ can be inferred from numerical techniques, such as a Savitsky-Golay differential algorithm, or can be acquired directly utilizing a lock-in scheme. In the latter case, a small ac modulation (few mV) at high reference frequency (several kHz) is added to the bias voltage between tip and sample. Lock-in amplifier can thus recover changes in the tunneling current with respect to the modulation bias. In realistic experiments, the differential conductance is recorded at non-zero temperature by a lock-in technique with a modulation voltage added to the stabilized voltage. While the former gives rise to thermal broadening of the density of states, the latter determines the instrumental resolution limit. The energy resolution of the experiment can be analyzed by using the Fermi-Dirac distribution function and the deconvolution of the modulation [21]:

$$\Delta E = \sqrt{\Delta E_{therm}^2 + \Delta E_{mod}^2} = \sqrt{(3k_BT)^2 + (2.5eV_{mod})^2}. \quad (2.11)$$

In order to detect features in the LDOS with a width less than ΔE, the temperature and V_{mod} have to be reduced as much as possible. In the present work, lock-in technique has been used to recover STS spectra at room temperature. Fig. 2.3 shows the system of tip and sample in tunnel contact in equilibrium and with applied sample bias voltage [17]. The occupied states of tip and sample are indicated by shaded region below Fermi level and the sample density of states is sketched by the curve inside the tunnel barrier. In the equilibrium state (Fig. 2.3a), the net tunneling current is zero. For the case of positive sample bias (Fig. 2.3b), the tunneling current arises from electrons tunneling from the occupied states of the tip (from $E_F - eV$ to E_F) into the unoccupied states of the sample. Imaging of these states is therefore referred

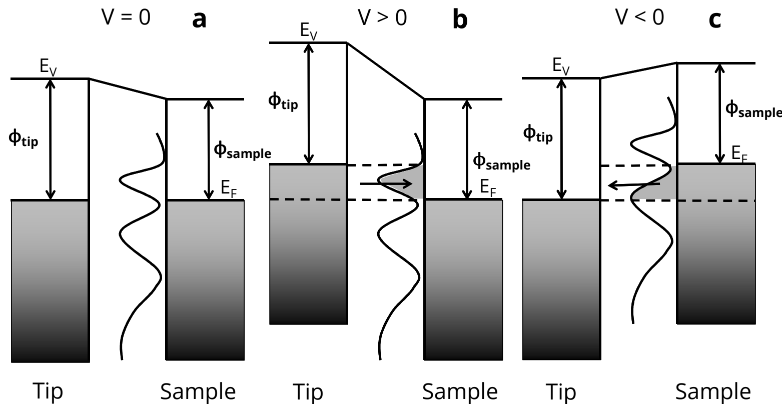

Figure 2.3: System of tip and sample in tunnel contact. (a) equilibrium, no net tunnel current; (b) positive sample bias, net tunnel current from tip to sample; (c) negative sample bias, net current current from the sample to the tip.

to as *empty state imaging* as electrons tunnel into the unoccupied levels of the sample. For this case, the LDOS of the sample at the (positive) applied bias is largely responsible for the measured tunneling current. For the opposite polarity (negative sample bias in Fig. 2.3c), the situation is reversed and slightly more complicated. Electrons tunnel from occupied states of the sample into the unoccupied states of the tip. Imaging and spectra taken at this polarity are commonly referred to as *filled state imaging* since the source of tunneling electrons comes from the filled states of the sample. However, for filled state spectroscopy, the current is mainly originated from electrons tunneling from Fermi level since they experience the lowest energy barrier. This results from the transmission coefficient which formulates that the states higher in absolute energy will have a higher probability of tunneling (see Eq. 2.9).
STS technique has been used to successfully characterize scattering of electrons, magnetic interactions, such as the Kondo effect, and single molecules electronic properties [22–24].

2.6 Instrumental setup

2.6.1 The UHV system

The experimental results shown in the following chapters were mainly performed in an UHV system which is depicted in Fig. 2.4. It consists of three different interconnected chambers called preparation (orange coloured in Fig. 2.4a), analysis (in blue), and SPM (in green). The system base pressure is in the low 10^{-10} mbar regime. A fast-entry lock allows to introduce samples and tips into the system without breaking the vacuum. Suitable holders transfer samples and tips through the different chambers. They can be inserted into

manipulators and thus be precisely positioned in each chamber. Furthermore, there are heating facilities in the manipulators of two main chambers. For substrate preparation the system is equipped with an ion sputter gun and direct, resistive, and radiative heaters. Preparation of thin films on single sample surfaces is carried out by means of Molecular Beam Epitaxy (MBE) in the preparation chamber. The use of different chambers for substrate preparation and thin films growth is crucial to ensure good UHV conditions during MBE, which can be checked by a Residual Gas Analyzer (RGA). Thin film deposition can occur by crucible filled with the material to be evaporated heated by electron bombardment or by cold lip Knudsen-cell. The evaporation rate can be adjusted by choosing appropriate parameters and can be calibrated by a quartz microbalance. Preparation and analysis chambers hold standard surface characterization techniques to check sample preparation. The periodicity of a surface and an estimate of the quality of its crystal structure can be determined by Reflection of High-Energy Electron Diffraction (RHEED). X-ray Photoelectron Spectroscopy (XPS) is an element specific method and allows a quantitative measure of the components at the surface. Similarly, Low-Energy Ion Scattering (LEIS) allows to identify surface elements by measuring the energy distribution of the scattered ions leaving the sample [25]. The main results discussed in the present thesis are obtained by means of STM, however a complete description of physics phenomena are usually achieved by combining different characterization techniques. For this purpose, in the following sections, a brief discussion of XPS and Raman spectroscopy are provided, since both decisively contributed to clarify the physical picture of $Al_2O_3/In_{0.53}Ga_{0.47}As$ interface (Chapt. 3) and silicene grown on Ag(111) (Chapt. 5), respectively. In particular, by combining UHV techniques it is then possible to accomplish a whole *in situ* characterization of the as-grown sample. On the other hand, the recent studies about graphene clearly demonstrated the important role played by Raman to elucidate the properties of 2D materials with honeycomb lattice. Therefore, in this framework it is necessary to correlate both *in situ* and *ex situ* characterizations.

2.6.2 Variable-temperature STM (VT-STM)

The VT-STM is available commercially from Omicron NanoTechnology GmbH. The same instrument can also perform Atomic Force Microscopy (AFM), Ballistic Electron Emission Microscopy (BEEM), and Kelvin-Probe Force Microscopy (KPFM) measurements. The tip is always at ambient temperature, whereas the temperature of the sample can be varied. It can be decreased by pumping liquid nitrogen or helium through a continuous flow cryostat while an integrated heating device allows an opposing increase in temperature. The temperature can be varied between 25 K to 1500 K. Any temperature within the specified range can be arbitrarily selected combining cooling and heating procedures. The samples are introduced into the STM with a wobble stick and

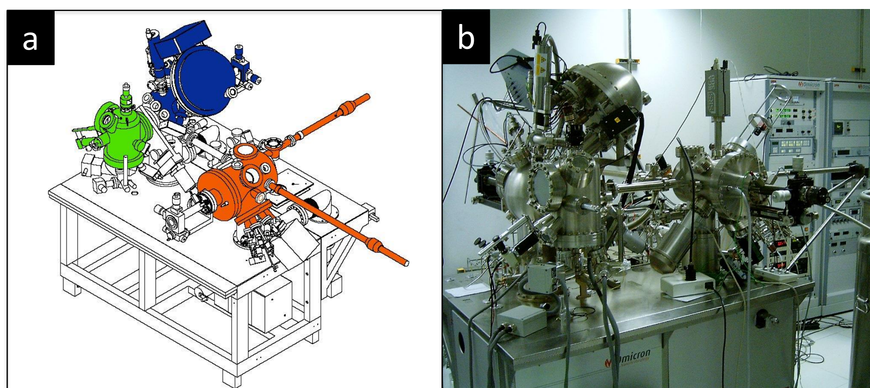

Figure 2.4: Pictures of UHV system at Laboratorio MDM. The preparation (in orange colour), the analysis (in blue), and SPM (in green) chambers are shown. The preparation chamber accommodates MBE facilities, RHEED, plasma source, and RGA. XPS and LEIS are in the analysis chamber. SPM chamber is exclusively devoted to STM-related techniques.

a screw driver with an Allen key is used to clamp the sample holder to the body of the STM to ensure good thermal contact. The STM tip is mounted on a tip holder scanner while the sample is fixed. A (x, y) sample stage allows access to different surface areas of the sample. High resolution SPM can be achieved by a vibration decoupling system. For this purpose the STM base plate is suspended by four soft springs, with resonance of the overall spring suspension system of about 2 Hz.

2.6.3 X-ray Photoelectron Spectroscopy

XPS is an important and widely used surface analysis method in many fields of studies in physics and chemistry. The technique probes the energy distribution of ejected electrons from solids via irradiations by x-rays and photoelectric effect. Electrons contain informations regarding chemical state, electronic structure, and atomic composition. Hence, surface composition as well as the electronic environment can be determined. In photoemission, a system containing N electrons in the initial state is left, after excitation, in a final excited state with N-1 electrons and one hole. The energy of the outgoing electron is influenced by the interaction between the photoelectron itself and the ionized system that is left behind. If the interaction is negligible (the so-called sudden approximation), the photoelectron kinetic energy E_k can derived using Einstein's argument (proposed in 1905) to explain the photoelectric effect (Fig. 2.5):

$$E_k = h\nu - |E_B| - \phi \tag{2.12}$$

where $h\nu$ is the energy of the incoming photon, ϕ the workfunction of the emitting material (in practice is the spectrometer workfunction, see Fig. 2.5),

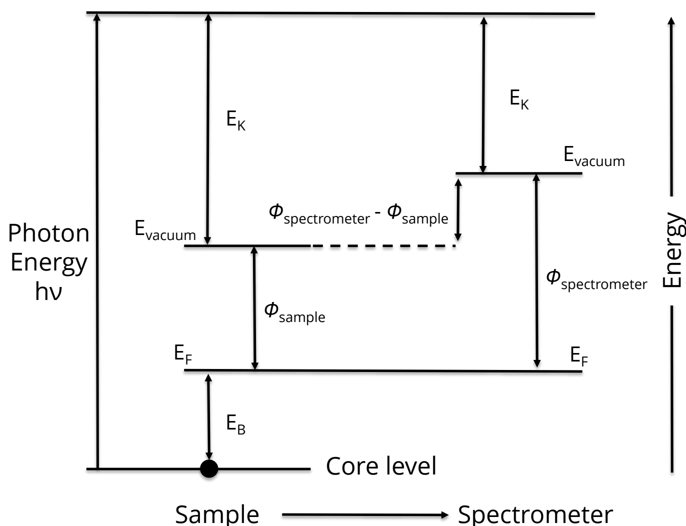

Figure 2.5: Energy level schematic for XPS binding energy measurements. The photoelectron emitted by the sample has a kinetic energy given by Eq. 2.12. However, the same photoelectron has a different kinetic energy in the spectrometer because of difference between sample and spectrometer workfunctions. Hence, the final value of workfunction necessary to calculate E_B is $\phi_{spectrometer}$.

and E_B the one-electron binding energy of the core level. In a solid, the core level binding energy usually refers to the Fermi level. By measuring the kinetic energies of the photoelectrons emitted in vacuum, it is possible to probe the occupied electron states of the system. Since every element has its own characteristic core level spectrum, XPS is an extraordinary tool for identifying different atomic species in a chemical compound [25, 26]. In the present work, XPS spectra were obtained by means of non-monochromatic Mg-$K_{\alpha1,2}$ (1253.6 eV) and Al-$K_{\alpha1,2}$ (1486.6 eV) radiation sources with a semispherical analyzer working with pass energy of 20 eV and with a variable take-off angle.

2.6.4 Raman Spectroscopy

Many different phenomena occur when shining light into a material (molecule or solid). Part of the light simply passes through the sample by transmission, while the remaining part interacts with the system through light absorption, reflection, photoluminescence, or light scattering. The amount of both parts of light is determined by the electronic and vibrational properties of the material. Furthermore, these different phenomena also occur when shining light into a given material with different energy photons, because different energies will be related to the different optical transitions occurring in the sample [27]. An incoming photon can be virtually absorbed by a material, i.e. not real absorption, which means that photon just shakes the electrons. They will then

scatter that energy back to another photon with the same energy of the incident one. In the case where the incident and scattered photons have the same energy, the scattering process is elastic and is named Rayleigh scattering [28]. The photon can shake the electrons, again with no real absorption, thus causing vibrations of the atoms at their natural vibrational frequencies generating phonons. In this case, when the electrons scatter the energy back into another photon, this photon has lost (gained) energy to (from) the vibration of the atoms. This is an inelastic scattering process that creates or absorbs a phonon and it is named Raman scattering. When the photon loses energy in creating a phonon a Stokes process takes place. When the photon gains energy by absorbing a phonon the process is named anti-Stokes process. In a solid, a further distinction is made between inelastic scattering by acoustic phonons, called Brillouin scattering, and by optical phonons, called Raman scattering. Therefore, within these optical processes, light scattering techniques provide an exceedingly useful tool to study fundamental excitations in solids and molecules. Indeed, light can be scattered inelastically so that the incident and scattered photons have different frequencies and this frequency difference is related to the properties of each material. The inelastic scattering of light is called Raman effect, in honor of Raman that discovered the effect in 1927. In the Raman process, an incident photon with energy E_i and momentum k_i reaches the sample and is scattered, resulting in a photon with a different energy E_f and momentum k_f. For energy and momentum conservation:

$$E_f = E_i \pm E_q \tag{2.13}$$

$$k_f = k_i \pm q \tag{2.14}$$

where E_q and q are the energy and momentum change during the scattering event induced by the excitation. Although different excitations can result from Raman scattering, the most common scattering phenomenon involves phonons, hence E_q and q are the energy and the momentum of the phonon created or annihilated in the inelastic Raman scattering event. In Raman scattering, the photon shakes the electrons. The inelastic scattering by phonons occurs because at different atomic positions within the vibrational mode displacements of the atom, the ability of the photon to shake the electrons is different. This ability to shake the electrons is measured by the polarizability. These characteristic vibrational modes are called normal modes and are related to the chemical and structural properties of materials. Since every material has a unique set of such normal modes, Raman spectroscopy can be used to probe materials properties in detail and to provide an accurate characterization of certain Raman-active phonon modes in specific materials [28]. When the energy E_i matches the energy gap between the valence and conduction bands in a semiconducting material, the probability for the scattering event to occur increases by many orders of magnitude and the process is then called a resonant Raman process (non-resonant otherwise). In the present work, Raman spectra were obtained

by means of *ex situ* visible and ultra-violet (UV) lines of an Ar^{+} laser equipped with the 2.41 eV/514 nm (green), 2.54 eV/488 nm (blue), and 3.41 eV/364 nm (UV) lines. Additional exciting wavelength of 1.96 eV/633 nm (red) is also used. Raman characterization is performed in a z backscattering geometry, for which k_i and k_f for the incident and scattered light, respectively, have the same direction and opposite signs. This gives the largest possible q vector and is the most common scattering geometry when working with nanomaterials, because a microscope is usually needed to focus the incident light onto small samples and the scattered light is also collected by the same microscope.

Bibliography

[1] G. Binnig and H. Rohrer, *Ultramicroscopy* **11**, 157 (1983)

[2] G. Binnig and H. Rohrer, *Surf. Sci.* **126**, 236 (1983)

[3] G. Binnig, H. Rohrer, Ch. Gerber, and E. Weibel, *Appl. Phys. Lett.* **40**, 178 (1982)

[4] G. Binnig, H. Rohrer, Ch. Gerber, and E. Weibel, *Phys. Rev. Lett.* **50**, 120 (1983)

[5] G. Binnig and H. Rohrer, *Rev. Mod. Phys.* **59**, 615 (1987)

[6] R. Wiesendanger, Scanning Probe Microscopy and Spectroscopy: Methods and Applications, Cambridge University Press, Cambridge (1994)

[7] D. M. Eigler and E. K. Schweizer, *Nature* **344**, 524 (1990)

[8] J. A. Stroscio and D. M. Eigler, *Science* **254**, 1319 (1991)

[9] Y. J. Song, A. F. Otte, V. Shvarts, Z. Zhao, Y. Kuk, S. R. Blankenship, A. Band, F. M. Hess, and J. A. Stroscio, *Rev. Sci. Instrum.* **81**, 121101 (2010)

[10] D. G. de Oteyza, P. Gorman, Y. C. Chen, S. Wickenburg, A. Riss, D. J. Mowbray, G. Etkin, Z. Pedramrazi, H. Z. Tsai, A. Rubio, M. F. Crommie, and F. R. Fischer, *Science* **340**, 1434 (2013)

[11] A. A. Khajetoorians, J. Wiebe, B. Chilian, and R. Wiesendanger, *Science* **332**, 1062 (2011)

[12] J. Bardeen, *Phys. Rev. Lett.* **6**, 57 (1961)

[13] J. Tersoff and D. R. Hamann, *Phys. Rev. Lett.* **50**, 1998 (1983)

[14] J. Tersoff and D. R. Hamann, *Phys. Rev. B* **31**, 805 (1985)

[15] A. J. Melmed, *J. Vac. Sci. Technol. B* **9**, 601 (1991)

[16] Y. Nakamura, Y. Mera, and K. Maeda, *Rev. Sci. Instrum.* **70**, 3373 (1999)

[17] R. J. Hamers, *Annu. Rev. Phys. Chem.* **40**, 531 (1989)

[18] C. J. Chen, *Phys. Rev. B* **42**, 8841 (1990)

[19] J. Li, W. D. Schneider, and R. Berndt, *Phys. Rev. B* **56**, 7656 (1997)

[20] M. Passoni, F. Donati, A. Li Bassi, C. S. Casari, and C. E. Bottani, *Phys. Rev. B* **79**, 045404 (2009)

[21] J. Wiebe, A. Wachowiak, F. Meier, D. Haude, T. Foster, M. Morgenstern, and R. Wiesendanger, *Rev. Sci. Instrum.* **75**, 4871 (2004)

[22] M. F. Crommie, C. P. Lutz, and D. M. Eigler, *Science* **262**, 218 (1993)

[23] V. Madhavan, W. Chen, T. Jamneala, M. F. Crommie, and N. S. Wingreen, *Science* **280**, 567 (1998)

[24] B. C. Stipe, M. A. Rezaei, and W. Ho, *Science* **280**, 1732 (1998)

[25] H. Bubert and H. Jennet (Editors), Surface and Thin Films Analysis: Principles, Instrumentation, Applications, Wiley, Weinheim (2002)

[26] S. Hüfner, Photoelectron Spectroscopy: Principles and Applications, Springer, Heidelberg (2003)

[27] F. Bassani and G. Pastori-Parravicini, Electronic States and Optical Transitions in Solids, Pergamon Press, Oxford (1975)

[28] A. Jorio, R. Saito, G. Dresselhaus, and M. S. Dresselhaus, Raman Spectroscopy in Graphene Related Systems, Wiley, Weinheim (2011)

Chapter 3

InGaAs

> Moore's law is all about economics and human innovation, and silicon integrated electronics is a dramatic manifestation of the human spirit. But there is nothing unique about silicon. In the not too distant future it may no longer make economic sense to shrink silicon transistors further. It is then that III–V compounds could become the key for continuing Moore's law
>
> J. A. del Alamo

3.1 III-V semiconductors

The III–V compound semiconductors, such as GaAs, AlAs, InAs, InP, and their ternary and quaternary alloys, combine elements in columns III and V of the periodic table. Some III–V compounds have excellent optical and electronic properties. Since their ability to efficiently emit and detect light, they are often used in lasers, light-emitting diodes, and detectors for optical communications, instrumentation, and sensing. These aspects indicate that III–V nano-electronics may have much wider device application areas than logics, combining information technology, nanotechnology, and biotechnology. A few compounds, especially GaAs, InGaAs, and InAs, exhibit outstanding electron transport properties, showing electron mobilities of one order of magnitude higher than Si. Transistors based on these materials are at the heart of many high speed and high frequency electronic systems [1]. No other family of materials currently being considered to replace the silicon channel in a metal-oxide-semiconductor field effect transistor (MOSFET) has such a promising prospective. Today, III–V complementary metal–oxide–semiconductor (CMOS) technology is a mainstream part of semiconductor research. Their future role has recently been recognized in the International Technology Roadmap for Semiconductors (ITRS) [2]. At the heart of a MOSFET there is the gate

stack. It is composed of a metal gate, a high-permittivity (high-κ) dielectric barrier, and the semiconductor channel. For a proper operation, the interface of the gate stack should have a dielectric free of trapped charge and other defects, a smooth interface with few interfacial imperfections and high stability. One of the advantages of silicon technology is the existence of a native oxide, SiO_2, that meets all these requirements. No such native oxides exist for III–V compounds. Furthermore, III–V surfaces show a phenomenon named *Fermi level pinning*, i. e. a physical effect which takes place at the surface of semiconductors whenever electrically active trap states partially or completely screen the semiconductor charge carriers from external electric field modulation [3]. This makes the MOSFET realization hard. For example, in GaAs, the most studied III–V compound, oxidation creates Ga and As oxides and sub-oxides, elemental As, As–As dimers, and Ga dangling bonds, among other defects [4, 5]. As a consequence, a high density of interface states results and prevents the effective modulation of the surface Fermi level [6]. Because of the difficulty of avoiding surface oxidation, early attempts to fabricate GaAs MOSFETs yielded devices with poor performance and low stability [7, 8]. However, in 1995, Ga_2O_3 deposited *in situ* on GaAs was shown to yield an interface of high quality [9]. This led to both n- and p-channel GaAs MOSFETs [10] and suggested that dielectric/III–V interfaces with unpinned Fermi levels were indeed possible. A further step forward was taken in 2003 when a GaAs MOSFET using Al_2O_3 deposited by Atomic Layer Deposition (ALD) was demonstrated [11]. The ALD technique is a chemically vapour deposition where the pulses are physically separated thus ensuring an atomic control of deposited layer. ALD is typically *ex situ* (with respect to the substrate preparation), robust and highly scalable and is widely used in modern silicon manufacturing, therefore a high quality ALD oxide/III–V interface paved the way to the exploitation of III–V semiconductors in MOSFET architectures. This result was unexpected because the starting GaAs surface had been exposed to air. Afterwards, transmission electron microscopy and X-ray Photoelectron Spectroscopy (XPS) showed that during ALD, a kind of “clean-up effect” takes place in which surface oxides are largely eliminated [12, 13]. Using ALD, MOSFET devices on other III–V compounds, such as InGaAs [14], InAs [15], and InP [16] were reported. Improvements in the electrical characteristics of III–V MOSFETs have been achieved by reducing the interface state density, D_{it} [1]. As their name suggests, interface states are electronic states that arise from disruptions to the ideal bonding structure of a semiconductor at its interface with a dielectric. They affect device operation and degrade the channel mobility. There are several ways to overcome the D_{it} problem. The first is to engineer the interface through pre-deposition cleaning treatments [17, 18], use of interfacial layers [19, 20], post-deposition treatments [17] or alternate dielectrics [21]. The second approach is to use compounds containing indium. Indeed, the device characteristics of MOSFETs improve significantly when the InAs mole fraction in the InGaAs channel is increased [22]. Indeed, $In_{0.53}Ga_{0.47}As$

is a suitable III–V semiconductor for a MOSFET channel material due to its high electronic mobility ($\sim$14.000 $cm^2\ V^{-1}\ s^{-1}$), bandgap of 0.74 eV, and its ability to be grown lattice matched on the semi-insulator substrate InP. Here, a combination of the aforementioned approaches is considered by studying the interfaces properties of the high-κ oxide Al_2O_3 deposited on two different $In_{0.53}Ga_{0.47}As$ reconstructions with a non-conventional experimental technique in this field, such as Scanning Tunneling Microscopy (STM).

3.2 $In_{0.53}Ga_{0.47}As$ (2×4) and (4×2) reconstructions

InGaAs surfaces grown by Molecular Beam Epitaxy (MBE) can be preserved from oxidation and contamination by condensation of a thin layer of amorphous As and then regenerated by thermal desorption of the As capping layer in vacuum [23]. The first STM imaging of InGaAs surfaces was performed by Ohkouchi and Gomyo [24]. Further detailed analyses on the InGaAs reconstructions have been subsequently carried out by Mirecki Millunchick *et al.* [25] and Bone *et al.* [26]. These works showed that, varying parameters as relative In/Ga concentration, i.e. the alloying, strain and temperature, a complex phase diagram with different surface reconstructions occurs. Existence of these reconstructions has been confirmed by Density Functional Theory calculation [27]. In the present study, particular attention is addressed to (2×4) and (4×2) reconstructions. Some differences have been reported in literature about reconstructions models depending on the sample preparation methodology. Indeed, InGaAs surfaces grown by MBE have been demonstrated to show (4×3) reconstruction, while the As-capped samples have not [28]. This aspect should be carefully taken into account throughout the present Chapter, since it is possible that the sample preparation might influence some properties, e.g. surface reconstructions or surface chemical composition. In the following, the substrates used are 1 µm-thick n-type (Si doping of $1 \times 10^{17}\ cm^{-3}$) $In_{0.53}Ga_{0.47}As(001)$ grown by MBE on n-type InP(001) wafers and capped with an As protective layer which is subsequently thermally desorbed in Ultra-High Vacuum (UHV). For substrates with nearly similar features, Shen *et al.* found that, starting from the As-rich (2×4) reconstruction, when the annealing temperature is increased, the surface reconstruction of decapped $In_{0.53}Ga_{0.47}As$ changes to a (2×4)-(4×2) mixed phase and finally, for higher annealing temperatures, the surface reconstruction further changes to the group III-rich, i.e. In or Ga, (4×2) reconstruction [28]. More in detail, they adopted the following three steps decapping and annealing procedure to prepare their samples. First, the samples are initially held at 180 °C for at least 2 hours degassing, thus removing the weakly bonded impurities from the surface such as water or moisture. Second, the sample temperature is raised to 330 °C for typically between 2 and 4 hours, in order to remove the As capping layer. Eventually, the sample is gradually heated to the peak temperature followed by quenching. The peak temperature determines

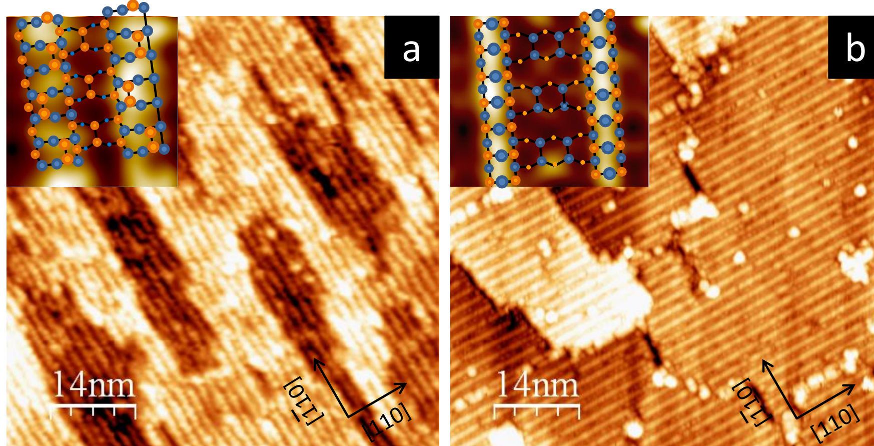

Figure 3.1: STM images 70×70 nm^2 of $In_{0.53}Ga_{0.47}As(001)$-$(2 \times 4)$ (a) and (4×2) (b) reconstructions. Insets show atomistic models of both reconstructions where orange spheres represent As atoms while blue spheres In/Ga atoms. STM images were acquired at -1.5 V bias with an etched W tip and at tunneling current set point of $0.3 - 0.5$ nA.

the observed surface reconstruction. For example, (2×4), mixed (2×4) and (4×2), and pure (4×2) surfaces are observed at 380 °C, 400 – 440 °C, and 455 °C peak temperatures, respectively [28]. Heating above 470 °C induces surface disorder probably from depletion of As from the bulk. Despite the arbitrary temperature values which, of course, depend on the proper heater and how they are measured (typically by means of thermocouples), a similar approach has been adopted here to prepare samples. Since the temperature calibration can be affected by several parameters (sample heater, position of the thermocouple, etc.), temperature reading has been crosschecked by pyrometer-based calibration of the K-thermocouple placed in the proximity of the transferable sample holder. The STM topographies in Fig. 3.1 show As-rich (2×4) and group III-rich (4×2) $In_{0.53}Ga_{0.47}As$ reconstructions. After decapping at 365 °C the resulting reconstruction is an As-rich (2×4) with periodicity $2\times$ and $4\times$ respectively along the [$\bar{1}$10] and [110] directions (Fig. 3.1a). On the other hand, when annealed at 440 °C this reconstruction is reversed in a group III-rich (4×2) reconstruction (Fig. 3.1b). Atomic model of $In_{0.53}Ga_{0.47}As(001)$-$(2 \times 4)$ surface reconstruction is deduced by comparison with GaAs(001)-(2×4) and InAs(001)-(2×4) reconstructions. The GaAs(001)-(2×4) surface has a nearly perfect $\beta2(2 \times 4)$ reconstruction with the exception of a few missing arsenic dimers that are probably caused by thermal desorption [29]. Conversely, the InAs(001)-(2×4) surface is dominated by the $\alpha2(2 \times 4)$ reconstruction with its zig-zagging rows [30]. The $In_{0.53}Ga_{0.47}As(001)$-$(2 \times 4)$ surface exhibits zig-zagging rows which is indicative of $\alpha2(2 \times 4)$ reconstruction. However, Shen *et al.* demonstrated that there is a higher fraction of double As-dimers (from 2 to 4 times) on the row of $In_{0.53}Ga_{0.47}As(001)$-$(2 \times 4)$ surface than on the

row of InAs(001)-(2×4) [28]. Therefore, (2×4) surface reconstruction is made of a top row (along the $[\bar{1}10]$ direction) of dimerized As atoms which are bonded to In or Ga atoms. Conversely, the main feature for the group III-rich $In_{0.53}Ga_{0.47}As(001)$ surface is represented by rows running in the [110] direction. Between the rows are trough regions. STM images reveal that this (4×2) surface is similar to the surface reconstructions of several other low bandgap III–V materials like InAs(001)–(4×2) surface, but it is distinct from the Ga-rich GaAs(001)–(4×2) reconstruction [31]. Hence, the $In_{0.53}Ga_{0.47}As(001)$-$(4 \times 2)$ reconstruction exhibits undimerized In/Ga atoms along the rows divided by trough regions containing two In/Ga dimers with a mean separation of 1.7 nm [32]. Based on STM results, $In_{0.53}Ga_{0.47}As(001)$–$(2 \times 4)$ and (4×2) structure models are proposed in insets of Fig. 3.1 that show As-dimers and undimerized In/Ga atoms in the top layer, respectively.
In literature, more attention is paid to the (4×2) reconstruction instead of the (2×4) one. This is usually justified by a lower reactivity to oxygen of the former reconstruction than the latter. By comparison with GaAs(001)-(2×4), Shen *et al.* suggested that the (2×4) reconstruction should undergo oxygen induced displacement reactions because the dimerized As atoms are likely to be displaced by ambient oxygen during oxide deposition [32]. Conversely, the (4×2) reconstruction is less reactive to oxygen and, therefore, probably more suitable for oxide deposition [32]. However, here, a comparison between the two considered reconstructions is reported. Indeed, based on chemical reactivity study and ALD-grown Al_2O_3 (see Sec. 3.3 and Sec. 3.4), a whole *in situ* study is performed, thus avoiding extra sources of oxidation and contamination. This comparison is mainly devoted to discern the different behavior of the considered reconstructions that show different chemical terminations. Indeed, the As-rich and group III-rich reconstructions, showing different surface atoms, are a good benchmark to understand the interface properties between InGaAs and a potential gate oxide. Moreover, while the two considered reconstructions are chemically different, the electronic behavior of the freshly prepared surfaces is similar as demonstrated by Scanning Tunneling Spectroscopy (STS). STS experimentally provides the local electronic structure of the surface (see Chapt. 2). In particular, STS may determine unambiguously the Fermi level position with respect to the valence band maximum (VBM) and conduction band minimum (CBM). For clean and unpinned n-type semiconductor surface, the Fermi level should reside nearby the CBM as due to the donor-like doping level. However, STS spectra in Fig. 3.2 show that in both surface reconstructions of the n-type $In_{0.53}Ga_{0.47}As$ the Fermi level is located in the proximity of the VBM. This p-type character is attributed to Fermi level pinning at the surface [32]. While theoretical calculations show that surface Fermi level pinning for (4×2) reconstruction is due to strained unbuckled dimers in the trough, so far neither clear theoretical nor experimental explanation has been proposed for the (2×4) case. Nonetheless the deeply different atomic arrangement of the two reconstructions (see Fig. 3.1), a common physical origin of the Fermi level pinning can be related

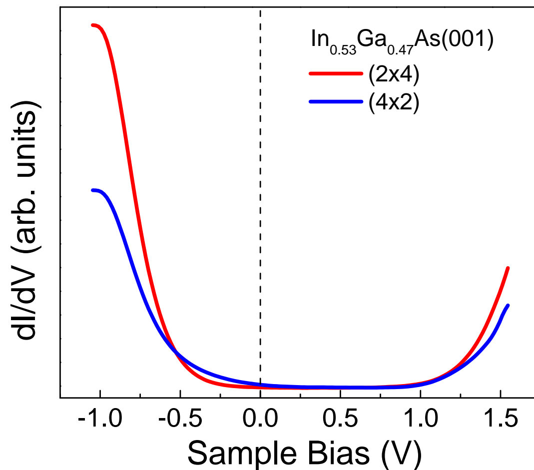

Figure 3.2: STS spectra of $In_{0.53}Ga_{0.47}As(001)$–$(2 \times 4)$ in red and $In_{0.53}Ga_{0.47}As(001)$–$(4 \times 2)$ in blue. Fermi level is at zero bias condition.

to intrinsic defects in the proximity of the $In_{0.53}Ga_{0.47}As$ surface consistently with the theoretical prediction of As dangling bonds resonant at ~ 0.1 eV above VBM [33].

3.3 Chemical reactivity of $In_{0.53}Ga_{0.47}As$ surfaces

The chemical reactivity of the two surfaces is studied by probing the As $3d$, In $3d_{5/2}$, and Ga $2p_{3/2}$ XPS lines after exposure in air (see Fig. 3.3). In the following, after air exposure, the (2×4) and (4×2) reconstructions will be denominated as the low-T and high-T surfaces respectively, with reference to the decapping temperature since the pristine surface reconstruction may change, thus making incorrect the original reconstructions notion. The XPS spectra were decomposed with pseudo Voigt functions (doublets for the As $3d$ line) upon Shirley background removal [34]. Fit to the spectra was based on the shape profile of bulk peaks in the pristine reconstructed surfaces [35]. Limited adventitious carbon contamination has been observed after exposure. The As $3d$ line of the high-T surface is rid of As oxides whereas a As_2O_3 can be deduced from the low-T surface. To gain a higher surface sensitivity, the As $2p_{3/2}$ lines are reported in the insets of Fig. 3.3 which evidence the formation of As_2O_3 on the low-T surface and minor trace of As_2O_3 also in the high-T surface upon exposure. The In $3d_{5/2}$ and Ga $2p_{3/2}$ lines exhibit an extra-component indicative of chemisorbed species along with the bulk one. In both In $3d_{5/2}$ lines the extra-component can be associated with sub-stoichiometric InO_x because the chemical shift Δ is lower than that reported for the In_2O_3 [17, 36], whereas $\Delta = 0.6$ eV in the Ga $2p_{3/2}$ lines is consistent with Ga_2O species [37, 38]. A

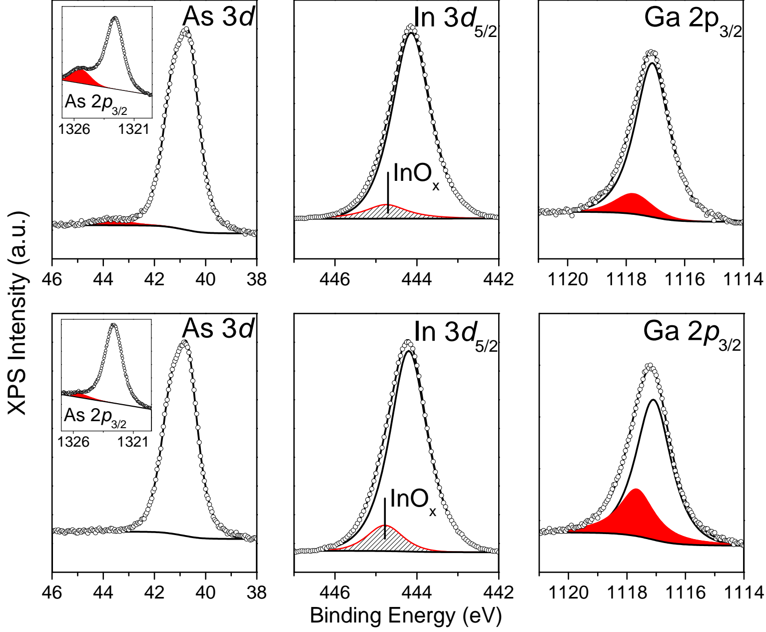

Figure 3.3: XPS spectra of As $2p_{3/2}$, As $3d$, In $3d_{5/2}$, and Ga $2p_{3/2}$ lines of $In_{0.53}Ga_{0.47}As(001)$–(2 × 4) (top panel) and $In_{0.53}Ga_{0.47}As(001)$–(4 × 2) (bottom panel) after air exposure for 3 min.

larger amount of In-O and Ga-O bonds is revealed after exposure of the high-T surface than low-T case.

3.4 Al_2O_3 deposition by ALD

The air-exposed surfaces were moved in atmospheric pressure (3 min in N_2 flow) to an ALD reactor where Al_2O_3 films were grown at 300 °C as follows: 500 ms trimethyl-Al (TMA) pulse, 8 s N_2 purge, 15 ms H_2O pulses, and 8 s N_2 purge. The effect of the ALD cycles on the interface chemistry is again elucidated by the As $3d$, In $3d_{5/2}$, and Ga $2p_{3/2}$ XPS lines in Fig. 3.4 recorded after deposition of 2 nm-thick Al_2O_3 film on the two surfaces. Within the XPS detection limits, the As $3d$ lines evidence an As oxide-free surface on both samples. From the In $3d_{5/2}$ lines, InO_x disappears in the low-T sample whereas formation of In_2O_3 is observed in the high-T sample which indicates further In oxidation. The Ga $2p_{3/2}$ lines can be decomposed in a bulk peak and a Ga* component with $\Delta = 0.9$ eV consistent with the interplay of interfacial Ga_2O_3 and Ga_2O [37]. It is important to note that Ga–O bonds increase after ALD cycles despite the previously reported reducing effect played by TMA on both As and Ga oxides in a different extent (the so-called TMA "self-cleaning" [17, 39, 40]). Moreover, the relative intensity of Ga*, i.e. the amount of Ga

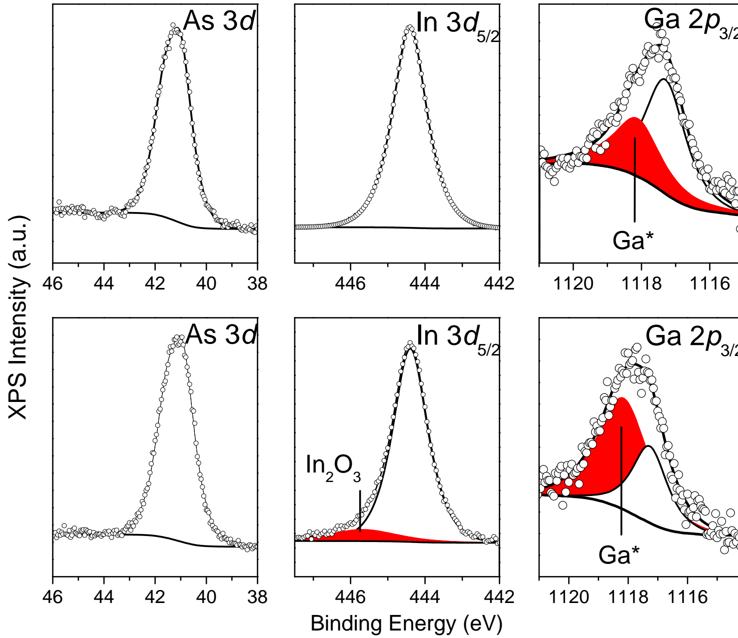

Figure 3.4: XPS spectra of As $3d$, In $3d_{5/2}$, and Ga $2p_{3/2}$ lines of $In_{0.53}Ga_{0.47}As(001)$–$(2 \times 4)$ (top panel) and $In_{0.53}Ga_{0.47}As(001)$–$(4 \times 2)$ (bottom panel) after 2 nm ALD-grown Al_2O_3.

oxides, is much higher in the high-T sample than in the low-T one. Despite the As-rich (2×4) reconstruction in the low-T sample undergoes an easier oxidation of As dimers thus rendering the exposed (2×4) surface richer of As_2O_3, XPS data in Fig. 3.4 show surface As–O bonds to be more efficiently reduced by the initial TMA pulse with respect to the Ga–O and In–O ones in both samples. As a consequence, a significantly higher content of interfacial Ga–O (interplay of Ga_2O and Ga_2O_3) and In–O (In_2O_3) bonds results in the interface between Al_2O_3 and the exposed (4×2) reconstructed $In_{0.53}Ga_{0.47}As(001)$ surface (high-T sample) because Ga–O and In–O bonds can more readily form upon oxygen chemisorption to Ga and In onto the rows along the [110] direction (see Fig. 3.1) as observed on InAs(001) [41].

3.5 Al_2O_3 deposition by MBE

The results shown in the previous sections show that air exposure and *ex situ* ALD growth inevitably complicate the study of Al_2O_3 / $In_{0.53}Ga_{0.47}As(001)$ interfaces. Therefore, for a better comprehension of the passivation role played by the high-κ oxide, a whole *in situ* approach is highly demanded, even if not usually employed in the semiconductor industry. However, a similar scenario occurred in 1996 when Ga_2O_3 and Gd_2O_3 oxides were demonstrated to pro-

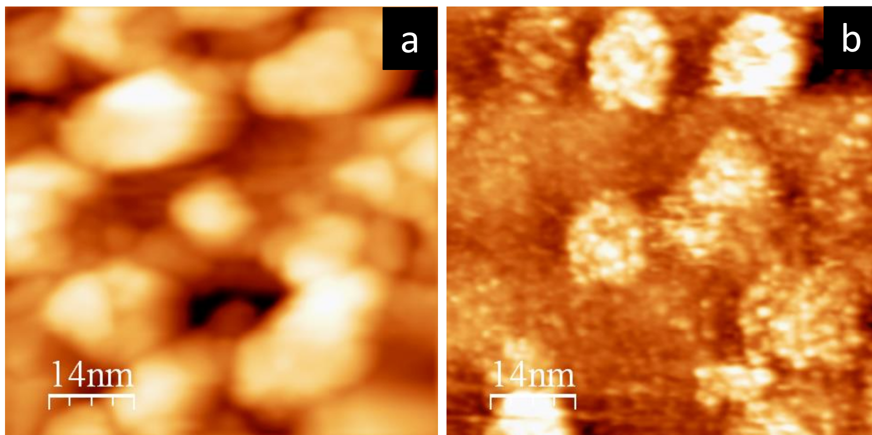

Figure 3.5: STM images 70×70 nm^2 of Al_2O_3 deposited on $In_{0.53}Ga_{0.47}As(001)$-$(2 \times 4)$ (a) and (4×2) (b) reconstructions.

duce good quality interfaces with GaAs, but required MBE technique that is unsuitable for high volume manufacturing [11]. For this purpose, here, a MBE-grown Al_2O_3 is considered in the framework of a whole *in situ* approach which includes XPS and STM/STS analysis (see the following sections). Preventing oxidation of III-V surface during gate dielectric deposition could be essential to achieve Fermi level unpinning [3]. For this purpose, before Al_2O_3 deposition, one monolayer of Al has been nominally grown by MBE in order to prevent $In_{0.53}Ga_{0.47}As$ oxidation [42]. Al_2O_3 films were grown at room temperature by means of the reactive deposition technique, i.e. a metallic Al flux is directed to the sample, while the growth chamber is filled by ultra-pure O_2 at 10^{-6} mbar pressure. After $\sim$3 nm-thick Al_2O_3 deposition, the observed morphology is strongly different (Fig. 3.5) from the pristine surface reconstructions. In Fig. 3.5a, the Al_2O_3 film on (2×4) reconstruction is characterized by large (tens of nm) three dimensional islands. On the (4×2) reconstruction the growth mode is quite similar but there are more small (few nm) islands on the larger ones than (2×4) surface. In both cases the pristine $In_{0.53}Ga_{0.47}As$ surface is fully covered by the Al_2O_3 film. It should be pointed out that, here, the MBE parameters have not been optimized in order to achieve the flattest or most conformal oxide deposition, but were instead intended to avoid excessive substrate oxidation, which is detrimental for electrical properties. After Al_2O_3 deposition and by means of STS, a Fermi level shift towards midgap is observed on both reconstructions (green curves in Fig. 3.6). This shift can be estimated in $\sim$0.25 eV and $\sim$0.2 eV for the $Al_2O_3/In_{0.53}Ga_{0.47}As$-$(2 \times 4)$ and $Al_2O_3/In_{0.53}Ga_{0.47}As$-$(4 \times 2)$ interfaces, respectively. The presence of the ultra-thin oxide films induces a little enlargement in the bandgap measurement which is limited by the low thickness of the insulating film itself, thus ensuring the possibility to still perform STM and STS. The STS spectra demonstrate that

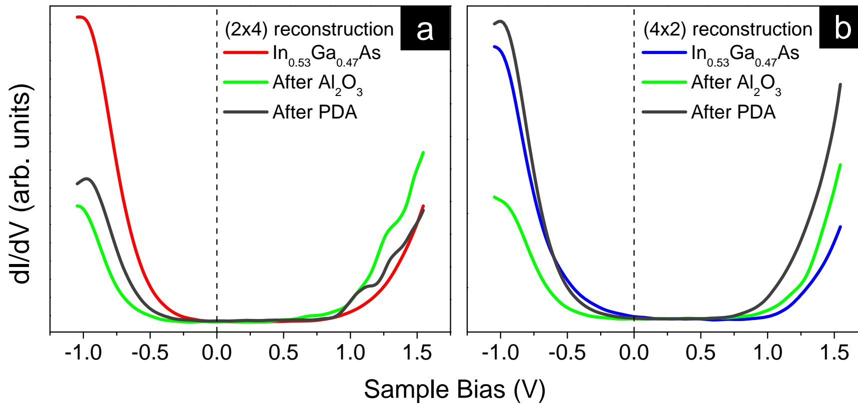

Figure 3.6: STS spectra of freshly decapped $In_{0.53}Ga_{0.47}As(001)$–$(2\times4)$ in red, after oxide deposition in green, and after PDA in dark gray (a). Clean $In_{0.53}Ga_{0.47}As(001)$–$(4\times2)$ is depicted in blue (b). Fermi level is at zero bias condition.

the Al_2O_3 can partially unpin both reconstructions. The overall shift of about 0.2 eV is similar to that reported in $HfO_2/In_{0.53}Ga_{0.47}As$-$(4 \times 2)$ interface [43], while complete unpinning has been achieved on the $In_2O/In_{0.53}Ga_{0.47}As$-$(4 \times 2)$ interface, but after post-deposition annealing (PDA) treatment at 380 °C [44]. This latter case evidences the important role played by PDA treatments, thus suggesting that in the absence of a thermal oxidation of the semiconductor surface, which disrupts the surface, some oxides will be able to bond with $In_{0.53}Ga_{0.47}As$ in a geometry, which eliminates the surface states within the bandgap. Therefore, a similar analysis has been carried out in the present case. Here, PDA treatments have been performed in a O_2 atmosphere (at 10^{-6} mbar pressure). A reconstruction-dependent behavior after PDA at 200 °C can be singled out. On the (2×4) reconstruction the Fermi level slightly shifts towards the original condition (dark gray curve in Fig. 3.6a) while, on the other hand, on the (4×2) reconstruction the original Fermi level pinning condition is fully restored (dark gray curve in Fig. 3.6b), i.e. the valence band maxima of the STS spectra coincide. In case of the (4×2) reconstruction, this behavior might be related to surface roughening as argued in the case of HfO_2 on $In_{0.53}Ga_{0.47}As$ even if at higher annealing temperature (300 °C) [43]. Indeed, also for Al_2O_3, a rms roughness is observed to increase from $\sim$1.3 nm to $\sim$1.8 nm after annealing at 200 °C for the $Al_2O_3/In_{0.53}Ga_{0.47}As$-$(4 \times 2)$ interface. On the other hand, in the $Al_2O_3/In_{0.53}Ga_{0.47}As$-$(2 \times 4)$ interface, the roughness value slowly decreases from $\sim$1.6 nm to $\sim$1.5 nm.

The chemical analysis carried out by means of *in situ* XPS can shed light on the role played by the interface in both reconstructions. The XPS spectra of the As $2p_{3/2}$, As $3d$, In $3d_{5/2}$, Ga $2p_{3/2}$, O $1s$, and Al $2p$ lines have been collected for the as-grown $Al_2O_3/In_{0.53}Ga_{0.47}As$ interfaces and for subsequently PDA. Fig. 3.7 shows the As $2p_{3/2}$, In $3d_{5/2}$, and Ga $2p_{3/2}$ lines related to the as-grown

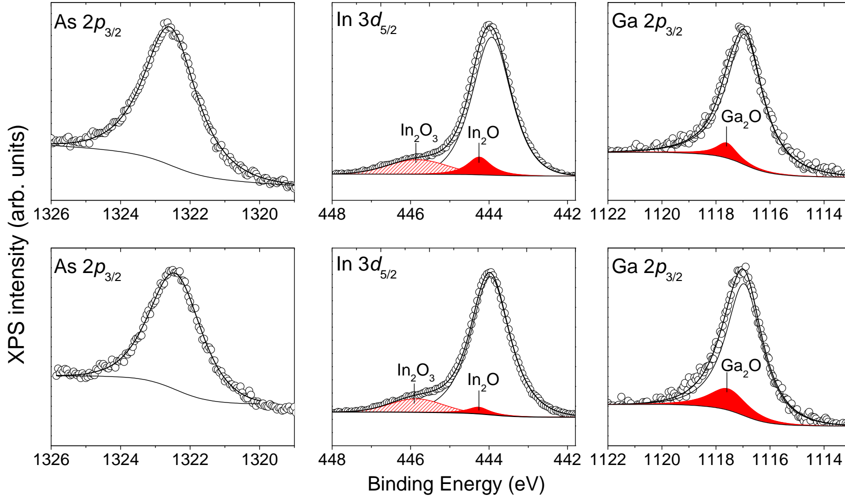

Figure 3.7: XPS spectra of As $2p_{3/2}$, In $3d_{5/2}$ and Ga $2p_{3/2}$ lines lines upon Al_2O_3 deposition on (2×4) reconstruction (top panel) and after post-deposition annealing (bottom panel). Similar results have been obtained for the (4×2) case.

Al_2O_3 on (2×4) reconstruction (top panel) and the same lines after PDA on the same reconstruction (bottom panel). Similar results have been obtained for the (4×2) case (data not shown). The As $2p_{3/2}$ lines of both interfaces are rid of As oxides irrespectively of the pristine surface reconstruction. This result is also confirmed by probing the As $3d$ line (Fig. 3.8). The absence of As oxides is a good starting point in order to achieve an effective passivation [13]. On the contrary, In $3d_{5/2}$ and Ga $2p_{3/2}$ lines present extra-component along with the bulk one. For the In case, in both interfaces, the extra-component can be associated with the presence of two different chemical states In^{1+} (In_2O) and In^{3+} (In_2O_3) [36], with the amount of the former one being lower than the latter. In the Ga $2p_{3/2}$ lines the extra-component can be associated with the formation of Ga_2O because the chemical shift is 0.6 eV for both reconstructions (Fig. 3.7) [37]. After PDA the As $2p_{3/2}$ still presents no oxides, the In_2O content decreases and In_2O_3 is fairly unaffected whereas the amount of Ga_2O increases (Fig. 3.7) but it is not assumed to be responsible for Fermi level pinning [37]. This increase in Ga_2O content could be likely associated with the concomitant In_2O decrease or with the presence of O_2 during PDA. In Fig. 3.8 the Al $2p$ lines confirm in both reconstructions the presence of the Al^{3+} oxidation state at ∼75 eV which is consistent with the formation of Al_2O_3 [45]. An additional minor Al component at lower binding energy, ∼73 eV, denoted with Al* (green curves in Fig. 3.8), can be associated with an interplay between Al-Al bond and Al-(InGaAs) bond [46]. Nevertheless, the reactive deposition technique ensures a good reactivity of the Al metallic flux in presence of O_2. In fact, the use of O_2 leads to a reduced oxidation of the semiconductor substrate with respect the use

of other more reactive oxidizers, e.g. atomic oxygen, and yields a chemical shift of the Al^{3+} component in the Al $2p$ line (with respect to the Al^* component) of 2.17 eV and 1.67 eV for the (2×4) and (4×2) reconstruction respectively, which is consistent with sesquioxide stoichiometry bonding (Fig. 3.8) [45]. The Al^* component does not vary its binding energy before and after PDA in the $Al_2O_3/In_{0.53}Ga_{0.47}As$-$(2 \times 4)$ interface, whereas different energetic position is found in the $Al_2O_3/In_{0.53}Ga_{0.47}As$-$(4 \times 2)$ case. It could be possible that in the (2×4) reconstruction, i.e. an As-rich surface, the Al-(InGaAs) part of Al^* may be dominated by Al-As bonding. This bonding could be stable after PDA, leaving the Al^* peak unaltered. On the other hand, in the (4×2) reconstruction, i.e. a group III-rich surface, the Al-(InGaAs) part of Al^* could be more equally shared by In and Ga. Since Ga and Al have similar electronegativities, the slight shift after PDA can be explained with a more balanced interplay between Al-(InGaAs) and Al-Al bond, with an increase of this latter component.

3.6 Effect of electric dipoles on Fermi level position

The reason why the interface is only partially pinned after Al_2O_3 deposition can be found in the limited In and Ga oxidation. Nonetheless, partial Fermi level unpinning observed from STS data can be elucidated by means of XPS investigation of the electronic bandstructure at the $Al_2O_3/In_{0.53}Ga_{0.47}As$ interface. Indeed, it is well-known from Kraut's determination of the interface band line-up that the valence band offset (VBO) in an oxide-semiconductor heterojunction can be inferred by measuring the mutual energy separation between XPS lines of the semiconductor and of the oxide with respect to the corresponding valence band edges [47]. Eq. 3.1 reports the Kraut's formula applied to the present case:

$$\begin{aligned}\Delta E_v = {} & |E_{Al_2O_3} - E_{InGaAs}|_{Al_2O_3/InGaAs} - (|E_{Al_2O_3} - E_v|_{Al_2O_3} \\ & - |E_{InGaAs} - E_v|_{InGaAs})\end{aligned} \tag{3.1}$$

where E indicates the binding energy (BE) of one element of Al_2O_3 or $In_{0.53}$-$Ga_{0.47}As$ and E_v is the respective valence band edge. In particular, as previously reported in Gd_2O_3/Ge heterojunction [48], process-dependent increase (decrease) of the absolute energy difference Δ_{O-S} between an oxide and a semiconductor XPS line results in an increase (decrease) of the VBO provided that some requirements are fulfilled. First, no change in the composition and/or stoichiometry takes place in the oxide or at the interface level. Second, no band bending occurs in the semiconductor. It can be noticed that the $\Delta_{O-S}(\mathrm{O}1s - \mathrm{As}3d) = \mathrm{BE}(\mathrm{O}1s) - \mathrm{BE}(\mathrm{As}3d)$ undergoes a sensible decrease when measured after annealing with respect to the as-grown Al_2O_3 as is evidenced in Fig. 3.8a for the (2×4) reconstructed surface and in Fig. 3.8b for the (4×2) one by using the As $3d$ and the O $1s$ lines as representative for the semiconductor and

Table 3.1: XPS absolute energy differences for as-grown Al_2O_3 on (2×4) reconstruction (a), after annealing at 200 °C (b), as-grown Al_2O_3 on (4×2) reconstruction (c), and after annealing at 200 °C (d). Uncertainty is ±0.08 eV.

Sample	$\Delta(O1s - As3d)$ (eV)	$\Delta(O1s - In3d_{5/2})$ (eV)	$\Delta(Ga2p_{3/2} - O1s)$ (eV)	$\Delta(O1s - Al2p)$ (eV)	$\Delta(Al2p - As3d)$ (eV)
a	491.73	88.35	584.65	456.90	34.81
b	491.15	87.72	585.29	456.79	34.37
c	491.58	88.28	584.67	456.89	34.66
d	491.18	87.80	585.15	456.86	34.33

the oxide, respectively. In detail, the quantitative amounts of the Δ_{O-S} as a function of the semiconductor lines, As $3d$, Ga $2p_{3/2}$, In $3d_{5/2}$, are reported in Tab. 3.1 for each process stage. A unequivocal trend appears irrespectively of the choice of the XPS lines. Indeed, from Tab. 3.1 it is possible to conclude that the decrease of the Δ(O1s – As3d) term is a common feature of all semiconductor lines which can be associated with a corresponding decrease of the VBO after annealing. This assignment is justified by the annealing-independent observation of a constant energy separation between the O 1s and Al 2p XPS lines, which is indicative of a stoichiometric invariance, and of the fixed position of all the semiconductor lines, which is indicative of no distortion of semiconductor electronic bands (see, for example, As 3d line in Fig. 3.8). A number of physical mechanisms can be invoked to interpret this annealing-induced VBO reduction; however the more likely event can be related to the relaxation of positively charged defects, e.g. Al dangling bonds [49] or fixed positive charge [50]. As similarly observed at the Al_2O_3/GaAs interface [50], accumulation of positive charges in the as-grown Al_2O_3 can produce an interface dipole which might result in the observed increase of the VBO by bending the oxide electronic bands with respect to a flat band condition. From this point of view, annealing the Al_2O_3 restores the flat band condition which descends from the suppression of the interface dipole and to the decrease of the VBO compared to the as-grown $Al_2O_3/In_{0.53}Ga_{0.47}As$ interface. It should be noticed that the assumed positive charge is intrinsic of the as-grown Al_2O_3 (and not other interfacial oxide species) because the VBO decrease is similarly reproduced by taking into account the Al 2p as oxide-related XPS line instead of the O 1s line (see Tab. 3.1). The presence of positive charges in the as-grown Al_2O_3 can be also supported by the evidence of a process-dependent chemical shift between the Al^{3+} and Al^* components in the Al 2p line in Fig. 3.8 which amounts to 2.17 eV and 1.82 eV for the (2×4) reconstruction in the as-grown and annealed Al_2O_3, respectively. A similar chemical shift is observed in the (4×2) reconstruction which amounts to 1.67 eV and 1.59 eV for as-grown and annealed cases, respectively. As the chemical shift can be influenced by coulombic attraction between photoemitted electrons and residing charges, the higher chemical shift measured in the as-grown Al_2O_3 is consistent with an extra positive charge in the oxide which affects the core level photoemission of Al

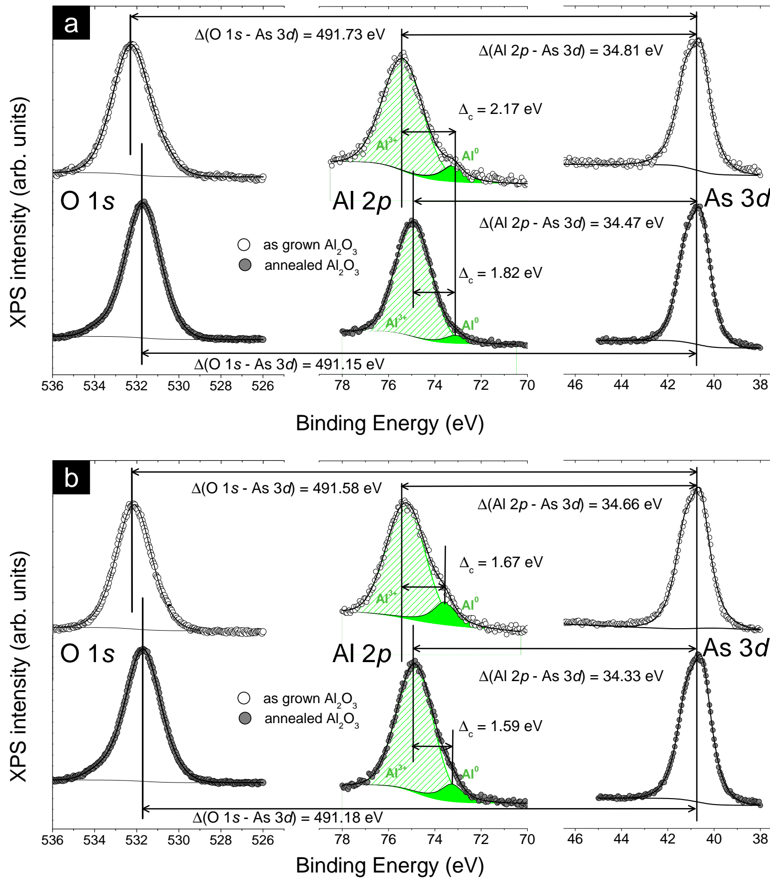

Figure 3.8: O 1s, Al 2p, and As 3d XPS lines for Al_2O_3 on (2×4) reconstruction as grown (top) and after annealing (bottom) (a) and for the (4×2) case (b). Doublets have been used to account for spin-orbit splitting ($\sim$0.68 eV) in the As 3d XPS line.

2p electrons. Although oxide charging can not be completely excluded, mainly due to the inability to exploit commonly used references [51], e.g. the C signal, it is noteworthy to underline that a comparative analysis of XPS level energy separation between samples with similar thickness has been considered with the aim to explain the presence of positive charges in the as-grown oxide. No precise determination of VBO value is here intended because it is beyond the scope of the present work. A second relevant effect can be associated with the above picture which can elucidate the phenomenology of the STS evidences. Besides bending the Al_2O_3 electronic bands, an interface dipole generated by positive charges in the as-grown Al_2O_3 can electrically screen the hole accumulation observed in the as-prepared $In_{0.53}Ga_{0.47}As$ surfaces then resulting in the partial Fermi level unpinning reported in Fig. 3.6. The back-shift of the interface

Fermi level after annealing can be regarded as a consequence of the dipole suppression due to charge relaxation. As no reconstruction-dependent interface composition can be deduced from the XPS inspection, the different extent of the back-shift between the two $In_{0.53}Ga_{0.47}As$ reconstructions necessarily claims for a mutually different annealing-induced bond or structural rearrangement [44]. This assumption is consistent with different values of the surface roughness extracted from the annealed Al_2O_3 grown on (2×4) and (4×2) reconstructed $In_{0.53}Ga_{0.47}As$, respectively.

3.7 Conclusions

Two distinct $In_{0.53}Ga_{0.47}As$ reconstructions have been investigated by STM, STS, and XPS. Their different peculiar surface reactivity and interaction with the initial TMA pulse suggests that a whole *in situ* approach could better elucidate the passivation mechanisms at the interfaces between $In_{0.53}Ga_{0.47}As$ and the high-κ oxide Al_2O_3. In this framework, it is possible to demonstrate that Al_2O_3 can partially unpin the $In_{0.53}Ga_{0.47}As$-(2×4) and (4×2) reconstructions and that PDA at 200 °C in molecular oxygen atmosphere results in a reconstruction-dependent behavior which could be ascribed to a different rearrangement of the chemical bonds at the very interface. In particular, the original Fermi level pinned condition is restored in a different extent depending on the surface reconstruction. This behavior is rationalized in terms of an interface dipole induced by positive charges in the as-grown oxide which are suppressed upon annealing as results from *in situ* XPS investigation of the change in the electron band line up at the interface between the oxide and the semiconductor. From STM/STS and XPS data, when capped with MBE-grown ultra-thin Al_2O_3 layers, the (2×4) reconstruction is more suitable to maintain Fermi level partially unpinned in a wider temperature range than the (4×2) reconstruction does, thus proving to be more favorable for application-oriented perspectives of $In_{0.53}Ga_{0.47}As$ as an active channel in MOSFET devices.

Bibliography

[1] J. A. del Alamo, *Nature* **479**, 317 (2011)

[2] ITRS: The International Technology Roadmap for Semiconductors (www.itrs.net)

[3] W. E. Spicer, I. Lindau, P. Skeath, and C. Y. Su, *J. Vac. Sci. Technol.* **17**, 1019 (1980)

[4] P. Kruse, J. G. McLean, and A. C. Kummel, *J. Chem. Phys.* **113**, 9224 (2000)

[5] C. L. Hinkle, A. M. Sonnet, E. M. Vogel, S. McDonnell, G. J. Hughes, M. Milojevic, B. Lee, F. S. Aguirre-Tostado, K. J. Choi, H. C. Kim, J. Kim, and R. M. Wallace, *Appl. Phys. Lett.* **92**, 071901 (2008)

[6] M. Scarrozza, G. Pourtois, M. Houssa, M. Caymax, A. Stesmans, M. Meuris, and M. M. Heyns, *Appl. Phys. Lett.* **95**, 253504 (2009)

[7] H. Becke, R. Hall, and J. White, *Solid State Electron.* **8**, 813 (1965)

[8] T. Mimura, K. Odani, N. Yokoyama, Y. Nakayama, and M. Fukuta, *IEEE Trans. Electron Devices* **25**, 573 (1978)

[9] M. Passlack, M. Hong, and J. P. Mannaerts, *Appl. Phys. Lett.* **68**, 1099 (1996)

[10] F. Ren, M. Hong, W. S. Hobson, J. M. Kuo, J. R. Lothian, J. P. Mannaerts, J. Kwo, S. N. G. Chu, Y. K. Chen, and A. Y. Cho, *Solid State Electron.* **41**, 1751 (1997)

[11] P. D. Ye, G. D. Wilk, J. Kwo, B. Yang, H. J. L. Gossmann, M. Frei, S. N. G. Chu, J. P. Mannaerts, M. Sergent, M. Hong, K. K. Ng, and J. Bude, *IEEE Electron Device Lett.* **24**, 209 (2003)

[12] M. M. Frank, G. D. Wilk, D. Starodub, T. Gustafsson, E. Garfunkel, Y. J. Chabal, J. Grazul, and D. A. Muller, *Appl. Phys. Lett.* **86**, 152904 (2005)

[13] M. L. Huang, Y. C. Chang, C. H. Chang, Y. J. Lee, P. Chang, J. Kwo, T. B. Wu, and M. Hong, *Appl. Phys. Lett.* **87**, 252104 (2005)

[14] Y. Xuan, H. C. Lin, P. D. Ye, and G. D. Wilk, *Appl. Phys. Lett.* **88**, 263518 (2006)

[15] N. Li, E. S. Harmon, J. Hyland, D. B. Salzman, T. P. Ma, Y. Xuan, and P. D. Ye, *Appl. Phys. Lett.* **92**, 143507 (2008)

[16] Y. Q. Wu, Y. Xuan, T. Shen, P. D. Ye, Z. Cheng, and A. Lochtefeld, *Appl. Phys. Lett.* **91**, 022108 (2007)

[17] H. D. Trinh, E. Y. Chang, P. W. Wu, Y. Y. Wong, C. T. Chang, Y. F. Hsieh, C. C. Yu, H. Q. Nguyen, Y. C. Lin, K. L. Lin, and M. K. Hudait, *Appl. Phys. Lett.* **97**, 042903 (2010)

[18] B. Brennan, M. Milojevic, C. L. Hinkle, F. S. Aguirre-Tostado, G. Hughes, and R. M. Wallace, *Appl. Surf. Sci.* **257**, 4082 (2011)

[19] Y. D. Wu, T. D. Lin, T. H. Chiang, Y. C. Chang, H. C. Chiu, Y. J. Lee, M. Hong, C. A. Lin, and J. Kwo, *J. Vac. Sci. Technol. B* **28**, C3H10 (2010)

[20] H. Hasegawa and M. Akazawa, *Appl. Surf. Sci.* **254**, 8005 (2008)

[21] R. Engel-Herbert, Y. Hwang, J. I. Cagnon, and S. Stemmer, *Appl. Phys. Lett.* **95**, 062908 (2009)

[22] P. D. Ye, Y. Xuan, Y. Wu, and M. Xu, *ECS Trans.* **19**, 605 (2009)

[23] W. M. Lau, R. N. S. Sodhi, S. Jin, S. Ingrey, N. Puetz, and A. SpringThorpe, *J. Appl. Phys.* **67**, 768 (1990)

[24] S. Ohkouchi and A. Gomyo, *Appl. Surf. Sci.* **130-132**, 447 (1998)

[25] J. Mirecki Millunchick, A. Riposan, B. J. Dall, C. Pearson, and B. G. Orr, *Surf. Sci.* **550**, 1 (2004)

[26] P. A. Bone, J. M. Ripalda, G. R. Bell, and T. S. Jones, *Surf. Sci.* **600**, 973 (2006)

[27] A. Chakrabarti, P. Kratzer, and M. Scheffler, *Phys. Rev. B* **74**, 245328 (2006)

[28] J. Shen, D. Winn, W. Melitz, J. Clemens, and A. C. Kummel, *ECS Trans.* **16**, 463 (2008)

[29] V. P. LaBella, H. Yang, D. W. Bullock, and P. M. Thibado, *Phys. Rev. Lett.* **83**, 2989 (1999)

[30] C. Ratsch, W. Barvosa-Carter, F. Grosse, J. H. G. Owen, and J. J. Zinck, *Phys. Rev. B* **62**, R7719 (2000)

[31] C. Kendrick, G. Le Lay, and A. Kahn, *Phys. Rev. B* **54**, 17877 (1996)

[32] J. Shen, J. B. Clemens, E. A. Chagarov, D. L. Feldwinn, W. Melitz, T. Song, S. R. Bishop, A. C. Kummel, and R. Droopad, *Surf. Sci.* **604**, 1757 (2010)

[33] H. P. Komsa and A. Pasquarello, *Appl. Phys. Lett.* **97**, 191901 (2010)

[34] D. A. Shirley, *Phys. Rev. B* **5**, 4709 (1972)

[35] L. Lamagna, M. Fusi, S. Spiga, M. Fanciulli, G. Brammertz, C. Merckling, M. Meuris, and A. Molle, *Microelectr. Eng.* **88**, 431 (2011)

[36] A. P. Kirk, M. Milojevic, J. Kim, and R. M. Wallace, *Appl. Phys. Lett.* **96**, 202905 (2010)

[37] C. L. Hinkle, M. Milojevic, B. Brennan, A. M. Sonnet, F. S. Aguirre-Tostado, G. J. Hughes, E. M. Vogel, and R. M. Wallace, *Appl. Phys. Lett.* **94**, 162101 (2009)

[38] A. Molle, G. Brammertz, L. Lamagna, M. Fanciulli, M. Meuris, and S. Spiga, *Appl. Phys. Lett.* **95**, 023507 (2009)

[39] H. C. Lin, W. E. Wang, G. Brammertz, M. Meuris, and M. Heyns, *Microelectr. Eng.* **86**, 1554 (2009)

[40] A. O'Mahony, S. Monaghan, G. Provenzano, I. M. Povey, M. G. Nolan, E. O'Connor, K. Cherkaoui, S. B. Newcomb, F. Crupi, P. K. Hurley, and M. E. Pemble, *Appl. Phys. Lett.* **97**, 052904 (2010)

[41] J. B. Clemens, S. R. Bishop, D. L. Feldwinn, R. Droopad, and A. C. Kummel, *Surf. Sci.* **603**, 2230 (2009)

[42] M. Fusi, L. Lamagna, S. Spiga, M. Fanciulli, G. Brammertz, C. Merckling, M. Meuris, and A. Molle, *Microelectr. Eng.* **88**, 435 (2011)

[43] J. B. Clemens, S. R. Bishop, J. S. Lee, A. C. Kummel, and R. Droopad, *J. Chem. Phys.* **132**, 244701 (2010)

[44] J. Shen, E. A. Chagarov, D. L. Feldwinn, W. Melitz, N. M. Santagata, A. C. Kummel, R. Droopad, and M. Passlack, *J. Chem. Phys.* **133**, 164704 (2010)

[45] I. Olefjord, H. J. Mathieu, and P. Marcus, *Surf. Interface Anal.* **15**, 681 (1990)

[46] B. Brennan, M. Milojevic, R. Contreras-Guerrero, H. C. Kim, M. Lopez-Lopez, J. Kim, and R. M. Wallace, *J. Vac. Sci. Technol. B* **30**, 04E104 (2012)

[47] E. A. Kraut, R. W. Grant, J. R. Waldrop, and S. P. Kowalczyk, *Phys. Rev. Lett.* **44**, 1620 (1980)

[48] M. Perego, A. Molle, and M. Fanciulli, *Appl. Phys. Lett.* **92**, 042106 (2008)

[49] B. Shin, J. R. Weber, R. D. Long, P. K. Hurley, C. G. Van de Walle, and P. C. McIntyre, *Appl. Phys. Lett.* **96**, 152908 (2010)

[50] J. Hu, A. Nainani, Y. Sun, K. C. Saraswat, and H. S. P. Wong, *Appl. Phys. Lett.* **99**, 252104 (2011)

[51] M. Perego and G. Seguini, *J. Appl. Phys.* **110**, 053711 (2011)

Chapter 4

2D materials: overview

> I call our world Flatland, not because we call it so, but to make its nature clearer to you, my happy readers, who are privileged to live in Space
>
> a square

4.1 From 3D to 2D materials

In the 1930s, Peierls and Landau argued that purely two-dimensional (2D) crystals were thermodynamically unstable and could not exist [1, 2]. Their theory pointed out that a divergent contribution of thermal fluctuations in low-dimensional crystal lattices should lead to a displacement of atoms comparable to interatomic distances at any finite temperature, thus making energetically unfavorable the crystal formation [3]. The argument was later extended by Mermin [4] and was strongly supported by experimental observations. Indeed, the melting temperature of thin films rapidly decreases with decreasing thickness until the films become unstable, segregating into islands or decomposing, at a thickness of, typically, dozens of atomic layers [5, 6]. Therefore, the long-range ordering (crystallographic or magnetic) in 2D at any finite temperature was thought to be theoretically impossible. For this reason, atomic monolayers were known only as an integral part of larger three-dimensional (3D) structures, e.g. graphite, and usually grown epitaxially on top of monocrystals with matching crystal lattices. Without such a 3D base, 2D materials were presumed not to exist until 2004, when the experimental identification of graphene [7] and other freestanding 2D atomic crystals (see below) occurred. These 2D crystals exhibit high crystal quality and could be obtained on top of non-crystalline substrates [7, 8], in liquid suspension [7], and as suspended membranes [9]. *A posteriori*, the existence of these one-atom-thick crystals can be reconciled with theory. Indeed, it can be argued that the obtained 2D crystals are quenched in a metastable state because they are extracted from 3D materials, whereas

their small size ($\ll 1\,\text{mm}$) and strong interatomic bonds ensure that thermal fluctuations cannot lead to the generation of dislocations or other crystal defects even at elevated temperature [10]. Moreover, the extracted 2D crystals become intrinsically stable by gentle crumpling in the third dimension [9]. Such 3D warping leads to a gain in elastic energy but suppresses thermal vibrations, which above a certain temperature can minimize the total free energy [11].

4.2 Flatland

After the discoveries of graphene's unusual properties in 2004 by Nobel prizewinners Geim and Novoselov (awarded in 2010), a new branch of condensed matter physics started. This field is mainly devoted to study the fascinating properties of 2D material like X-enes (graphene, silicene, and germanene), X-anes (graphane, silicane, and germanane), and transition metal dichalcogenides (TMDs). With reference to the "romance of many dimensions" published in 1884 by Abbott, nowadays these materials are pictorially grouped under the name *Flatland*. The 2D materials family is characterized by one-atom-thick materials showing different properties but with similar problems related to their synthesis. The importance of graphene is not only that it has unique properties but also that it has paved the way for the isolation and synthesis of many other 2D materials [8]. Nowadays it is possible to consider a whole new class of materials, 2D atomic crystals, with a large variety of properties ranging from large bandgap insulators to the very best conductors, from the extremely mechanically strong to the soft and fragile, and from the chemically active to the very inert. Experience on graphene provided different possible methods for obtaining other 2D crystals. For example, micromechanical or chemical exfoliation can be successfully applied to other layered materials such as $Bi_2Sr_2CaCu_2O_x$, $NbSe_2$, BN, MoS_2, Bi_2Te_3, and many other dichalcogenides [8, 12, 13] and epitaxial growth has been applied to grow monolayers of BN [14] and recently silicene (see Chapt. 5) [15, 16]. The properties of the obtained 2D materials might be very different from those of their 3D precursors. For example, the overlapping between the valence and conduction bands in graphene is exactly zero while it is finite in graphite [7] and a monolayer of MoS_2 is a direct band semiconductor while the bulk material has an indirect bandgap [12]. By combining the different properties of the aforementioned materials, it will be probably imaginable, in the near future, to create new 3D stacked materials based on 2D layers. Indeed, it will be possible to fully control 2D crystals, thus creating stacks (not merely of the same material) of these crystals according to the desired requirements. Insulating, conducting, probably superconducting, and magnetic layers can all be combined in one layered material as desired, thus tuning the properties of such heterostructures depending on the stacking order.

4.3 Graphene

Graphene, the 2D honeycomb arrangement of carbon atoms, is nowadays one of the most important material either for fundamental physics properties or technological aspects. Carbon atoms in graphene are sp^2 hybridized, meaning that only three valence electrons form the strong σ bonds and the fourth has a communal use forming the so-called π bonds. Hence, graphene is a zero-overlap semimetal and conducts electricity very well, in contrast to diamond, where each carbon atom is in sp^3 hybridization and therefore has four equivalent neighbors. A large number of its properties, such as mechanical stiffness, strength and elasticity, very high electrical and thermal conductivity, and many others are supreme [10, 17]. Many graphene characteristics measured in experiments have exceeded those obtained in any other material, with some of them reaching theoretically predicted limits: room temperature electron mobility of $2.5 \times 10^5\,\mathrm{cm^2V^{-1}s^{-1}}$ [18] (theoretical limit $\sim 2 \times 10^5\,\mathrm{cm^2V^{-1}s^{-1}}$ [19]), a Young's modulus of 1 TPa and intrinsic strength of 130 GPa [20, 21], very high thermal conductivity (above 3.000 $\mathrm{WmK^{-1}}$ [22]), optical absorption of exactly $\pi\alpha < 2.3\%$ (in the infrared limit, where α is the fine structure constant) [23], complete impermeability to any gases [24], ability to sustain extremely high densities of electric current [25], e.g. a million times higher than copper. Another property of graphene is that it can be chemically functionalized [26–28]. However, some of these features have been achieved only for the highest quality samples made by mechanically exfoliated graphene or for graphene deposited on special substrates like hexagonal BN. Although interest in graphene exploded in 2004, after the two seminal papers [7, 29], the history of this material goes back much further. Indeed, even in 1947, when the name graphene did not exist yet, Wallace calculated the bandstructure of a single layer of carbon atoms arranged in a honeycomb 2D lattice, i.e. graphene, therein predicting its gapless nature [30]. In the 1960s, single graphene layers were produced by the reduction of graphite oxide [31] and observed on platinum [32] whereas in 1975, graphene has been produced by the thermal decomposition of SiC [33]. Initially, however, these results found only limited attention in the community. It was only in 1994 that the name graphene has been introduced for single carbon layers of the graphitic structure [34]. After the discoveries of graphene's extraordinary properties in 2004, an exponential and rapid increase in graphene research allowed to conceive the first graphene transistor just in 2007 [35]. A detailed discussion of graphene's properties, in particular electronic properties, is beyond the scope of the present work. However, in order to understand similarities and differences with other 2D material, in particular silicene (see Chapt. 5), a brief resume of the principal electronic properties (extensively discussed in detail in Refs. [36, 37]) is necessary. In condensed matter physics, the Schrödinger equation is usually quite sufficient to describe electronic properties of materials. Graphene is an exception since its charge carriers mimic relativistic particles and are more easily and naturally described starting with the Dirac

equation rather than the Schrödinger equation [10]. Electrons moving around carbon atoms interact with the periodic potential of graphene's honeycomb lattice giving rise to new quasi-particles that at low energies are accurately described by the (2+1)-dimensional Dirac equation with an effective speed of $v_F \approx 10^6\,\mathrm{m/s}$. These quasi-particles, called massless Dirac fermions, can be seen as electrons that have lost their rest mass or as neutrinos that acquired the electron charge [10, 38]. The relativistic-like description of electron waves on honeycomb lattices provides a way to probe quantum electrodynamics (QED) phenomena by measuring graphene's electronic properties. The hexagonal honeycomb lattice of graphene, with two carbon atoms per unit cell, leads to a rather unique bandstructure, where the π states form the valence band and the π^* states the conduction band. These two bands touch at six points, the so-called Dirac or neutrality points. Symmetry allows to reduce these six points to a pair, K and K', which are independent of one another. Hence, graphene is a zero-gap semiconductor, in which low energy quasi-particles within each valley can formally be described by the Dirac-like Hamiltonian:

$$H = \hbar v_F \begin{pmatrix} 0 & k_x - ik_y \\ k_x + ik_y & 0 \end{pmatrix} = \hbar v_F \sigma \cdot \mathbf{k} \tag{4.1}$$

where $\mathbf{k}$ is the quasiparticle momentum, σ the 2D Pauli matrix, and the k-independent Fermi velocity v_F plays the role of the speed of light. The Dirac equation is a direct consequence of graphene's crystal symmetry. Its honeycomb lattice is made up of two equivalent carbon sublattices A and B, and cosine-like energy bands associated with the sublattices intersect at zero E near the edges of the Brillouin zone, giving rise to conical sections of the energy spectrum for $|E| < 1\,\mathrm{eV}$. Thus, the absence of a gap between the valence and conduction bands is a consequence of the symmetry between the sublattices [39] in contrast to, for example, BN where the symmetry between the sublattices is broken (one consists of boron, another of nitrogen) and a large gap is opened in the electronic bandstructure. Electronic states near zero E, where the bands intersect, are composed of states belonging to the different sublattices and their relative contributions in the make-up of quasi-particles have to be taken into account by, for example, using two-component wavefunctions (spinors). This requires an index to indicate sublattices A and B, which is similar to the spin index (up and down) in QED and, therefore, is referred to as pseudospin. Accordingly, in the formal description of graphene's quasiparticles by the Dirac-like hamiltonian (Eq. 4.1), σ refers to pseudospin rather than the real spin of electrons, which must be described by additional terms in the hamiltonian. Importantly, QED specific phenomena are often inversely proportional to the speed of light c and therefore enhanced in graphene by a factor $c/v_F \approx 300$ [10]. In particular, this means that pseudospin-related effects should generally dominate those due to the real spin. By analogy with QED, a quantity called chirality [40] is introduced and is formally a projection of σ on the direction of motion $\mathbf{k}$

and is positive (negative) for electrons (holes). In essence, chirality in graphene means that k electron and $-k$ hole states are intricately connected because they originate from the same carbon sublattices. The concepts of chirality and pseudospin are important because many electronic processes in graphene can be understood as due to conservation of these quantities [10, 40]. Graphene, but also other 2D materials, offers truly unique opportunities because, unlike in most semiconductor systems, its 2D electronic states are not buried deep under the surface and can be accessed directly by tunneling and other local probes. Therefore, many interesting results can be expected to arise from scanning probe experiments [10].

4.4 Beyond graphene

There exists an entire periodic table of crystalline 2D solid-state materials with different electronic, mechanical, and transport properties. It was shown decades ago by Frindt that layered van der Waals materials, e.g. layered metal dichalcogenides, could be mechanically and chemically exfoliated into few and single layers [41]. Additionally, the efforts in graphene research have yielded many methods for synthesizing, transferring, detecting, characterizing, and manipulating the properties of layered van der Waals materials. These established methods have enabled the field of 2D materials beyond graphene to mature very quickly. In general, there are two main classes of single and few layers 2D materials [42]. The most common class of crystalline structures that can be exfoliated, as stable single layers, are the layered van der Waals solids. These crystal structures are composed by neutral, single-atom-thick or polyhedral-thick layers of atoms that are covalently or ionically connected with their neighbors within each layer, whereas the layers are held together via van der Waals bonding along the out of plane axis. The weak interlayer van der Waals energies (∼40-70 meV) enable the easy exfoliation of these layers [42]. The most conventional and simple approaches for obtaining single and few layers thick 2D materials from many of these solids include mechanical exfoliation of large crystals, chemical exfoliation by dispersing in a solvent with the appropriate surface tension, and molecule/atom intercalation in order to exfoliate these layers and enable their dispersion in polar solvents [8, 42, 43]. The mechanical exfoliation process has been used to prepare and study the properties of few layers van der Waals materials, such as MoS_2 and $NbSe_2$, since the 1960s [41, 44]. The isolation of individual and few layers using mechanical exfoliation remains the most powerful approach for studying their properties (but it is not suitable for large scale industrial production), since it is considerably less destructive than the other methods and has been successfully used to create large, ∼10 µm in diameter, single layer flakes on a variety of substrates. One of the most well-studied families of van der Waals solids is the TMDs, the most common being MoS_2. TMDs with stoichiometry MX_2 (M = Ti, Zr, Hf, V, Nb, Ta, Re; X

= S, Se, Te) crystallize into layered 2D structures in which hexagonally packed MX_6 octahedra or trigonal prisms share edges with their six nearest MX_6 neighbors within each layer [45–48]. Theoretical calculations based on structure optimization predict that, out of 88 different combinations of MX_2 compounds, several of them can be stable in freestanding, single layer honeycomb-like structures [49]. However, so far, only very few MX_2 compounds have been synthesized as suspended single layers or exfoliated as thin sheets. Other families of van der Waals solids that have been exfoliated into single layers include hexagonal BN [50] and other chalcogenides such as Bi_2Te_3, Sb_2Te_3, and Bi_2Se_3, with topological properties [51, 52]. Many novel van der Waals compounds can be created via the topotactic deintercalation of precursor solids. For example, the layered $CaGe_2$ and $CaSi_2$ Zintl phases can be topochemically deintercalated in aqueous HCl to produce layered hydrogen-terminated GeH or half-hydrogen-terminated/half-hydroxy-terminated $SiH_{0.5}(OH)_{0.5}$ [42, 53]. These group IV graphane analogues, e.g. germanane [53], are a new intriguing class of systems due to the possibility of utilizing covalent chemistry to modulate and tune their properties. Finally, the second class considers non-layered materials which can give 2D layer by means of surface growth. Indeed, the deposition of materials on substrates offers the potential to grow and study the properties of single or few atom-thick materials beyond those existing as layered bulk crystals. For example, recently, it was demonstrated that monolayers of silicon deposited on Ag(111), Ir(111) or $ZrB_2(0001)$ organize into a puckered hexagonal graphene-like lattice with sp^2/sp^3 bonding configuration (see Chap. 5) [15, 16, 47, 48, 54, 55]. Additionally, ultra-thin insulators such as Al_2O_3 [56], NaCl [57], MgO [58], TiO_2 [59], and ZnO [60] have been prepared in this fashion on metal substrates. Unlike exfoliation, the choice of substrate has been typically limited to metals due to the prevalence of scanning tunneling microscope as a characterization tool. Indeed, to date, the real challenge is growing these 2D materials on semiconducting or insulating substrates.

Bibliography

[1] R. E. Peierls, *Ann. I. H. Poincare* **5**, 177 (1935)

[2] L. D. Landau, *Phys. Z. Sowjetunion* **11**, 26 (1937)

[3] L. D. Landau and E. M. Lifshitz, Statistical Physics, Part I, Pergamon, Oxford (1980)

[4] N. D. Mermin, *Phys. Rev.* **176**, 250 (1968)

[5] J. A. Venables, G. D. T. Spiller, and M. Hanbucken, *Rep. Prog. Phys.* **47**, 399 (1984)

[6] J. W. Evans, P. A. Thiel, and M. C. Bartelt, *Surf. Sci. Rep.* **61**, 1 (2006)

[7] K. S. Novoselov, A. K. Geim, S. V. Morozov, D. Jiang, Y. Zhang, S. V. Dubonos, I. V. Grigorieva, and A. A. Firsov, *Science* **306**, 666 (2004)

[8] K. S. Novoselov, D. Jiang, F. Schedin, T. J. Booth, V. V. Khotkevich, S. V. Morozov, and A. K. Geim, *Proc. Natl. Acad. Sci.* **102**, 10451 (2005)

[9] J. C. Meyer, A. K. Geim, M. I. Katsnelson, K. S. Novoselov, T. J. Booth, and S. Roth, *Nature* **446**, 60 (2007)

[10] A. K. Geim and K. S. Novoselov, *Nature Mater.* **6**, 183 (2007)

[11] D. R. Nelson, T. Piran, and S. Weinberg, Statistical Mechanics of Membranes and Surfaces, World Scientific, Singapore (2004)

[12] K. F. Mak, C. Lee, J. Hone, J. Shan, and T. F. Heinz, *Phys. Rev. Lett.* **105**, 136805 (2010)

[13] D. Teweldebrhan, V. Goyal, and A. A. Balandin, *Nano Lett.* **10**, 1209 (2010)

[14] A. Nagashima, N. Tejima, Y. Gamou, T. Kawai, and C. Oshima, *Phys. Rev. Lett.* **75**, 3918 (1995)

[15] P. Vogt, P. De Padova, C. Quaresima, J. Avila, E. Frantzeskakis, M. C. Asensio, A. Resta, B. Ealet, and G. Le Lay, *Phys. Rev. Lett.* **108**, 155501 (2012)

[16] C. L. Lin, R. Arafune, K. Kawahara, N. Tsukahara, E. Minamitani, Y. Kim, N. Takagi, and M. Kawai, *Appl. Phys. Express* **5**, 045802 (2012)

[17] A. K. Geim, *Science* **324**, 1530 (2009)

[18] A. S. Mayorov, R. V. Gorbachev, S. V. Morozov, L. Britnell, R. Jalil, L. A. Ponomarenko, P. Blake, K. S. Novoselov, K. Watanabe, T. Taniguchi, and A. K. Geim, *Nano Lett.* **11**, 2396 (2011)

[19] S. V. Morozov, K. S. Novoselov, M. I. Katsnelson, F. Schedin, D. C. Elias, J. A. Jaszczak, and A. K. Geim, *Phys. Rev. Lett.* **100**, 016602 (2008)

[20] C. Lee, X. Wei, J. W. Kysar, and J. Hone, *Science* **321**, 385 (2008)

[21] F. Liu, P. Ming, and J. Li, *Phys. Rev. B* **76**, 064120 (2007)

[22] A. A. Balandin, *Nature Mater.* **10**, 569 (2011)

[23] R. R. Nair, P. Blake, A. N. Grigorenko, K. S. Novoselov, T. J. Booth, T. Stauber, N. M. R. Peres, and A. K. Geim, *Science* **320**, 1308 (2008)

[24] J. S. Bunch, S. S. Verbridge, J. S. Alden, A. M. van der Zande, J. M. Parpia, H. G. Craighead, and P. L. McEuen, *Nano Lett.* **8**, 2458 (2008)

[25] J. Moser, A. Barreiro, and A. Bachtold, *Appl. Phys. Lett.* **91**, 163513 (2007)

[26] D. C. Elias, R. R. Nair, T. M. G. Mohiuddin, S. V. Morozov, P. Blake, M. P. Halsall, A. C. Ferrari, D. W. Boukhvalov, M. I. Katsnelson, A. K. Geim, and K. S. Novoselov, *Science* **323**, 610 (2009)

[27] K. P. Loh, Q. Bao, P. K. Ang, and J. X. Yang, *J. Mater. Chem.* **20**, 2277 (2010)

[28] R. R. Nair, W. Ren, R. Jalil, I. Riaz, V. G. Kravets, L. Britnell, P. Blake, F. Schedin, A. S. Mayorov, S. Yuan, M. I. Katsnelson, H. M. Cheng, W. Strupinski, L. G. Bulusheva, A. V. Okotrub, I. V. Grigorieva, A. N. Grigorenko, K. S. Novoselov, and A. K. Geim, *Small* **6**, 2877 (2010)

[29] C. Berger, Z. Song, T. Li, X. Li, A. Y. Ogbazghi, R. Feng, Z. Dai, A. N. Marchenkov, E. H. Conrad, P. N. First, and W. A. de Heer, *J. Phys. Chem. B* **108**, 19912 (2004)

[30] P. R. Wallace, *Phys. Rev.* **71**, 622 (1947)

[31] H. P. Boehm, A. Clauss, G. O. Fischer, and U. Hofmann, *Z. Naturforschg.* **17**, 150 (1962)

[32] J. W. May, *Surf. Sci.* **17**, 267 (1969)

[33] A. J. van Bommel, J. E. Crombeen, and A. van Tooren, *Surf. Sci.* **48**, 463 (1975)

[34] H. P. Boehm, R. Setton, and E. Stumpp, *Pure Appl. Chem.* **66**, 1893 (1994)

[35] M. C. Lemme, T. J. Echtermeyer, M. Baus, and H. Kurz, *IEEE Electron Device Lett.* **28**, 282 (2007)

[36] A. H. Castro Neto, F. Guinea, N. M. R. Peres, K. S. Novoselov, and A. K. Geim, *Rev. Mod. Phys.* **81**, 109 (2009)

[37] S. Das Sarma, S. Adam, E. H. Hwang, and E. Rossi, *Rev. Mod. Phys.* **83**, 407 (2011)

[38] K. S. Novoselov, A. K. Geim, S. V. Morozov, D. Jiang, M. I. Katsnelson, I. V. Grigorieva, S. V. Dubonos, and A. A. Firsov, *Nature* **438**, 197 (2005)

[39] J. C. Slonczewski and P. R. Weiss, *Phys. Rev.* **109**, 272 (1958)

[40] F. D. M. Haldane, *Phys. Rev. Lett.* **61**, 2015 (1988)

[41] R. F. Frindt, *J. Appl. Phys.* **37**, 1928 (1966)

[42] S. Z. Butler, S. M. Hollen, L. Cao, Y. Cui, J. A. Gupta, H. R. Gutierrez, T. F. Heinz, S. S. Hong, J. Huang, A. F. Ismach, E. Johnston-Halperin, M. Kuno, V. V. Plashnitsa, R. D. Robinson, R. S. Ruoff, S. Salahuddin, J. Shan, L. Shi, M. G. Spencer, M. Terrones, W. Windl, and J. E. Goldberger, *ACS Nano* **7**, 2898 (2013)

[43] J. N. Coleman, M. Lotya, A. O'Neill, S. D. Bergin, P. J. King, U. Khan, K. Young, A. Gaucher, S. De, R. J. Smith, I. V. Shvets, S. K. Arora, G. Stanton, H. Y. Kim, K. Lee, G. T. Kim, G. S. Duesberg, T. Hallam, J. J. Boland, J. J. Wang, J. F. Donegan, J. C. Grunlan, G. Moriarty, A. Shmeliov, R. J. Nicholls, J. M. Perkins, E. M. Grieveson, K. Theuwissen, D. W. McComb, P. D. Nellist, and V. Nicolosi, *Science* **331**, 568 (2011)

[44] R. F. Frindt, *Phys. Rev. Lett.* **28**, 299 (1972)

[45] J. A. Wilson and A. D. Yoffe, *Adv. Phys.* **18**, 193 (1969)

[46] M. Chhowalla, H. S. Shin, G. Eda, L. J. Li, K. P. Loh, and H. Zhang, *Nature Chem.* **5**, 263 (2013)

[47] M. Xu, T. Liang, M. Shi, and H. Chen, *Chem. Rev.* **113**, 3766 (2013)

[48] Q. Tang and Z. Zhou, *Prog. Mat. Sci.* **58**, 1244 (2013)

[49] C. Ataca, H. Sahin, and S. Ciraci, *J. Phys. Chem. C* **116**, 8983 (2012)

[50] K. K. Kim, A. Hsu, X. Jia, S. M. Kim, Y. Shi, M. Hofmann, D. Nezich, J. F. Rodriguez-Nieva, M. Dresselhaus, T. Palacios, and J. Kong, *Nano Lett.* **12**, 161 (2012)

[51] D. Kong, W. Dang, J. J. Cha, H. Li, S. Meister, H. Peng, Z. Liu, and Y. Cui, *Nano Lett.* **10**, 2245 (2010)

[52] M. Z. Hasan and C. L. Kane, *Rev. Mod. Phys.* **82**, 3045 (2010)

[53] E. Bianco, S. Butler, S. Jiang, O. D. Restrepo, W. Windl, and J. E. Goldberger, *ACS Nano* **7**, 4414 (2013)

[54] A. Fleurence, R. Friedlein, T. Ozaki, H. Kawai, Y. Wang, and Y. Yamada-Takamura, *Phys. Rev. Lett.* **108**, 245501 (2012)

[55] L. Meng, Y. Wang, L. Zhang, S. Du, R. Wu, L. Li, Y. Zhang, G. Li, H. Zhou, W. A. Hofer, and H. J. Gao, *Nano Lett.* **13**, 685 (2013)

[56] A. J. Heinrich, J. A. Gupta, C. P. Lutz, and D. M. Eigler, *Science* **306**, 466 (2004)

[57] F. E. Olsson, S. Paavilainen, M. Persson, J. Repp, and G. Meyer, *Phys. Rev. Lett.* **98**, 176803 (2007)

[58] M. Sterrer, T. Risse, U. M. Pozzoni, L. Giordano, M. Heyde, H. P. Rust, G. Pacchioni, and H. J. Freund, *Phys. Rev. Lett.* **98**, 096107 (2007)

[59] D. V. Potapenko, J. Hrbek, and R. M. Osgood, *ACS Nano* **2**, 1353 (2008)

[60] C. Tusche, H. L. Meyerheim, and J. Kirschner, *Phys. Rev. Lett.* **99**, 026102 (2007)

Chapter 5

Silicene on Ag(111)

> The next generation of computers may still be made of silicon after all, only thinner
>
> J. Uhlrich

5.1 Theoretical background

About twenty years ago Takeda and Shiraishi theoretically considered the Si and Ge equivalents of graphite by first-principles calculations [1]. They found that, while C atoms prefer to arrange in a flat aromatic stage, i.e. graphite building block, Si and Ge atoms prefer instead to form corrugated aromatic stages. The z components of Hellmann-Feynmann forces acting on Si atoms of the unit cell induce a puckering effect which corrugates the Si stage changing D_{6h} symmetry into D_{3d} one. The most important aspect of this pioneering study is that corrugated stage results to be more stable than the flat one. The former configuration lengthen the Si-Si bond to 2.247 Å with respect to the 2.226 Å of the latter stage. Renewed interest in Si and Ge as obvious alternative of C raised after the first synthesis of carbon nanotubes [2] and mostly after graphene [3]. Guzman-Verri and Lew Yan Voon applied tight-binding models to study the electronic properties of silicon-based nanostructures [4]. In particular, they considered three different kinds of structures and one of them was named for the first time *silicene*. Hence, they referred to silicene, Si(111) monolayer, and Si hexagonal nanotubes. By their own definition "silicene is a two-dimensional (2D) sheet with a honeycomb lattice of lattice constant a made out of Si atoms which have sp^2 hybridization. Thus, silicene has the same structure as a graphene sheet but it is composed of Si atoms instead of C atoms". The authors also defined "a Si(111) layer has a lattice structure which is the same as the honeycomb lattice for silicene, except that one set of atoms is vertically displaced from the plane due to sp^3 bonding". This latter structure has basis vectors and unit cell equal to those of graphene (and silicene). For silicene

calculated bandstructure, a linear dispersion close to the K point was found with linearly fitted Fermi velocity of the order of 10^5 m/s. Lower Fermi velocity with respect to graphene, i.e. 10^6 m/s [5], occurs because π bonds, which are responsible for in plane conduction, are weaker and the atomic distance is greater than in graphene. Similarly to graphene, silicene π and σ bands are not coupled due to planar and orbital symmetries, but in the Si(111) configuration the sp^3 hybridization makes them coupling [4]. However, the π band is still doubly degenerate at the K point and this aspect ensures that hexagonal symmetry is conserved [6]. The puckered configuration of Si(111) monolayer preserves the linear dispersion relation close to the K point with fitted Fermi velocity of 10^4 m/s [4]. This difference in Fermi velocities in the two considered Si structures can be understood considering that in silicene each atom shows sp^2 hybridization, so its lobe points perpendicular to the sheet plane. All lobes are therefore oriented along the same direction thus forming π bond with their first near neighbor. On the other hand, Si(111) monolayer shows sp^3 hybridization which is responsible of π bonding not with first near neighbor but with the second one. Electrons move easier from one atom to another when the coupling is stronger. This explains why Fermi velocities are decreasing from graphene, silicene to Si(111) monolayer. Cahangirov and collaborators subsequently confirmed, by means of structure optimization, phonon modes, and finite temperature molecular dynamics, that Si and Ge can have stable 2D honeycomb structures [7]. In particular, they discussed different buckling extent distinguishing planar (PL), low-buckled (LB), and high-buckled (HB) structures. While the PL structure is the least energetic configuration and is not stable, LB honeycomb structure of Si is stable with an equilibrium buckling of 0.44 Å. HB (buckling of ≈ 2 Å) structures have imaginary phonon frequencies for large portion of Brillouin zone and they are believed to not correspond to a real local minimum. Nonetheless, they can occur under the constraint of (1×1) hexagonal lattice and they are expected to exhibit metallic behavior. Conversely, LB configurations are semimetallic with π and π^* bands crossing Fermi level at K and K' points, with estimated Fermi velocity of $\backsim 10^6$ m/s. Si and Ge LB structures show nearest neighbor distance of 2.25 Å and 2.38 Å, respectively [7]. Similar results were also obtained by Houssa *et al.* and by Liu *et al.*, which calculated Si-Si bond length of 2.26 Å [8] and 2.28 Å [9], respectively. Furthermore, Liu and collaborators predicted that the quantum spin Hall effect could be observed in an experimentally accessible low temperature (18 - 34 K) regime [9], thus demonstrating that silicene (but also 2D Ge) has non-trivial topological properties in its native structures.

5.2 First experimental evidences

In contrast to graphene, silicene does not exist in nature, so exfoliation methods cannot be used to generate single 2D layers from a graphite-like solid

phase. Different grow techniques, among those typically used in condensed matter physics, have to be considered for synthesizing silicene. A suitable choice is to deposit silicon by means of Molecular Beam Epitaxy (MBE) onto a non-reactive surface. Usually, metal surfaces are a good choice because they do not interact strongly with the incoming adatoms and do not form alloys for reasonably low temperatures. Ag surfaces have been used intensively in recent years to grow silicon nanostructures. In particular, Ag(001) and Ag(110) have been exploited to grow silicon stripes and highly oriented Si nanoribbons with silicene-like properties, respectively [10, 11]. However, in order to potentially grow a honeycomb lattice, a sixfold top layer symmetry surface is demanded. For this purpose, the Ag(111) surface results to be an excellent candidate to support the formation of silicene. A first attempt on this surface was claimed by Lalmi *et al.* based on Scanning Tunneling Microscopy (STM) observation of honeycomb silicene sheet [12]. However, the reported experimental data did not convince the scientific community which raised some doubts on the claimed result. The most critical point is about huge compression that silicene film seems to experience with a Si-Si distance of just 0.19 nm, which is rather unreasonable [13]. The first clear experimental evidence of silicene[1] on Ag(111) has been reported by Vogt and collaborators [14]. They combined Low-Energy Electron Diffraction (LEED), STM, and Angle-Resolved Photoelectron Spectroscopy (ARPES) measurements supporting the formation of honeycomb silicon sheet and confirming the structural and electronic properties predicted by theory. Similar structural results have been also reported by Lin *et al.* [15]. Evidences of silicene formation on $ZrB_2(0001)$ [16] and Ir(111) [17] have been also reported.

5.3 Morphological properties

To study the silicene structural properties several experiments have been carried out by properly tuning growth parameters. STM has been intensively used to scrutinize the as-grown topographies, thus providing atomic characterization. When dealing with MBE growth, a starting fundamental step is related to sample surface preparation. For this purpose, Ag(111) single crystal has been usually cleaned by several cycles of sputtering and annealing. Ar^+ ion sputtering at 1 keV kinetic energy and 10^{-6} mbar partial pressure has been performed for 30-60 min. Subsequent annealing at 530 °C for 30 min ensures a clean surface as shown in Fig. 5.1. In particular, the atomic resolution clearly evidences the six-fold symmetry with lattice parameter of 0.289 nm. Si deposition occurred by means of a dedicated evaporator after accurate degassing. Gaussian beam spot of about 15 mm confirms that most of the sample (13×5 mm^2) intercepts the silicon flux. Several evaporation fluxes have been used

[1] In contrast to the definition proposed by Guzman-Verri and Lew Yan Voon [4], it is nowadays common practice to name silicene even the puckered configurations, i.e. Si(111) monolayer, and not only the planar one.

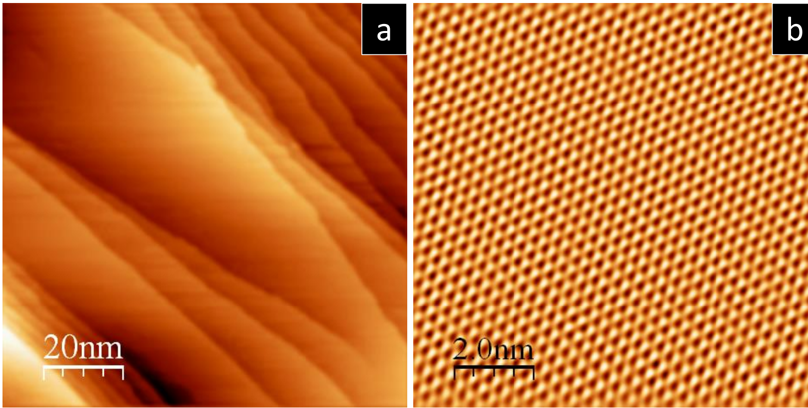

Figure 5.1: STM images of Ag(111) terraces $100 \times 100\ nm^2$ (a) and atomic resolution $10 \times 10\ nm^2$ (b). STM images were acquired at -0.2 V bias with an etched W tip and at tunneling current set point of 1.9 nA.

ranging from 1.1×10^{-2} to 6.4×10^{-2} ML/min estimated by means of quartz microbalance and X-ray Photoelectron Spectroscopy (XPS). Two main growth parameters have been firstly considered such as substrate temperature and coverage. The former is responsible of Si adatoms mobility, while the latter dictates their density. Keeping the substrate temperature constant at 250 °C and varying coverage (in the sub-monolayer regime) the following phase diagram is obtained. For coverage of 0.45 ML the surface morphology is dominated by the presence of 2D flat domains that cannot be atomically resolved by STM (Fig. 5.2a). It is possible to argue that *topographic effect* may take place since the more conductive Ag could be imaged as a protrusion with respect to the less conductive Si. This hypothesis is supported by the different tunneling conditions used before and after Si deposition. Typically, Ag surface is scrutinized in low tunneling resistance conditions, whereas on Si higher tunneling resistance is used. However, as will be discussed more in detail in Sec. 5.4, these flat domains are made up of Si because their electronic properties differ from those of Ag. Their atomic arrangement is at the moment not understood. When increasing nominal coverage to 0.65 ML, these 2D flat domains combine with other corrugated domains characterized by the presence of a regular pattern (Fig. 5.2b). Finally, for coverage of 0.9 ML the first kind of domains disappears and only rippled domains are present on the substrate (Fig. 5.2c). Hence, increasing nominal coverage, in the sub-monolayer regime, results in a progressively formation and enlargement of structured domains with a concomitantly suppression of flat domains. Similar experiments have been performed at lower substrate temperatures for equivalent coverage values. For $T < 240$ °C no structural transition from flat to structured domains is observed. Therefore, silicene formation on Ag(111) occurs only if an onset of temperature and coverage is reached. The structured domains show two main

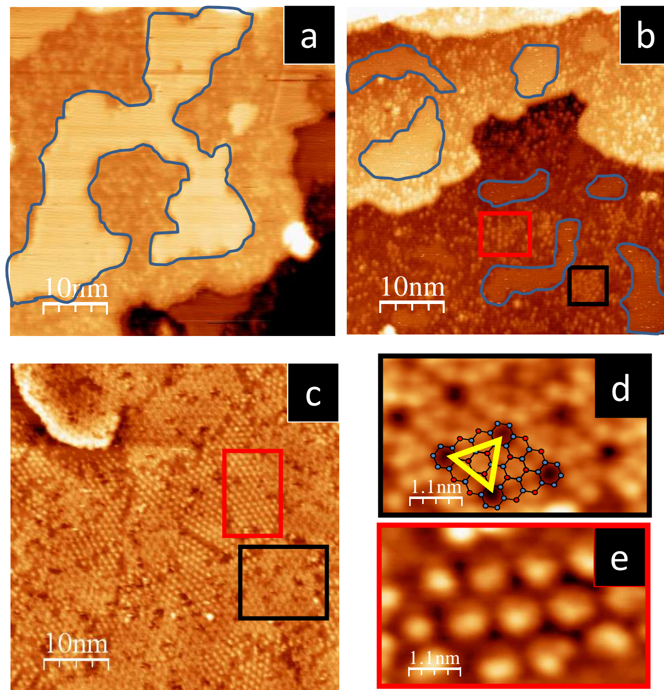

Figure 5.2: STM images of Si deposition with 0.45 ML (a), 0.65 ML (b), and 0.9 ML (c) nominal coverage. All images are 50 × 50 nm^2. STM magnification of black and red boxes depicted in (b) and (c) showing (4 × 4) superstructure (d) and hexagonally packed dots (e). STM images were acquired at -1.5 V and -1.3 V bias and at tunneling current set point of 0.1 – 0.4 nA.

characteristic arrangements: a (4 × 4) superstructure and periodic patterns of hexagonally packed dots (Fig. 5.2d and e). The STM detection of (4 × 4) symmetry with respect to the bare Ag(111)-(1 × 1) has been proven to be an indirect evidence of silicene [14, 15]. Vogt *et al.* demonstrated that formation of silicene is in good agreement with the 2D growth mode, since smaller 2D islands start to grow bigger with increasing deposition and eventually covering Ag terraces [14]. The characteristic flower-like shape of this reconstruction (see Fig. 5.2d) is the result of Si atoms displaced on different heights. Dark centres are separated by 1.14 nm corresponding to 4 times the Ag(111) surface lattice constant (0.289 nm) and 3 times the freestanding silicene lattice constant (0.383 nm [7]). Hence, the (4 × 4) Ag superstructure corresponds to a (3 × 3) silicene reconstruction. The notation with respect to the silver substrate will be considered throughout the present Chapter. Dark centres are surrounded by six triangular structures consisting of three bright protrusions separated by 0.4 nm. The voltage independence of STM imaging suggests that geometric rather than electronic effects dominate, as also confirmed by Atomic Force Microscopy (AFM) measurements [18]. The (4 × 4) superstructure STM image

can be explained by a 2D honeycomb silicene sheet, where Si atoms are placed either on top or in between of Ag atoms. However, only on top atoms are probed by STM, thus giving rise to the characteristic flower-like shape [14, 18]. By geometric considerations, it is possible to calculate an average Si-Si distance of 0.22 nm, which is in excellent agreement with predicted values reported in Sec. 5.1. Structural model based on Density Functional Theory (DFT) determined a Si-Si distance of 0.232 nm and top-bottom Si atoms separation of 0.075 nm [14], which indicates that (4×4) silicene on Ag(111) is LB. Moreover, this structural model gives also information on the hybridization state of single atoms. Six top Si atoms of (4×4) cell form bond angles of about 110°, very close to 109.5° of full sp^3 hybridization. From the twelve bottom Si atoms, six are purely sp^2 hybridized with angles of about 120° and the remaining six have bond angles between 112° to 118° [14]. Hence, in contrast to graphene which is flat and fully sp^2 hybridized, silicene has a buckled honeycomb atomic arrangement of mixed sp^2/sp^3 hybridized atoms.
The nature of hexagonally packed dots has been investigated more in detail. A comparative analysis is simplified by the simultaneous presence of different morphologies on the same sample and then in single STM images. Furthermore, benefiting of the concomitant presence of (4×4) superstructure, the alignments of various domains can be easily compared with $[1\bar{1}0]$ direction of Ag(111) surface. Indeed, the (4×4) superstructure is aligned along this high symmetry direction. Fig. 5.3a shows a STM image which satisfies the above mentioned requirements. In fact, besides the (4×4) superstructure in white contour, other adjacent patterns can be individuated. Three different patterns can be distinguished with periodicities of ∼0.8 nm (red contour in Fig. 5.3a) and ∼1 nm (blue and black contours in Fig. 5.3a). Since (4×4) superstructure has quite similar periodicity, i.e. 1.14 nm, the previous periodicities could be regarded as $\sqrt{7}$, $\sqrt{13}$, and $2\sqrt{3}$ times the Ag lattice constant. Their misalignment with respect to the Ag(111) $[1\bar{1}0]$ direction is ∼20° (for red contour), ∼13° (black contour), and ∼30° (blue contour). These resulting patterns can be interpreted as oriented silicene domains, differently overlapped on the underlying Ag(111). Depending on the relative orientation between the silicene honeycomb lattice and the Ag(111), different Si atoms are placed either on top or in between of Ag atoms. As a consequence, different buckled superstructures arrange in addition to the (4×4) superstructure, thus forming a compact patchwork quilt, similar to the case of graphene on Cu foils [19]. Therefore, the observed patterns can be respectively associated to $(\sqrt{7} \times \sqrt{7})$, $(\sqrt{13} \times \sqrt{13})$, and $(2\sqrt{3} \times 2\sqrt{3})$ superstructures. With the help of hard spheres models, it is possible to gain insights these different superstructures. Indeed, from STM images only, it is rather difficult to deduce an atomic model. For this purpose, simple hard spheres model representing the respective superstructures have been summarized in Fig. 5.3b, where Si atoms are in blue, Ag substrate is shown gray, and yellow contours simulate the corresponding expected STM topographies. Unit cells are also reported in red. $(\sqrt{7} \times \sqrt{7})$ superstructure is obtained rotating the

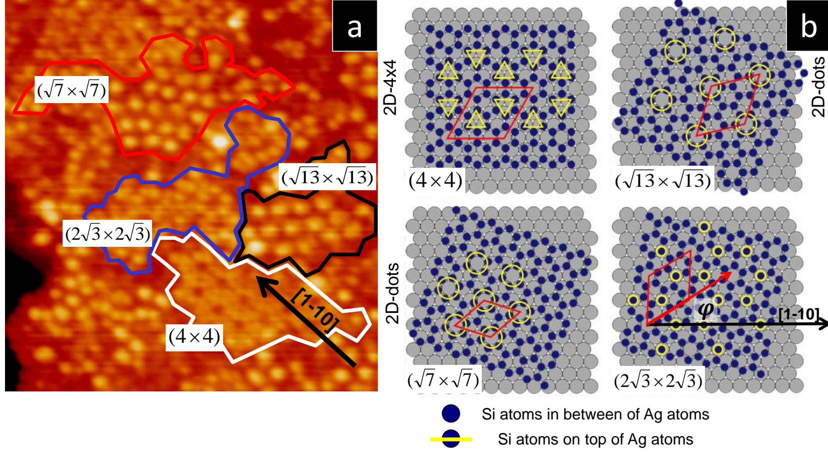

Figure 5.3: (a) STM image of multi-oriented silicene domains on Ag(111) and (b) hard spheres model of silicene superstructures (in blue) on Ag(111) (in grey) with yellow and red contours indicating the resulting STM topography and unit cells, respectively.

Si adlayer of 19.1° with respect to the $[1\bar{1}0]$ direction of Ag(111). Therefore the complete notation is $(\sqrt{7} \times \sqrt{7})R19.1°$. In this model all Si atoms are close to three-fold site [20], so the protrusions seen in the STM image can be associated to tip-convolution effect. $(\sqrt{13} \times \sqrt{13})$ superstructure can be interpreted as a silicene sheet rotated of 27° which means that superstructure periodicity is shown at angle of 13.9° with respect to the $[1\bar{1}0]$ direction of Ag(111). Six Si atoms are found on top of six Ag atoms surrounding a central Ag atom, thus giving rise to large protrusions observed by the STM image. Because this superstructure is not on a Ag symmetry axis, another kind of $(\sqrt{13} \times \sqrt{13})R13.9°$ exists where the silicene sheet is rotated of 5.2° instead of 27° [20, 21]. Different types of the same superstructure will be distinguished following the nomenclature introduced by Enriquez *et al.* [21]. For example, Fig. 5.3a shows $(\sqrt{13} \times \sqrt{13})$-I superstructure. Finally, when the silicene sheet is rotated of 10.9°, the resulting $(2\sqrt{3} \times 2\sqrt{3})R30°$ superstructure appears. These additional superstructures have different buckling values because different silicon atoms lie on top or in between of silver atoms, thus giving rise to different periodicities, thus making silicene a multi-phase material. Tab. 5.1 summarizes the calculated properties of the most important silicene superstructures discussed in the following. These structural phases stem from the intrinsic flexibility of silicene originated by its buckled structure, which acts as an additional degree of freedom, in contrast to graphene. In addition to these coexisting phases, another silicene single phase superstructure is present. Fig. 5.4a and b show two STM images of $(4/\sqrt{3} \times 4/\sqrt{3})$ superstructure obtained after annealing the as-grown morphology at 290 °C. This superstructure has been reported firstly by Feng *et al.* and it is the silicene superstructure which more closely resembles a honeycomb structure [22]. The same authors measured a peri-

Table 5.1: Number of atoms per supercell, Si-Si buckling distance, cell parameter, and Si-Si bond length of silicene superstructures. The buckling distance is measured from the top atoms to a bottom plane standing at the average height position of the bottom atoms.

Superstructure	Si atoms per cell (Top)	Buckling (Å)	Cell parameter (Å)	Si-Si distance (Å)
(4×4)	18 (6)	$0.71 < \Delta z < 0.77$	11.78	$2.34 < d < 2.39$
$(\sqrt{13} \times \sqrt{13})$	14 (4)	0.77	10.60	$2.31 < d < 2.36$
$(2\sqrt{3} \times 2\sqrt{3})$	14 (2)	1.1	10.20	$2.28 < d < 2.36$

odicity of 0.64 nm in contrast with the expected value of 0.67 nm [23]. Their experimental value is therefore about 4% smaller than the theoretical one. This contraction has been initially explained by a phenomenological configuration where Si atoms are pulled either upward or downward in a $AB\overline{A}$ configuration. However, subsequent low temperature STM measurements allowed Chen *et al.* to find out a spontaneous symmetry breaking of silicene layer at 77 K by forming two mirror symmetric rhombic superstructures [25]. These two superstructures have identical geometry when ignoring the substrate and share the same central substrate atom for each hexagon unit. Hence, the six Si atoms around the center of the hexagon will be flip-flopped so quickly that the STM observes the resulting honeycomb superstructure originated by the two rhombic phases [25]. Fig. 5.4a shows the room temperature STM image acquired at -1.2 V sample bias and 0.5 nA tunneling current, which closely resemble those reported in literature [22, 23, 25]. However, changing the polarity of sample bias from filled states to empty state imaging, it is possible to notice that the same honeycomb structure appears more evident with the possibility to resolve single atoms. The line profiles reported in Fig. 5.4c and d indicate that the imaged atoms are placed on top of silver ones according to the model proposed in the papers by Wu's group [22, 23, 25]. However, some discrepancies are present. Indeed, here, the measured periodicity is in excellent agreement with the theoretical one, i.e. 0.67 nm, thus suggesting that the silicene layer is not compressed. This is also confirmed by the Si-Si distances between on top Si atoms which is 0.4 nm in good agreement with the expected value of 0.38 nm. At the time of writing, a definite model of $(4/\sqrt{3} \times 4/\sqrt{3})$ structure is still lacking and it is not clear yet if this superstructure is a monolayer [22, 23, 25] or multilayer [18, 26, 27] silicene phase.

5.4 Electronic properties

As discussed in Chapt. 1, the effort to synthesize silicene is mainly devoted to exploit this material in future electronic devices. For this purpose, a clear picture of its electronic properties represents the main important topic. In their paper, Vogt *et al.*, along with a detailed analysis on the structural properties of

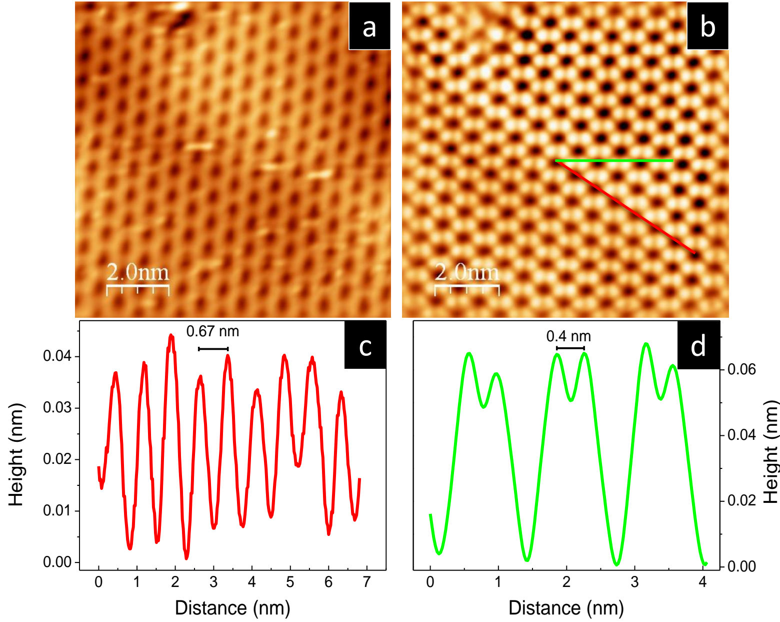

Figure 5.4: (a) STM image of $(4/\sqrt{3} \times 4/\sqrt{3})$ silicene superstructure acquired at -1.2 V sample bias and (b) the same image acquired at 1.2 V sample bias. (c) and (d) line profiles along the red and green lines of (b), respectively.

(4×4) silicene, showed ARPES data recorded at photon energy of 126 eV [14]. They found a linear dispersion in the electronic bandstructure in the Si K point of the Brillouin zone. The linear dispersion can be fitted by $E = \hbar v_F k$ with Fermi velocity $v_F = 1.3 \times 10^6$ m/s. Such a value of Fermi velocity is comparable to the one found in graphene [28]. However, in contrast to graphene, the conical branches do not cross the Fermi level but the apex of the Si cone is approximately 0.3 eV below Fermi level. Therefore, it is possible to assume that the gap opening between π and π^* amounts to about 0.6 eV [14, 29]. Nonetheless, the bandgap opening could result from the substrate interaction, as already observed for the case of graphene on SiC [30, 31]. Without using synchrotron radiation, it is possible to determine the local electronic properties by means of STM. The electronic properties of single silicene phases can be quite easily examined by using Scanning Tunneling Spectroscopy (STS), which guarantees a local probe of both valence and conduction bands around Fermi level. STS spectrum results in a proportional relationship with the local density of states (LDOS) (Chap. 2), thus providing a powerful tool to discern electronic properties up to the atomic scale. In particular, STS investigations have been performed on the various 2D morphologies observed, keeping (4×4) superstructure as reference. In Fig. 5.5 dI/dV tunneling spectra acquired on different Si domains are reported. First of all, Ag(111) (Fig. 5.5a) has been scrutinized with resulting spectrum which is typical of metal surfaces and in good agreement with results reported in

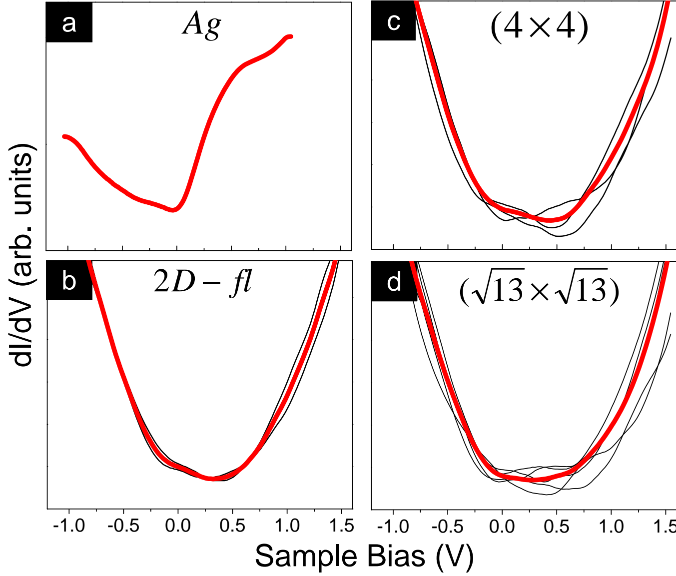

Figure 5.5: (a) STS spectra of clean Ag(111) surface; (b) 2D flat domains; (c) (4×4) and (d) $(\sqrt{13} \times \sqrt{13})$-I superstructure.

literature [32]. In order to compare electronic properties of substrate and Si adlayers, the initial STS characterization has been limited to 2D flat domains obtained at low coverage, $(\sqrt{13} \times \sqrt{13})$-I, and (4×4) superstructures. From Fig. 5.5, it is possible to recognize different profile in the STS spectrum of each Si adlayer with respect to the Ag(111). Indeed, a plateau-like feature, comprised between two lateral branches, can be identified while spanning the bias voltage between $-0.2\,\text{eV}$ to $0.6\,\text{eV}$. This aspect confirms that 2D flat domains are made up of silicon atoms and are not due to topographic effect (Sec. 5.3). Moreover, all the three Si domains show different electronic behavior with respect to the Ag. In Fig. 5.5c and d individual dI/dV spectra (black curves) of corrugated phases are affected by comparatively wider dispersion with respect to the average (red curve) than in the case of 2D flat domains (Fig. 5.5b). Since both corrugated phases show such a dispersion while flat phase does not, a possible role of buckling in determining electronic properties is expected. In order to verify that dispersion of STS spectra is not simply related to statistical fluctuations, a detailed analysis in the plateau-like region is reported in Fig. 5.6, where two distinct groups of curves can be recognized. Moreover, these STS spectra were obtained by probing different surface lattice sites. Green curves can be easily distinguished from the blue ones, since they show a symmetric behavior centred on the bias voltage $V_B = 0.25\,\text{eV}$ while, conversely, blue curves show an asymmetric behavior with two dips, i.e. local minima, placed at $V_B = -0.2\,\text{eV}$ (sample occupied states) and $V_B = 0.6\,\text{eV}$ (sample empty states). This bimodal distribution of STS curves suggests that their dispersive nature is

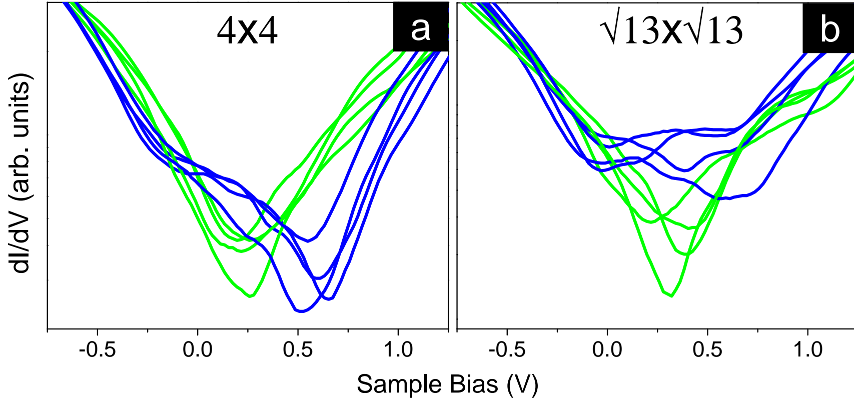

Figure 5.6: STS curves on (4×4) superstructure (a) and $(\sqrt{13} \times \sqrt{13})$-I superstructure (b).

unlikely related to statistical fluctuations but it is instead probably related to a position-dependent LDOS. Single STS curves reported in Fig. 5.5 are randomly acquired on the surface. However, a correspondence between the local surface morphology and the respective dI/dV spectrum is found. Green spectra have been acquired in the dark hole bottom position of (4×4) superstructure and on top of the protrusions generated by $(\sqrt{13} \times \sqrt{13})$-I superstructure (Fig. 5.7). On the contrary, blue curves are related to top bright triangular position in (4×4) superstructure and bottom position in $(\sqrt{13} \times \sqrt{13})$-I one (Fig. 5.7). Two possible interpretative hypotheses can be considered in order to explain the experimental scenario. The former consideration is that the origin in the charge inhomogeneity can be correlated with the characteristic surface modulation of silicene. Indeed, a similar effect results in rippled graphene on Ru substrates [33]. For graphene on Ru substrate, the inhomogeneity can be understood in terms of charge transfer from conduction to valence band as confirmed by both dI/dV spectra and tight-binding model incorporating a periodic potential. A space dependent interaction between silicene and Ag(111) surface might be responsible for local charge transfer or metal screening. Moreover, these local alterations could arise from the structural transition from flat to corrugated domains. The latter hypothesis is concerned with the symmetry breaking in the honeycomb lattice. In particular, the presence of topological defects which might be introduced by the off plane buckling could be responsible of modifications in the electronic structure. The presence of a buckled structure in silicene clearly requires particular attention when dealing with symmetry arguments. Indeed, the freestanding silicene structure has not been discovered yet. Hence, the superstructures found on metallic substrates are obviously different in terms of symmetry. For this purpose, in the following, a phenomenological model, which accounts for the buckling distortion, is proposed to explain the experimental data. As already discussed, the presence of a vertical buckling

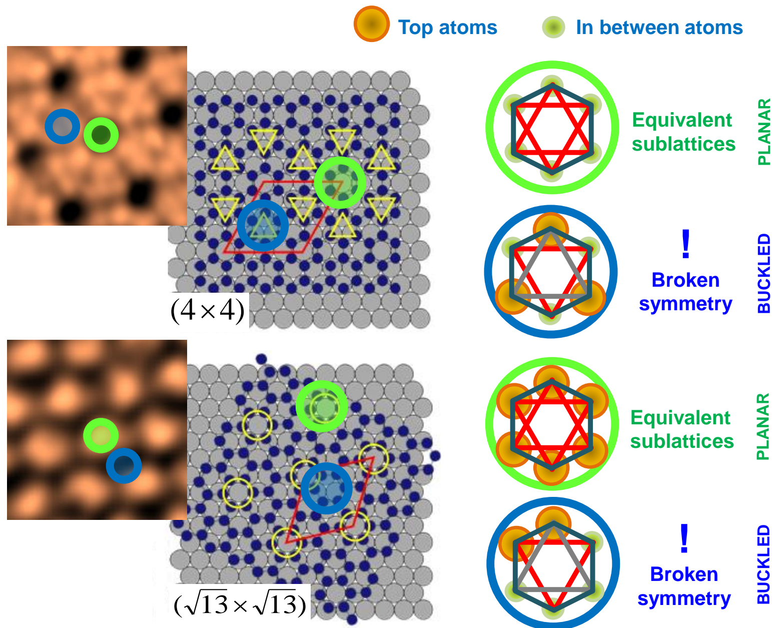

Figure 5.7: Hard spheres model of (4×4) superstructure (top panel) and $(\sqrt{13} \times \sqrt{13})$-I superstructure (bottom panel) indicating in blue and green circles the lattice position where the STS spectra of Fig. 5.6 have been acquired.

introduces a further degree of freedom that is not present in graphene. Graphene honeycomb structure is composed by two different triangular sublattices (see Chapt. 4), which give rise to most of its peculiar electronic properties [34]. Nonetheless, interface related interaction may provoke deviations from the freestanding configuration. For instance, epitaxial graphene on SiC experiences a substrate interaction, which is responsible for a small bandgap opening caused by sublattice symmetry breaking [30]. Fig. 5.7 depicts the hard spheres model of (4×4) (top panel) and $(\sqrt{13} \times \sqrt{13})$-I (bottom panel) superstructures. Si atoms are represented in dark blue spheres, Ag atoms in grey spheres, and yellow contours are a guide for the eye predicting resulting STM topography (shown in insets for both superstructures). Considering the case of (4×4) superstructure, it is possible to perceive that green curves are related to equivalent triangular sublattices, i.e. the six Si atoms lie on the same plane since they are all in between of Ag ones. Blue curves are instead associated with a position where symmetry breaking in the sublattices occurs. As a matter of fact, the gray triangle of blue spectrum in Fig. 5.7 (top panel) shows all atoms in the top position while the red triangle in the bottom position. The situation is reversed when considering $(\sqrt{13} \times \sqrt{13})$-I superstructure (Fig. 5.7 bottom panel). Green curves associated with protrusions correspond to equivalent sublattices where all the six Si atoms, which compose the hexagonal cell, are placed on top of an underlying Ag atom. Differently, blue curves are obtained when probing

a buckled cell where the six-fold symmetry is inevitably broken. This simple model may explain, by symmetry arguments, why families of STS spectra collected on different silicene phases behave similarly. While green spectra of both superstructures are related to a lattice position where hexagonal symmetry is conserved, blue spectra are instead associated with symmetry breaking due to the intrinsic buckled configuration of silicene. Therefore the LDOS of these silicene superstructures results to be periodically modulated by the symmetry breaking, whose origin can be found in the presence of intrinsic buckled bonding in the silicene sheet as a consequence of a modulated interaction with the Ag substrate. However, an estimation of such an interaction is not possible by STS only. Moreover, detection of Dirac point in STS curves is not a simple issue. In the present case, although dI/dV curves of Ag(111) and Si adlayers are different, a precise assignment of Dirac point energetic position should take into account the presence of a metallic substrate, i.e. a non-vanishing DOS and surface states near Fermi level. A clear assignment of Dirac point could be achieved by applying a gate voltage thus causing Dirac point to shift energetically relative to Fermi level, as demonstrated for graphene grown on SiO_2 [35], but, again, this option is at the moment impracticable. Another possibility consists in measure quasi-particle interference (QPI) patterns originated by scattering of free carriers. Constant energy contours in reciprocal space cut through the electron or hole conical sheets near Fermi level resulting in small circles centred at the K points. Carriers can be scattered within small circles (intra-valley scattering) or between circles (inter-valley scattering) giving rise to QPI patterns in real space STS maps, as demonstrated for graphene on SiC [36]. For what concerns silicene, Feng *et al.* found in $(4/\sqrt{3} \times 4/\sqrt{3})$ superstructure (which is $\sqrt{3} \times \sqrt{3}$ reconstruction with respect to the silicene lattice) Dirac point at $-0.5\,\text{eV}$ which deviates from Fermi level because of charge transfer from Ag(111) to silicene [22]. By means of QPI patterns the same group confirmed the energetic position of Dirac point and determined $v_F = 1.2 \times 10^6\,\text{m/s}$ in the $(4/\sqrt{3} \times 4/\sqrt{3})$ superstructure. Despite independent experiments performed by ARPES and STS measurements showed the presence of massless Dirac fermions in silicene superstructures grown on Ag(111), a clear picture of the electronic properties is, at the moment, elusive. In fact, there is no consensus on the aforementioned electronic properties. Arafune *et al.*, commented the QPI patterns pointing out that for low wave number the dispersion relation should be fitted by parabolic function, thus concluding that there are no massless Dirac fermions but quasi-free electrons arising from the surface states of Ag(111) modified by Si covering [24]. On the other hand, Chen *et al.* replied that measurements at 6 K are inevitably affected by structural transition which takes place at 77 K thus introducing further scattering centres that overshadow the original effect [23, 25]. These considerations are related to $(4/\sqrt{3} \times 4/\sqrt{3})$ superstructure which is not clear yet whether it is only a first layer, only a second or multi layers, or can be both of them [18, 26, 27, 37, 38]. However, (4×4) superstructure has been questioned too, since STS experiments

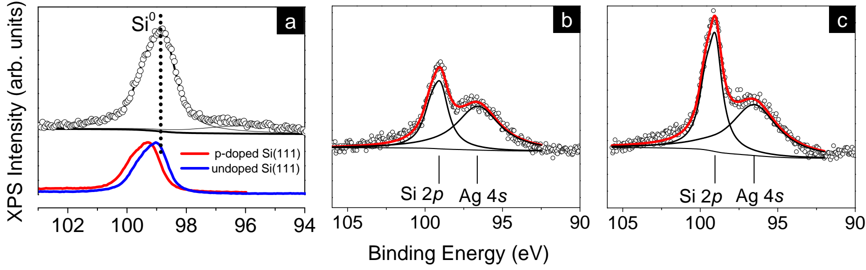

Figure 5.8: (a) Si 2*p* XPS line of silicene grown on Ag(111) (top panel) and of references substrates of p-doped (red line) and nominally undoped (blue line) Si(111). (b) and (c) Si 2*p* and Ag 4*s* core levels corresponding to Fig 5.2a and b, respectively.

in magnetic field showed the absence of Landau levels that represent a clear signature for the presence of massless Dirac fermions [39]. Nonetheless, further detailed ARPES experiments confirmed the results proposed by Vogt *et al.* unravelling the complicated bandstructure related to the (4×4) silicene on Ag(111) [29]. These conflicting results on the electronic properties of silicene phases confirm the complicated nature of this novel material which, anyway, represents an interesting candidate since, once completely understood, could pave the way to the possibility of artificially tuning electronic properties in 2D materials. Moreover, theoretical calculations on freestanding silicene show intrinsic values of electron mobility of $2.57 \times 10^5\,\mathrm{cm^2V^{-1}s^{-1}}$ and hole mobility of $2.22 \times 10^5\,\mathrm{cm^2V^{-1}s^{-1}}$ which are smaller than those of graphene but still very high and promising [40].

5.5 Chemical properties

Together with morphological and electronic aspects, the chemical properties of silicene should be carefully taken into account. Indeed, in contrast to graphene, silicene does not exist in nature, i.e. there is not solid phase of silicon similar to graphite, and therefore the chemical aspects related to bonding formation are relevant. Furthermore, silicene chemical functionalization is expected to provide a wide range of electronic properties [41] as, for example, indicated by hydrogenated silicene [42]. Experiments using synchrotron radiation to chemically characterize silicon adlayers on Ag(111) and $ZrB_2(0001)$ have been reported [14, 16, 29]. Indeed, a powerful tool to gain insights of chemical features is represented by PES (see Chapt. 2). High resolution synchrotron radiation evidences that in silicene nanoribbons Si 2*p* core level has the narrowest full width half medium ever found in the Si solid phase [11]. For silicene on Ag(111), this value is comparable [29]. Fig. 5.8 shows Si 2*p* line related to elemental silicene which is peaked at binding energy of 98.8 eV and can be well distinguished from the Ag 4*s* line from the substrate. Fit to the XPS lines involved Shirley background removal and decomposition in pseudo Voigt

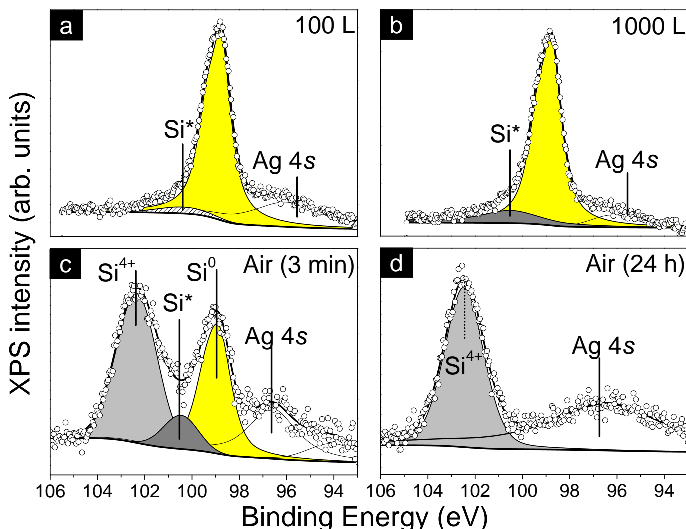

Figure 5.9: (a) Si $2p$ XPS line of silicene after 100 L O_2 exposure, (b) after 1000 L O_2 exposure, (c) after 3 min dry air exposure, and (d) after one day in air.

functions (products of Gaussian and Lorentzian). Doublets of Voigt functions were adopted when treating p core levels. This binding energy position is shifted to slightly lower energy with respect to the reported Si $2p$ lines of p-doped and nominally undoped Si(111) substrates (Fig. 5.8a). This shift can be attributed either to an n-type character of silicene, intrinsic of deposition process, or to an electron transfer from Ag. This latter hypothesis is well-known to occur in graphene on metal substrates [33]. Despite buckling can be related to the intrinsic nature of the Si adlayer, no substrate induced change in the chemical bonding state of the silicene layer, e.g. Si-Ag bonding, can be deduced from the deconvolution of Si $2p$ line, thus suggesting marginal chemical interaction between Si and Ag atoms. Of course, for similar arguments, the possible formation of an alloy can be ruled out at the temperature range here explored. XPS spectra depicted in Fig. 5.8b and c represent the thickness dependence of Si $2p$ core level in function of coverage. The reported spectra correspond to the coverage regimes reported in Fig. 5.2. Therefore the intensity of Si $2p$ core level can be used combined with STM either to determine surface coverage or calibrate the deposition evaporator.

The chemical stability of silicene has been tested by O_2 exposure in Ultra-High Vacuum environment and upon exposure to ambient conditions. O_2 constitutes a significant choice because is the principal element of oxides which, in an applicative and device-oriented view, could represent a potential interface with silicene. The Si $2p$ lines of silicene exposed to 100 and 1000 L (1 L = 1 s at 10^{-6} Torr) of ultra-pure O_2 are reported in Fig 5.9a and b, respectively. The shape profile of Si $2p$ line exhibits a small asymmetry, which increases with exposure and can be associated to a minor Si-O component with a chemical

shift of 1.5 eV from the elemental silicene line. The scarce oxidation degree is consistent with the reported low reactivity of silicene nanoribbons [11] and can be tentatively related to oxidation pathways through structural defects or domain boundaries of silicene domains. A marked change affects the silicene composition already after 3 min exposure to dry air (Fig. 5.9c). The originally double-peak shape profile of Si 2*p* core level is now decomposed in three contributions, coming from the elemental residual silicene (Si^0) and two different kinds of Si-O bonding components (Si^* and Si^{4+}). The major Si-O bonding component is placed at binding energy of 102.3 eV and is consistent with a preferential SiO_2 formation originated by Si^{4+} state. The other component (Si^*) comes from lower valence states of Si-O bonding, i.e. sub-oxides species. Although no more dominant, it worth noting that silicene related line still persists on the surface even after 3 min long exposure to dry air. Nonetheless, longer exposure, e.g. one day, to air leads to complete oxidation of Si adlayer thus resulting in an atomically thin SiO_2 film (Fig. 5.9d). Oxidation of silicene in ambient condition represents a serious drawback for any silicene-based device functionalization as well as for a broad range of *ex situ* probing.

5.6 Silicene encapsulation

The previous reported results (Sec. 5.5) about chemical instability of silicene in ambient air conditions, in contrast to graphene which is chemically non-reactive, require a suitable strategy for exploitation of this material. While disentangling silicene from a metal template is still an open challenge, seeking for an on top interface engineering could let to achieve a two-fold objective. Indeed, interfacing silicene with a gate dielectric material could be benefiting for both any feasible voltage bias application and also for saving it from possibly destructive reactivity under ambient conditions. For this purpose, encapsulation of the silicene layer is a mandatory task. Capping, at room temperature, with an ultra-thin Al layer emerges as a promising option as the silicene bandstructure is not significantly altered by Al absorption according to theoretical predictions [43]. To this purpose, the silicene layer has been protected with a 7 nm-thick Al film. To assess, the Al-induced structural modifications in the Si adlayer, the Al growth has been monitored in real time by Reflection of High-Energy (30 keV) Electron Diffraction (RHEED). RHEED patterns of the relevant growth steps are reported in Fig. 5.10. Surface superstructures of the silicene domains can be deduced from the non-equivalently spaced sub-streaks of the RHEED patterns in Fig.5.10b which account for the interplay of different but quite similar periodicities of silicene superlattices and clearly distinguish the diffraction signatures of silicene domains from the characteristic pattern of Ag(111)-(1×1) surface (Fig. 5.10a). Despite the deposition is performed at room temperature, Al growth is epitaxial and flat since well-defined RHEED pattern can be observed during the Al deposition and no spotty pattern takes place. Silicene-related sub-

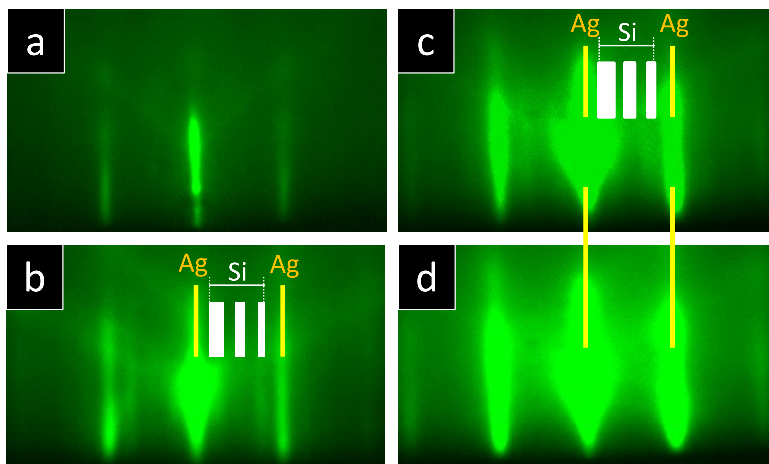

Figure 5.10: (a) RHEED pattern of clean Ag(111)-(1 × 1) surface; (b) silicene epitaxially grown on Ag(111), where the main streaks indicate the periodicity of the coincidence cell and sub-streaks are related to the various silicene superstructures. The different width of sub-streaks is intended to picture the interplay of different diffraction features; (c) 3 nm-thick Al film on silicene/Ag, and (d) 7 nm-thick Al film on silicene/Ag.

streaks can be still recognized after RHEED monitoring up to 3 nm-thick Al film, therein unambiguously indicating the persistence of the silicene arrangement. Since the RHEED sub-streaks of extra surface periodicity are usually vanishing in conventionally reconstructed semiconductor surfaces after foreign atoms adsorption, the persistence of silicene sub-streaks is indicative of the wetting character of the Al layer. Finally, when increasing thickness, Al-related streaks appear and place nearly in correspondence of the pristine Ag(111) streaks due to the similar unit cell of the Al(111) and Ag(111) surfaces. XPS probing of Al and Si core levels allows to gain insight into the compositional depth profiling of the Al/silicene/Ag(111) heterostructure in thickness range compatible with the photoelectron mean free path. To assess the chemical properties of the interface, the Si 2p and Al 2p core levels have been monitored with a variable take-off angle ranging from 37° to 70° with respect to the sample surface plane. No changes are observed in the Si 2p lines recorded at 1 nm and 4 nm-thick Al layer with respect to the reference taken on freshly as-grown silicene. In Fig. 5.11a, a shift of the Si 2p line to lower binding energy can be deduced after Al deposition and can be related to an extra charge exchange between Al and Si orbitals as much as previously observed in the freshly deposited silicene on Ag. Indeed, Al atoms, due to their low electronegativity comparable to that of Si atoms, are expected to lose electrons, i.e. behave like donors for silicene, in favor of the neighboring Si atoms. The so induced depopulation of bonding orbitals increases the length of the Si-Al bond thus weakening it [43]. An additional feature (see arrow in Fig. 5.11b) can be noticed at binding energy of 103.5 eV which is Al-related because the same feature appears even when Al is

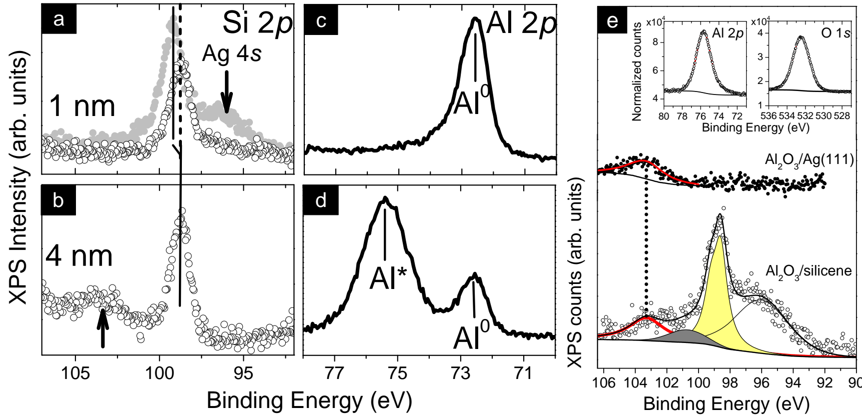

Figure 5.11: (a) Si $2p$ XPS line of silicene of freshly as-grown (dark gray) and after 1 nm of Al deposition; (b) after 4 nm of Al capping layer; (c) Al $2p$ line after 4 nm of Al capping layer showing elemental Al-Al bonding (Al^0), and (d) after oxidation of 7 nm-thick capping layer where Al* is indicative of Al_2O_3 formation. (e) XPS spectra of Si $2p$ and Ag $4s$ core levels of Al_2O_3/Ag(111) reference (top panel) and Al_2O_3/silicene/Ag(111) (bottom panel). Insets: Al $2p$ and O $1s$ lines with normalized intensity according to the respective atomic sensitivity factors.

directly deposited on Ag(111) without silicene interlayer. Al $2p$ line is indicative of a purely elemental Al bonding in the capping layer after 1 nm coverage thus ruling out the Si-Al bonding formation (Fig. 5.11c). Upon exposure of a 7 nm-thick Al-capped silicene to air (Fig. 5.11d), the Al $2p$ core level exhibits two component: one (Al^0) is related to residual Al-Al bonding at the bottom of the capping layer and another one (Al^*) is related to partial oxidation from the surface level. The chemical shift of the Al* component amounts to 2.9 eV which corresponds to a major Al_2O_3 composition [44]. Survival of a pure Al layer below the oxide can thus prevent the encapsulated silicene from any possible oxidation. The so obtained Al_2O_3 film shows very low roughness of 0.33 nm measured by *ex situ* AFM (data not shown) thus indicating a quite conformal morphology of the Al_2O_3/Al/silicene/Ag(111) heterostructure. While this configuration can be exploited to access *ex situ* characterization, engineering an Al_2O_3/silicene/Ag(111) heterostructure would be highly desiderable for the device-oriented point of view. In particular, the interface between Al_2O_3 and silicene could be regarded as potential interface between gate dielectric and active channel in a classical MOSFET architecture. Taking benefit from the previously observed low reactivity of silicene with dosed O_2, co-deposition of Al and O has been performed in order to induce Al_2O_3 formation. To this scope, Al growth rate has been adequately rescaled down to 0.1 Å/min and the oxygen partial pressure has kept at $\sim 1.3 \times 10^{-6}$ mbar (same used for 100 and 1000 L exposure) in order to promote the growth of a stoichiometric Al_2O_3 and avoid excess of elemental Al. Fig. 5.11e depicts the XPS spectra

acquired after sesquioxide Al_2O_3 growth. The Si $2p$ core levels is deconvoluted in three components (beside the Ag $4s$), namely the Si^0 line indicative of silicene bonding and two extra-components at 101.6 eV (Si^*) and 103.3 eV. This latter component can be assigned to Al-related component as demonstrated by the upper spectrum without silicene (top panel in Fig. 5.11e) and, therefore, can not be assigned to Si^{4+} bonding state. While O_2 preferentially reacts with Al (insets of Fig. 5.11e), the Si^* component can be interpreted as a limited oxidation of silicene layer in a sub-stoichiometric state. However, the Si $2p$ line is mainly dominated by Si^0 bonding, thus proving the nearly complete survival of silicene layer after Al_2O_3 formation. Similarly to the case of only pure Al capping layer, the Si $2p$ is down-shifted from its pristine binding energy position. This is consistent either with a charge transfer between silicene and oxide or with an oxide-induced modification of silicene electronic states. For what concerns the Al $2p$ line, reactive deposition of Al and O_2 results in the oxidation of Al with dominant Al^{3+} state placed at 75.6 eV in Al $2p$ line and in a O $1s$ line at 532.5 eV, both being consistent with Al_2O_3 constitution [44]. Moreover, the ratio of XPS areas deduced by pseudo Voigt fitting normalized on the relevant atomic sensitivity factors ensures the presence of sesquioxide stoichiometry, since Al and O atomic concentration are 35% and 65%, respectively. The asymmetric shape of Al $2p$ line can be understood considering lower Al oxidation states in a dramatically minor extent. Summarizing, two distinct non-destructive methodologies to encapsulate silicene layer in Al_2O_3/Al/silicene/Ag(111) and Al_2O_3/silicene/Ag(111) heterostructures can be fabricated without impacting on the structural and chemical properties of silicene itself. While the former configuration is intended to access *ex situ* diagnostic, the latter is potentially suitable to gated device implementations. These encapsulation designs can be generally applied to any silicene configuration regardless of the choice of substrate.

5.7 Raman spectroscopy characterization

The previous described encapsulation process allows to access *ex situ* characterization, in particular Raman spectroscopy. Raman spectroscopy is a powerful tool to investigate the arrangement of Si bonds in the silicene superstructures and how they influence vibrational and electronic properties (see Chapt. 2). In particular, Raman spectroscopy might elucidate the multi-phase character of silicene due to the variety of reconstructed Si domains found on Ag(111) surface. Three main important silicene superstructures, namely (4×4), $(\sqrt{13} \times \sqrt{13})$, and $(2\sqrt{3} \times 2\sqrt{3})$, show bond length dispersion in a range quite close to the Si-Si bond length in sp^3 diamond-like silicon (2.34 Å) (see Tab. 5.1). Bond angles result also distributed in a bimodal fashion with two peaks centred around 109° and 120°, which identify sp^3 and sp^2 hybridized atoms, respectively. As previously reported, the present case is strictly connected with the presence of

Ag(111) substrate, i.e. the aforementioned superstructures and their particular arrangement are related to the specific Ag surface. Therefore, the following aspects should be carefully taken into account. Substrate induces: a non-uniformly distributed vertical alignment of Si atoms, in contrast to freestanding silicene; a horizontal in plane strain being tensile in character and a partial hybridization between Si and Ag orbitals, whose strength is still unclear. These features are expected to dramatically impact the vibrational properties of each silicene superstructure.

In the following two distinct silicene configurations will be examined. The first one is shown in Fig. 5.12a, therein evidencing silicene domains presenting a lateral size of about 20-50 nm and uniformly distributed on the Ag(111) surface. The atomically resolved STM magnification in Fig. 5.12b shows that Si atoms are sequentially placed either in between or on top of the Ag atoms, thus generating two characteristic surface patterns, the (4×4) (green contour in Fig. 5.12b) and $(\sqrt{13} \times \sqrt{13})$-II (red contour in Fig. 5.12b) buckled superstructures. The second configuration is reported in Fig. 5.12c, where it is possible to observe the large scale topography of the $(2\sqrt{3} \times 2\sqrt{3})$ superstructure. $(2\sqrt{3} \times 2\sqrt{3})$ domains extend over the Ag(111) terraces, thus indicating an improved continuity of the layer with respect to the more fragmented surface structure depicted in Fig. 5.12a. The atomic-scale topography in Fig. 5.12d shows the characteristic surface pattern of this superstructure. The second configuration is obtained at slightly higher growth temperature (270 °C) than the first one. After carefully STM identification, these different configurations have been encapsulated following the procedure described in Sect. 5.6. In Fig. 5.13 the visible Raman spectra of Al_2O_3-capped silicene on Ag(111), Al_2O_3 film on Ag(111), and of air-exposed silicene on Ag(111) are compared. Firstly, it is worth noting that two broad feature around 300 and 800 cm^{-1} are present in the spectra of both capped silicene and Al_2O_3 only. These broad bands can be then assigned to the amorphous Al_2O_3 thin capping film [45]. As can be noted in the spectrum of non-capped silicene, the band at 800 cm^{-1} is still present but it is very weak. From the aforementioned air exposure experiments, when the Si/Ag(111) system is exposed to air, it reacts with atmospheric oxygen producing amorphous SiO_2. Therefore, the weak feature at 800 cm^{-1} in the reported spectrum can be assigned to a SiO_2 thin film [46], resulting from the partial oxidation of the silicene layer in agreement with the XPS measurements. However, visible Raman spectra of encapsulated silicene is mainly dominated by an intense and sharp feature located at 516 cm^{-1}, plus a broad and weak shoulder covering the 440 – 500 cm^{-1} spectral range. As no similar feature is observed in case of oxidized silicene or for the reference Al_2O_3/Ag sample, the origin of the narrow and asymmetric peak must be necessarily attributed to the intercalated silicene layer. Another component lying in the 930 – 1000 cm^{-1} spectral range is evident in the capped silicene spectrum; this feature is probably related to second order Raman features. Since bulk Si presents main peak at 521 cm^{-1}, deviation from this value can be interpreted either as strained Si or with presence of Si

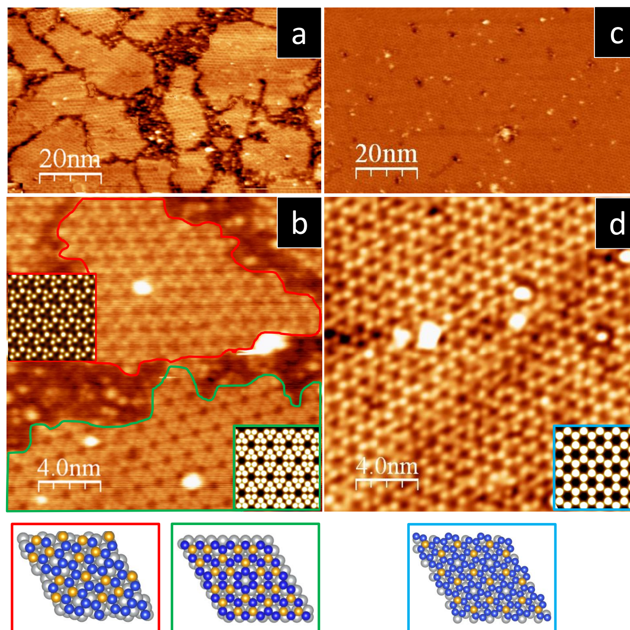

Figure 5.12: (a) Large-scale STM characterization of silicene domains on Ag(111) in the first configuration. (b) The two most abundant superstructures (4×4) (in green) and $(\sqrt{13} \times \sqrt{13})$-II (in red) with respective DFT relaxed superstructures and the corresponding simulated STM images shown as inset of panel (b). (c) Large-scale STM characterization and (d) atomic scale topography of the $(2\sqrt{3} \times 2\sqrt{3})$ superstructure with DFT relaxed superstructure and the corresponding simulated STM image shown as inset of panel (d). STM images were acquired at -1.4 V and 0.4 nA set point. Gray spheres denote Ag(111) atoms, whereas blue and orange indicate down- and up-standing silicene atoms, respectively.

nanocrystals. However, in the present case, this feature cannot be provided by a full sp^3 nanocrystalline silicon, because only ~ 2 nm tailed nanocrystals would induce the observed redshift whereas the STM probed domains turn out to have a width ranging from 20 to 50 nm [47, 48] (see STM image in Fig. 5.12a). A derivation of the peak at 516 cm^{-1} from a fully sp^3 stressed Si can be also ruled out because the periodicity of the Si lattice (0.54 nm) is much larger than the Ag(111) surface cell parameter (0.29 nm). As a consequence, the resulting compressive strain should up-shift Raman peak of bulk silicon at 520 cm^{-1}, thus not being consistent with the observed feature. Fig. 5.14 depicts the simulated spectra of the corresponding defect-free models, while Fig. 5.15 shows the experimental Raman spectra of co-existing (4×4) and $(\sqrt{13} \times \sqrt{13})$-II superstructures and $(2\sqrt{3} \times 2\sqrt{3})$ single phase. Fig. 5.15a shows the intense sharp peak at 516 cm^{-1} in the first configuration shown in Fig. 5.12a. Despite the sp^2/sp^3 nature of the two phases, a doubly degenerate E_{2g} mode is predicted to take place at 495 cm^{-1} and 505 cm^{-1} for (4×4) and $(\sqrt{13} \times \sqrt{13})$-II superstructures, respectively. These frequencies are in pretty good agreement with

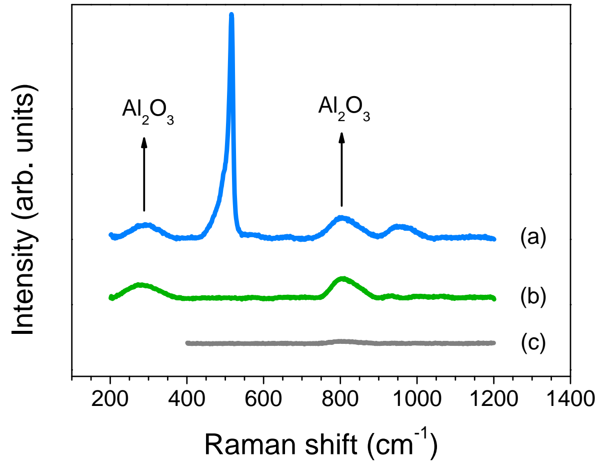

Figure 5.13: (a) Visible (488 nm) Raman spectrum of Al_2O_3-capped silicene, (b) 7 nm-thick Al_2O_3 reference film, and (c) uncapped silicene after air exposure. Spectra are vertically stacked for clarity.

the experimental feature at 516 cm^{-1}, taking into account an underestimation of about 1-5% for vibrational frequencies typical of implemented computation. As for the graphene G peak, this mode is provided by the bond stretching of all sp^2 silicon atom pair, thus reflecting the sp^2 character and being the fingerprint of a honeycomb lattice. Although the presence of E_{2g} modes clearly indicates the honeycomb nature of the 2D Si lattice, the broad and asymmetric shoulder in the $440 - 500$ cm^{-1} is not compatible with a defect-free planar trigonal geometry. In order to better understand the differences between silicene and graphene, it is useful to report some Raman features about graphene, which is well-studied [49]. Raman spectrum of graphene is characterized by the presence of a E_{2g} mode (G peak at 1581 cm^{-1}) and by 2D peak at 2600 cm^{-1} activated by inter-valley electron-phonon scattering between K and K' point of the first Brillouin zone. For graphene, the presence of an additional D(A_{1g}) peak at ~1300 cm^{-1} is expected when double resonance processes take place, namely intra-valley electron-defect scattering at K in the first Brillouin zone. The picture about silicene is however more complicated. Nonetheless assuming a defect-free model, it is quite surprisingly to find out several vibrational modes (denoted as D, T, and K in Fig. 5.14) with non-vanishing Raman intensity in the silicene superstructures. Beyond the E_{2g} vibrational mode, for the (4×4) case, two A_{1g} modes at 436 cm^{-1} and at 466 cm^{-1} (reported as D and T respectively in Fig. 5.14a) are Raman-active and the D one is the dominant feature. Similarly, the $(\sqrt{13} \times \sqrt{13})$-II superstructure presents, beyond the E_{2g} vibrational mode, a D(A_{1g}) peak at 455 cm^{-1} and a K(B_{2u}) peak at 475 cm^{-1}, as reported in Fig. 5.14b. By comparing the simulated spectra reported in Fig. 5.14, it can be noticed that the A_{1g} mode at 436 cm^{-1} is the most intense Raman-active mode in case of the (4×4) superstructure, while the E_{2g} mode becomes largely

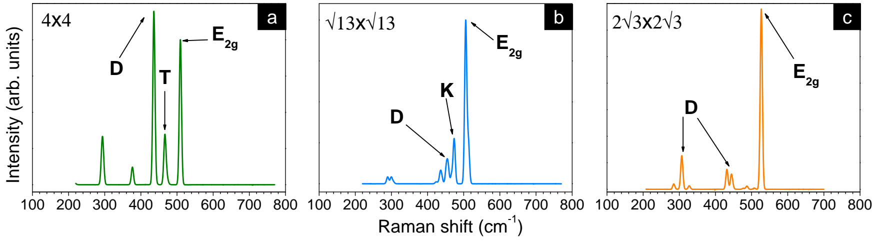

Figure 5.14: (a) Computed Raman spectra of the (4×4), (b) $(\sqrt{13} \times \sqrt{13})$-II, and (c) $(2\sqrt{3} \times 2\sqrt{3})$ superstructures obtained by the calculated vibrational spectra convoluted with a uniform Gaussian broadening having a full width at half-maximum of $10\,\text{cm}^{-1}$.

dominant for the $(\sqrt{13} \times \sqrt{13})$-II one. Since these two superstructures mutually differ in terms of their intimate buckling distribution, the observed intensity variation of the Raman features is reasonably related to their different atomic configuration. In particular, a flatter condition, i.e. a reduced number of buckled bonds, as in the $(\sqrt{13} \times \sqrt{13})$-II, results in a strong suppression of the A_{1g} modes intensity with respect to the E_{2g} peak. The origin of the A_{1g} mode activation can be then associated to an intrinsic "disorder" related to the non-uniform substrate-induced buckling and to the mixed sp^2/sp^3 nature of the honeycomb Si lattice. More in details, for the (4×4) case, the D(A_{1g}) mode comes from the breathing-like displacement of planar hexagons, while the T(A_{1g}) is related to the breathing-like displacement of non-planar hexagons; for the $(\sqrt{13} \times \sqrt{13})$-II, the D($A_{1g}$) and K($B_{2u}$) modes arise from the breathing mode of the hexagonal rings having alternating up- and down-standing atoms and to Kekule-distorted hexagonal rings, respectively [50]. Since the experimental Raman spectrum integrates the contribute of the two phases weighted by their abundances ratio, the Raman spectrum of 2D sp^2/sp^3 Si superstructures is dominated by the E_{2g} modes of the two superstructures, along with the asymmetric shoulder provided by the interplay of the disorder-activated modes (A_{1g} and B_{2u}). Remarkably, the experimental spectrum in Fig. 5.15a is well reproduced by the calculated spectrum of the $(\sqrt{13} \times \sqrt{13})$-II superstructure, rather than by the one of the (4×4) superstructure. This asymmetry may come from the smaller amount of (4×4) superstructure domains with respect to the $(\sqrt{13} \times \sqrt{13})$-II ones. Nonetheless, it is interesting to explore whether a Raman resonance not implemented in the adopted DFT framework might take place also in consideration of the measured bandgap for the (4×4) superstructure [14]. In this case, resonance effects are expected to selectively amplify the E_{2g} Raman-active modes. Indeed, the latter is an intra-valley phonon scattering process at Γ and thus, its resonance is strictly related to electronic transitions when the incident radiation is properly tuned with the direct bandgap transition, with the consequent enhancement of the related Raman signal. To probe possible resonant behaviors, the Raman spectrum of the two configurations has been investigated as a function of the excitation

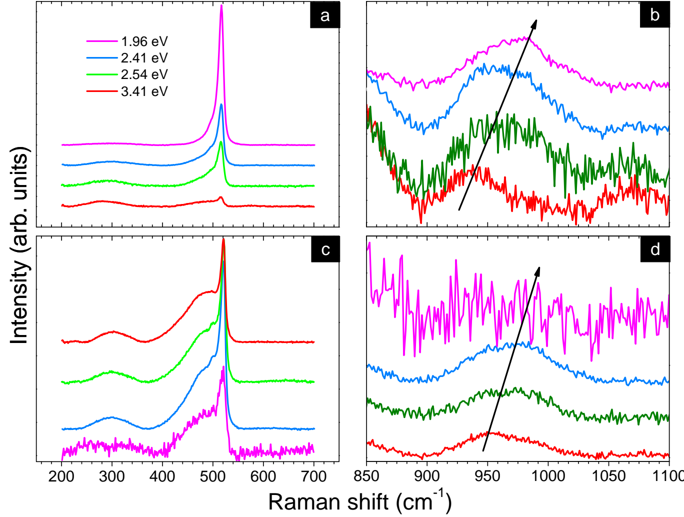

Figure 5.15: (a) Experimental Raman spectra of Al_2O_3-capped multi-phase sample $(4 \times 4)/(\sqrt{13} \times \sqrt{13})$-II and (c) isolated $(2\sqrt{3} \times 2\sqrt{3})$ superstructure acquired with different excitation energies. Magnification in the 850-1100 cm^{-1} spectral range of the Raman spectra of the (b) multi-phase sample $(4 \times 4)/(\sqrt{13} \times \sqrt{13})$-II and (d) isolated $(2\sqrt{3} \times 2\sqrt{3})$ superstructure acquired with different excitation energies. Spectra are vertically stacked for clarity.

energy. The case of the mixed $(4 \times 4)/(\sqrt{13} \times \sqrt{13})$-II phases is reported in Fig. 5.15a. The pronounced enhancement of the E_{2g} peak intensity with increasing excitation energy indicates a semiconductive character (formally similar to that of sp^3 silicon [51]), which is consistent with the reported presence of a direct gap in the (4×4) superstructure [14]. Interestingly, an additional indication of the multi-phase character of the sample comes from the frequency dispersion of the band at $\sim$900 cm^{-1} (see Fig. 5.15b): the observed blueshift as a function of the excitation energy is similar to that observed for the 2D peak of graphene, which is provided by the presence of the Kohn anomaly in the K point of the Brillouin zone [49]. The second order Raman feature of bulk Si is also located between 900 and 1000 cm^{-1}, which is suggestive of two transverse optical modes. When varying the exciting frequency, this band is affected by a change of the peak's intensity ratio because of Raman resonance rather than frequency dispersion [51]. The resonance behavior and the frequency dispersion can be rationalized by attributing a semiconducting character to the (4×4) superstructure consistently with ARPES outcomes [14, 29] and a graphene-like character to the $(\sqrt{13} \times \sqrt{13})$-II one. In contrast to these two superstructures, the $(2\sqrt{3} \times 2\sqrt{3})$ phase has been successfully stabilized as dominant phase after carefully tailoring the growth conditions. Fig 5.15c shows the experimental Raman spectrum of the $(2\sqrt{3} \times 2\sqrt{3})$, acquired with four excitation energies, while Fig. 5.14c the calculated one. As for the $(\sqrt{13} \times \sqrt{13})$-II superstructure,

the Raman spectrum is characterized by the presence of a strong E_{2g} mode at 521 cm^{-1}, confirming both the sp^2 hexagonal lattice symmetry and the sp^3-like nature of its bonds lengths. Furthermore, weak A_{1g} modes are also active, thus indicating a lower amount of intrinsic disorder with respect to the previously analysed superstructures. Interestingly, the ultra-violet Raman spectrum exhibits a quite low signal/noise ratio (Fig. 5.15d), thus reflecting a very low cross section at this frequency, that is opposed to the expected behavior of the sp^3 diamond-like silicon [51]. By observing the spectra reported in Fig. 5.15c and d, two remarkable facts must be underlined: no Raman resonance affects the E_{2g} mode and a frequency dispersion characterizes the ~900 cm^{-1} band. Both observations are not compatible with a full semiconductive sp^3 structure [51], but they rather reflect the presence of a Si honeycomb lattice with a characteristic graphene-like behavior, that is a non-resonant behavior and Kohn anomaly related frequency dispersion. It is then possible to describe the Si on Ag(111) 2D systems in terms of a sp^2/sp^3 form of silicon characterized by a vertically distorted honeycomb lattice provided by the substrate's constraints. For the first configuration, where two different superstructures coexist, i.e. (4×4) and $(\sqrt{13} \times \sqrt{13})$-II, the dependence of the Raman response with the excitation energy allows to recognize a non-trivial semiconducting character. On the other hand, in the configuration mostly dominated by the $(2\sqrt{3} \times 2\sqrt{3})$ superstructure, it is possible to recognize evidence of a low-distorted honeycomb lattice with a graphene-like symmetry and electronic character.

5.8 Conclusions and perspectives

In recent years a considerable effort has been devoted to identifying the graphene-like allotrope of silicon, namely silicene, both from the experimental and theoretical points of view. Although freestanding silicene has been hypothesized as a pure sp^2 hybridization of silicon, its existence under ambient conditions has been argued due to strong electron correlation in Si-based nanostructures. On the other hand, many authors succeeded in epitaxially growing a 2D Si layers on metallic substrates. In particular, silicene grown on Ag(111) is characterized by the presence of several phases showing different structural and electronic properties. These structural phases stem from the intrinsic flexibility of silicene in constrast to graphene. STM allows to observe a thermally activated process which induces surface phase transitions of single layer silicon domains from a flat morphology to complex 2D structures which are related to the formation of silicene domains. The latter domains show different preferential orientations that generate characteristic surface superstructures depending on the location of the silicene buckled bonds. It is also possible to find out a growth procedure promoting the coexistence of a variety of silicene phases. In this case the corresponding different silicene domains intersect together preserving their characteristic orientation and surface morphologies.

A position-dependent LDOS results from atomically resolved STS spectra of the (4×4) and $(\sqrt{13} \times \sqrt{13})$-I superstructures. Indeed, phenomenological considerations on symmetry breaking due to triangular sublattices inequality are proposed that qualitatively rationalize the observed position-dependent LDOS. Two distinct STS curves show similar behavior even if acquired in diametrically different position in the (4×4) and $(\sqrt{13} \times \sqrt{13})$-I superstructures because of buckling-induced distortion in the honeycomb lattice. Based on XPS monitoring of the Si $2p$ photoemission line, epitaxial silicene grown on Ag(111) proves to be chemically stable upon O_2 exposure up to 1000 L but it undergoes a progressive oxidation in air. A non-destructive methodology to encapsulate the silicene layer in physically Al_2O_3/Al/silicene/Ag and Al_2O_3/silicene/Ag heterostructures has been demonstrated which makes epitaxial silicene accessible to a broad number of *ex situ* diagnostic and potentially suitable to gated device configurations. The design of an effective encapsulation layer can be generally applied to any silicene layer regardless of the substrate. The effectiveness of the silicene encapsulation unambiguously resulted from registering the fingerprint of the silicene layer in the *ex situ* measured Raman spectrum of the Al_2O_3 capped silicene on Ag(111). This can be potentially used as a benchmark to assess the influence of the substrate or to recognize different superstructures in the vibrational properties of silicene. Hence, by combining experimental techniques with DFT calculations, it is possible to describe the silicene on Ag(111) system in terms of a sp^2/sp^3 hybridized form of silicon where a vertically distorted honeycomb lattice is induced by the substrate's constraints. The Raman spectrum reflects the multi-hybridized nature of silicene resulting from a buckling-induced distortion of a purely sp^2 hybridized structure. This sp^2/sp^3 character provokes an intrinsic disorder, which leads to the activation of Raman-inactive vibrational modes, whose intensity is a function of the amount and distribution of buckled Si atoms.

To date, buckled silicene structures have been experimentally reported on substrates with metallic character, including Ag(111) [14, 15], Ir(111) [17], and ZrB_2(0001) [16]. It is worth noting that similar results as those obtained on Ag(111) single crystal can be achieved also on Ag grown on mica substrates. Although in principle there is nothing different, there are some practical consequences. Indeed, the Ag on mica substrates are cheaper than Ag single crystals, but they can be also potentially used in device configuration by cleaving mica layers and etching the residual thin Ag substrate. However, accessing the electronic functionalities of silicene necessarily demand to bypass the metallic support. For this purpose, several theoretical works started to investigate alternate non-metallic substrates, whose lattice parameters could be compatible with 2D growth of Si. Recently, GaS [52], ZnS [53], BN [54, 55], and SiC(0001) [55] substrates have been reported as theoretical potential candidates. The purpose of the these works is to look for a non-metallic substrate which can concomitantly favor a 2D growth of Si and induce the honeycomb arrangement as a consequence of an inherent sp^2 bonding hybridization. To this scope, layered

graphite-like materials [56] with hexagonal atomic arrangement are expected to be promising candidates. Importantly, cleavage of the layered compounds does not create dangling bonds and, therefore, these materials are ideally suited as inert substrates for van der Waals epitaxy of weakly interacting films in the monolayer regime [57]. The electronic properties as well as the structural and chemical characteristics of layered materials make them appealing for a variety of applications and suitable for the synthesis of hybrid devices based on 2D materials, as widely reported in the recent literature [58, 59]. In this framework, an intriguing option as potential substrate is represented by MoS_2 which, today, is probably the best-known transition metal dichalcogenide.

Bibliography

[1] K. Takeda and K. Shiraishi, *Phys. Rev. B* **50**, 14916 (1994)

[2] S. Iijima, *Nature* **354**, 56 (1991)

[3] K. S. Novoselov, A. K. Geim, S. V. Morozov, D. Jiang, Y. Zhang, S. V. Dubonos, I. V. Grigorieva, and A. A. Firsov, *Science* **306**, 666 (2004)

[4] G. G. Guzman-Verri and L. C. Lew Yan Voon, *Phys. Rev. B* **76**, 075131 (2007)

[5] K. S. Novoselov, A. K. Geim, S. V. Morozov, D. Jiang, M. I. Katsnelson, I. V. Grigorieva, S. V. Dubonos, and A. A. Firsov, *Nature* **438**, 197 (2005)

[6] I. Milosevic, B. Nikolic, M. Damnjanovic, and M. Krcmar, *J. Phys. A Math. Gen.* **31**, 3625 (1998)

[7] S. Cahangirov, M. Topsakal, E. Aktürk, H. Sahin, and S. Ciraci, *Phys. Rev. Lett.* **102**, 236804 (2009)

[8] M. Houssa, G. Pourtois, V. V. Afanas'ev, and A. Stesman, *Appl. Phys. Lett.* **97**, 112106 (2010)

[9] C. C. Liu, W. Feng, and Y. Yao, *Phys. Rev. Lett.* **107**, 076802 (2011)

[10] C. Leandri, H. Oughaddou, B. Aufray, J. M. Gay, G. Le Lay, A. Ranguis, and Y. Garreau, *Surf. Sci.* **601**, 262 (2007)

[11] P. De Padova, P. Perfetti, B. Olivieri, C. Quaresima, C. Ottaviani, and G. Le Lay, *J. Phys. Condens. Matter* **24**, 223001 (2012)

[12] B. Lalmi, H. Oughaddou, H. Enriquez, A. Kara, S. Vizzini, B. Ealet, and B. Aufray, *Appl. Phys. Lett.* **97**, 223109 (2010)

[13] G. Le Lay, P. De Padova, A. Resta, T. Bruhn, and P. Vogt, *J. Phys. D Appl. Phys.* **45**, 392001 (2012)

[14] P. Vogt, P. De Padova, C. Quaresima, J. Avila, E. Frantzeskakis, M. C. Asensio, A. Resta, B. Ealet, and G. Le Lay, *Phys. Rev. Lett.* **108**, 155501 (2012)

[15] C. L. Lin, R. Arafune, K. Kawahara, N. Tsukahara, E. Minamitani, Y. Kim, N. Takagi, and M. Kawai, *Appl. Phys. Express* **5**, 045802 (2012)

[16] A. Fleurence, R. Friedlein, T. Ozaki, H. Kawai, Y. Wang, and Y. Yamada-Takamura, *Phys. Rev. Lett.* **108**, 245501 (2012)

[17] L. Meng, Y. Wang, L. Zhang, S. Du, R. Wu, L. Li, Y. Zhang, G. Li, H. Zhou, W. A. Hofer, and H. J. Gao, *Nano Lett.* **13**, 685 (2013)

[18] A. Resta, T. Leoni, C. Barth, A. Ranguis, C. Becker, T. Bruhn, P. Vogt, and G. Le Lay, *Sci. Rep.* **3**, 2399 (2013)

[19] P. Y. Huang, C. S. Ruiz-Vargas, A. M. van der Zande, W. S. Whitney, M. P. Levendorf, J. W. Kevek, S. Garg, J. S. Alden, C. J. Hustedt, Y. Zhu, J. Park, P. L. McEuen, and D. A. Muller, *Nature* **469**, 389 (2011)

[20] H. Jamgotchian, Y. Colignon, N. Hamzaoui, B. Ealet, J. Y. Hourau, B. Aufray, and J. P. Biberian, *J. Phys. Condens. Matter* **24**, 172001 (2012)

[21] H. Enriquez, S. Vizzini, A. Kara, B. Lalmi, and H. Oughaddou, *J. Phys. Condens. Matter* **24**, 314211 (2012)

[22] B. Feng, Z. Ding, S. Meng, Y. Yao, X. He, P. Cheng, L. Chen, and K. Wu, *Nano Lett.* **12**, 3507 (2012)

[23] L. Chen, H. Li, B. Feng, Z. Ding, J. Qiu, P. Cheng, K. Wu, and S. Meng, *Phys. Rev. Lett.* **110**, 085504 (2013)

[24] R. Arafune, C. L. Lin, R. Nagao, M. Kawai, and N. Takagi, *Phys. Rev. Lett.* **110**, 229701 (2013)

[25] L. Chen, C. C. Liu, B. Feng, X. He, P. Cheng, Z. Ding, S. Meng, Y. Yao, and K. Wu, *Phys. Rev. Lett.* **110**, 229702 (2013)

[26] P. De Padova, P. Vogt, A. Resta, J. Avila, I. Razado-Colambo, C. Quaresima, C. Ottaviani, B. Olivieri, T. Bruhn, T. Hirahara, T. Shirai, S. Hasegawa, M. C. Asensio, and G. Le Lay, *Appl. Phys. Lett.* **102**, 163106 (2013)

[27] R. Arafune, C. L. Lin, K. Kawahara, N. Tsukahara, E. Minamitani, Y. Kim, N. Takagi, and M. Kawai, *Surf. Sci.* **608**, 297 (2013)

[28] K. R. Knox, S. Wang, A. Morgante, D. Cvetko, A. Locatelli, T. O. Mentes, M. A. Nino, P. Kim, and R. M. Osgood Jr., *Phys. Rev. B* **78**, 201408 (2008)

[29] J. Avila, P. De Padova, S. Cho, I. Colambo, S. Lorcy, C. Quaresima, P. Vogt, A. Resta, G. Le Lay, and M. C. Asensio, *J. Phys. Condens. Matter* **25**, 262001 (2013)

[30] S. Y. Zhou, G. H. Gweon, A. V. Fedorov, P. N. First, W. A. de Heer, D. H. Lee, F. Guinea, A. H. Castro Neto, and A. Lanzara, *Nature Mater.* **6**, 770 (2007)

[31] K. S. Novoselov, *Nature Mater.* **6**, 720 (2007)

[32] A. Bendounan, Y. Fagot Revurat, B. Kierren, F. Bertran, V. Y. Yurov, and D. Malterre, *Surf. Sci.* **496**, L43 (2002)

[33] A. L. Vazquez de Parga, F. Calleja, B. Borca, M. C. G. Passeggi Jr., J. J. Hinarejos, F. Guinea, and R. Miranda, *Phys. Rev. Lett.* **100**, 056807 (2008)

[34] A. H. Castro Neto, F. Guinea, N. M. R. Peres, K. S. Novoselov, and A. K. Geim, *Rev. Mod. Phys.* **81**, 109 (2009)

[35] Y. Zhang, V. W. Brar, F. Wang, C. Girit, Y. Yayon, M. Panlasigui, A. Zettl, and M. F. Crommie, *Nature Phys.* **4**, 627 (2008)

[36] G. M. Rutter, J. N. Crain, N. P. Guisinger, T. Li, P. N. First, and J. A. Stroscio, *Science* **317**, 219 (2007)

[37] L. Chen, C. C. Liu, B. Feng, X. He, P. Cheng, Z. Ding, S. Meng, Y. Yao, and K. Wu, *Phys. Rev. Lett.* **109**, 056804 (2012)

[38] P. De Padova, J. Avila, A. Resta, I. Razado-Colambo, C. Quaresima, C. Ottaviani, B. Olivieri, T. Bruhn, P. Vogt, M. C. Asensio, and G. Le Lay, *J. Phys. Condens. Matter* **25**, 382202 (2013)

[39] C. L. Lin, R. Arafune, K. Kawahara, M. Kanno, N. Tsukahara, E. Minamitani, Y. Kim, M. Kawai, and N. Takagi, *Phys. Rev. Lett.* **110**, 076801 (2013)

[40] Z. G. Shao, X. S. Ye, L. Yang, and C. L. Wang, *J. Appl. Phys.* **114**, 093712 (2013)

[41] B. Huang, H. J. Xiang, and S. H. Wei, *Phys. Rev. Lett.* **111**, 145502 (2013)

[42] M. Houssa, E. Scalise, K. Sankaran, G. Pourtois, V. V. Afanas'ev, and A. Stesmans, *Appl. Phys. Lett.* **98**, 223107 (2011)

[43] J. Sivek, H. Sahin, B. Partoens, and F. M. Peeters, *Phys. Rev. B* **87**, 085444 (2013)

[44] I. Olefjord, H. J. Mathieu, and P. Marcus, *Surf. Interface Anal.* **15**, 681 (1990)

[45] R. Vali and S. M. Hosseini, *Comp. Mat. Sci.* **29**, 138 (2004)

[46] R. B. Laughlin and J. D. Joannopoulos, *Phys. Rev. B* **16**, 2942 (1977)

[47] G. Faraci, S. Gibilisco, P. Russo, and A. R. Pennisi, *Phys. Rev. B* **73**, 033307 (2006)

[48] I. F. Crowe, M. P. Halsall, O. Hulko, A. P. Knights, R. M. Gwilliam, M. Wojdak, and A. J. Kenyon, *J. Appl. Phys.*, **109**, 083534 (2011)

[49] A. C. Ferrari, J. C. Meyer, V. Scardaci, C. Casiraghi, M. Lazzeri, F. Mauri, S. Piscanec, D. Jiang, K. S. Novoselov, S. Roth, and A. K. Geim, *Phys. Rev. Lett.* **97**, 187401 (2006)

[50] S. Shaik, A. Shurki, D. Danovich, and P. C. Hiberty, *J. Am. Chem. Soc.* **118**, 666 (1996)

[51] J. B. Renucci, R. N. Tyte, and M. Cardona, *Phys. Rev. B* **11**, 3885 (1975)

[52] Y. Ding and Y. Wang, *Appl. Phys. Lett.* **103**, 043114 (2013)

[53] M. Houssa, B. van den Broek, E. Scalise, G. Pourtois, V. V. Afanas'ev, and A. Stesmans, *Phys. Chem. Chem. Phys.* **15**, 3702 (2013)

[54] L. Li, X. Wang, X. Zhao, and M. Zhao, *Phys. Lett. A* **377**, 2628 (2013)

[55] H. Liu, J. Gao, and J. Zhao, *J. Phys. Chem. C* **117**, 10353 (2013)

[56] G. Gao, W. Gao, E. Cannuccia, J. Taha-Tijerina, L. Balicas, A. Mathkar, T. N. Narayanan, Z. Liu, B. K. Gupta, J. Peng, Y. Yin, A. Rubio, and P. M. Ajayan, *Nano Lett.* **12**, 3518 (2012)

[57] Y. Shi, W. Zhou, A. Y. Lu, W. Fang, Y. H. Lee, A. L. Hsu, S. M. Kim, K. K. Kim, H. Y. Yang, L. J. Li, J. C. Idrobo, and J. Kong, *Nano Lett.* **12**, 2784 (2012)

[58] R. V. Kashid, D. J. Late, S. S. Chou, Y. K. Huang, M. De, D. S. Joag, M. A. More, and V. P. Dravid, *Small* **9**, 2730 (2013)

[59] D. J. Late, B. Liu, J. Luo, A. Yan, H. S. S. Ramakrishna Matte, M. Grayson, C. N. R. Rao, and V. P. Dravid, *Adv. Mater.* **24**, 3549 (2012)

Chapter 6

Conclusions

> When a scientist doesn't know the answer to a problem, he is ignorant. When he has a hunch as to what the result is, he is uncertain. And when he is pretty damn sure of what the result is going to be, he is still in some doubt
>
> R. P. Feynman

In the present thesis the fundamental properties of alternate channel materials to (bulk) silicon have been studied. Formidable challenges have to be faced in order to integrate novel materials in the classical metal-oxide-semiconductor field effect transistor (MOSFET) device concept. Indeed, many constraints of physical, technological but even economical nature should be taken into account when considering which material will replace silicon in the future. In this framework, an incessant research is nowadays able to provide different alternate solutions. Here, two potential and paradigmatic candidates have been chosen and studied. They are $In_{0.53}Ga_{0.47}As$ and silicene. The former represents the natural evolution of GaAs, whose study started in the early days of micro-electronics concomitantly with silicon and germanium. In the *More Moore* view, it will probably symbolize one of the most reliable successor of silicon because of the higher electron mobility and nearly full compatibility with silicon-based processing. On the other hand, silicene represents an intriguing bet. Indeed, silicene does not exist in nature and therefore it constitutes an excellent example of "material engineering" with structural and electronic properties tunable *ad hoc* for a determined purpose. Moreover, silicene could further extend the scaling either in a *More Moore* or in a *More than Moore* view. Indeed, since a successor of the Si MOSFET for future high performance logic will most likely be an entirely new device based on an alternative operating principle, presumably, it will be not sufficient to keep the MOSFET as the basic building block for integrated circuits (ICs) and only change the channel material. Of course, these candidates have different timeline with respect to the integration and exploitation in industry. In a short time $In_{0.53}Ga_{0.47}As$-based

ICs will become reality while, today, a silicene FET does not exist yet. However, future $In_{0.53}Ga_{0.47}As$ MOSFETs and high performance logic ICs will suffer from the same fundamental problems as Si MOSFETs and CMOS ICs, i.e. gate and source-to-drain tunneling, variability, parasitic resistances and capacitances, and power consumption. The best channel material does not help if the external parasitics dominate FET operation. In this framework, $In_{0.53}Ga_{0.47}As$ (but also Ge) is a mid-term option which will probably extend Moore's law until two-dimensional (2D) materials will likely represent the ultimate scaling.
The main problem related to III-V semiconductors, in particular $In_{0.53}Ga_{0.47}As$, is represented by interface realization. For this purpose, two different $In_{0.53}$-$Ga_{0.47}As$ reconstructions showing different chemical terminations have been investigated at the interface with a high-κ oxide as Al_2O_3. Scanning Tunneling Microscopy and Spectroscopy (STM and STS) allowed to atomically characterize both reconstructions thus confirming the pinned Fermi level conditions of both surfaces, according to the theoretical models. Al_2O_3 deposition by Molecular Beam Epitaxy (MBE) can adequately passivate the dangling bonds causing Fermi level pinning thus alleviating it. Benefiting from comparison with common *ex situ* process, a whole *in situ* approach allows to chemically control the oxide composition at the interface and to verify thermal stability of the so obtained Fermi level unpinning. After annealing at 200 °C Fermi level pinning is indeed restored in a different extent depending on the surface reconstructions. The cause of Fermi level unpinning can be found in the presence of positive oxide charges or electric dipoles in the as-grown oxide. Therefore, the presence of positive charges can be exploited to unpin the interface Fermi level. $In_{0.53}Ga_{0.47}As$ can be successfully used as active channel material provided that a close control of the interface realization and suitable oxide deposition are considered. As a partial conclusion, engineering an unpassivated $In_{0.53}Ga_{0.47}As$ interface has been achieved by combining *in situ* MBE growth and treatment along with scanning tunneling investigations of the local structure and electronic properties.
On the other hand, since the first reports on the successful isolation of a stable monolayer of graphene, special efforts have been invested in the exploration of similar materials with novel properties resulting from their ultra-thin 2D nature. Those alternate materials have the potential to bypass some of the hurdles existing in the use of graphene in contemporary electronics, i.e. incompatibility with present day silicon technology and lack of an energy bandgap, which is essential for all semiconductor devices. In this framework, silicene is a completely new material which has been predicted to exist in its freestanding fashion by theory and discovered on supporting metallic substrates as Ag(111), Ir(111), and ZrB_2(0001) by experiments. In particular, silicene on Ag(111) has been proved to form several phases with different structural and electronic properties. Combining different experimental characterization techniques, such as STM/STS, X-ray Photoelectron Spectroscopy, and Raman, with theoretical modelling a complex multi-phase scenario has been drawn resulting in a much

more complicated picture with respect to graphene. Of course, this scenario is far from being exhaustively understood and a vibrant debate is currently in progress to elucidate the intimate aspects of silicene. The experience acquired on Al_2O_3 at the interface with $In_{0.53}Ga_{0.47}As$ allowed to encapsulate silicene thus preventing its oxidation in ambient air condition. This encapsulation design shows the advantage of being applicable to any silicene configuration irrespective of the supporting substrate. On the other hand, the survey for alternate substrates and, in particular, for non-metallic ones is nowadays the main challenge to face. Indeed, in contrast to graphene, silicene is strictly dependent on its substrate and disentangling silicene from a metal template is not an easy task. Overall, in this exploratory effort, some relevant outcomes have been achieved including structural identification via STM and Raman, electronic characterization by STS, and encapsulation in a device-oriented perspective.
In conclusion, while III-V semiconductors are a viable option in the near future, it is very likely that the future will be dominated by 2D materials either in their isolated form or integrated in artificially conceived heterostructures. Indeed, the rapid evolution of graphene is a clear evidence of the potentiality that could be achieved in 2D materials. Furthermore, they show impressive values of carrier mobilities and they are also the thinnest possible channel thereby representing ideal candidates for *More Moore* view, but they also appear versatile to other device concepts in a *More than Moore* extended approach. Therefore, it is possible to expect that 2D materials will remain a hot topic and that these materials will find their place in future electronics. Finally, it could seem a twist of fate if the incessant survey of possible alternate material to silicon had to end with silicon again but in its 2D allotropic form.

Publications

1. Polychronis Tsipas, Spyros Kassavetis, Dimitra Tsoutsou, Evangelia Xenogiannopoulou, Evangelos Golias, Sigiava A. Giamini, **Carlo Grazianetti**, Daniele Chiappe, Alessandro Molle, Marco Fanciulli, and Athanasios Dimoulas, "Evidence for graphite-like hexagonal AlN nanosheets epitaxially grown on single crystal Ag(111)", *Appl. Phys. Lett.*, accepted;
2. Daniele Chiappe, Emilio Scalise, Eugenio Cinquanta, **Carlo Grazianetti**, Bas van den Broek, Marco Fanciulli, Michel Houssa, and Alessandro Molle, "Two-dimensional honeycomb Si nanosheets on a MoS_2 surface", *Adv. Mater.*, accepted;
3. **Carlo Grazianetti**, Daniele Chiappe, Eugenio Cinquanta, Grazia Tallarida, Marco Fanciulli, and Alessandro Molle, "Exploring the morphological and electronic properties of silicene superstructures", *Appl. Surf. Sci.*, in press;
4. Michel Houssa, Bas van den Broek, Emilio Scalise, Benedicte Ealet, Geoffrey Pourtois, Daniele Chiappe, Eugenio Cinquanta, **Carlo Grazianetti**, Marco Fanciulli, Alessandro Molle, Valeri V. Afanas'ev, and Andre Stesmans, "Theoretical aspects of graphene-like group IV semiconductors", *Appl. Surf. Sci.*, in press;
5. Emilio Scalise, Eugenio Cinquanta, Michel Houssa, Bas van den Broek, Daniele Chiappe, **Carlo Grazianetti**, Geoffrey Pourtois, Benedict Ealet, Alessandro Molle, Marco Fanciulli, Valeri V. Afanas'ev, and Andre Stesmans, "Vibrational properties of epitaxial silicene layers on (111) Ag", *Appl. Surf. Sci.*, in press;
6. Alessandro Molle, Daniele Chiappe, Eugenio Cinquanta, **Carlo Grazianetti**, Marco Fanciulli, Emilio Scalise, Bas van den Broek, and Michel Houssa, "Structural and chemical stabilization of the epitaxial silicene", *ECS Trans.* **58**, 217 (2013);
7. Eugenio Cinquanta, Emilio Scalise, Daniele Chiappe, **Carlo Grazianetti**, Bas van den Broek, Michel Houssa, Marco Fanciulli, and Alessandro Molle, "Getting through the nature of silicene: A sp^2-sp^3 Two-dimensional silicon nanosheet", *J. Phys. Chem. C* **117**, 16719 (2013);

8. Alessandro Molle, **Carlo Grazianetti**, Daniele Chiappe, Eugenio Cinquanta, Elena Cianci, Grazia Tallarida, and Marco Fanciulli, "Hindering the oxidation of silicene with non-reactive encapsulation", *Adv. Func. Mater.* **23**, 4340 (2013);

9. **Carlo Grazianetti**, Alessandro Molle, Grazia Tallarida, Sabina Spiga, and Marco Fanciulli, "Effect of electric dipoles on the Fermi level positioning at the interface between ultra-thin Al_2O_3 films and differently reconstructed $In_{0.53}Ga_{0.47}As(001)$ surfaces", *J. Phys. Chem. C* **116**, 18746 (2012);

10. Daniele Chiappe, **Carlo Grazianetti**, Grazia Tallarida, Marco Fanciulli, and Alessandro Molle, "Local electronic properties of corrugated silicene phases", *Adv. Mater.* **24**, 5088 (2012);

11. Luca Lamagna, Alessandro Molle, Claudia Wiemer, Sabina Spiga, **Carlo Grazianetti**, Gabriele Congedo, and Marco Fanciulli, "Atomic layer deposition of Al-doped ZrO_2 thin films as gate dielectric for $In_{0.53}Ga_{0.47}As$", *J. Electrochem. Soc.* **159**, H220 (2012);

12. Alessandro Molle, Luca Lamagna, **Carlo Grazianetti**, Guy Brammertz, Clement Merckling, Matty Caymax, and Marco Fanciulli, "Reconstruction dependent reactivity of As-decapped $In_{0.53}Ga_{0.47}As(001)$ surfaces and its influence on the electrical quality of the interface with Al_2O_3 grown by atomic layer deposition", *Appl. Phys. Lett.* **99**, 193505 (2011);

13. Luca Lamagna, Alessandro Molle, Claudia Wiemer, Sabina Spiga, **Carlo Grazianetti**, and Marco Fanciulli, "Atomic layer deposition of Al-doped ZrO_2 thin films for advanced gate stack on III-V substrates", *ECS Trans.* **35**, 431 (2011).

Conferences

1. **Carlo Grazianetti**, Daniele Chiappe, Eugenio Cinquanta, Elena Cianci, Grazia Tallarida, Marco Fanciulli, and Alessandro Molle, *"Hindering the oxidation of silicene with non-reactive encapsulation"*, Flatlands – Beyond Graphene 2013, Bremen, Germany, 17-21 June 2013 (Poster);

2. **Carlo Grazianetti**, Daniele Chiappe, Eugenio Cinquanta, Grazia Tallarida, Marco Fanciulli, and Alessandro Molle, *"Morphological and electronic properties of silicene grown on Ag(111)"*, E-MRS 2013, Strasbourg, France, 27-31 May 2013 (Oral);

3. **Carlo Grazianetti**, Daniele Chiappe, Eugenio Cinquanta, Elena Cianci, Grazia Tallarida, Marco Fanciulli, and Alessandro Molle, *"Hindering the oxidation of silicene with non-reactive encapsulation"*, E-MRS 2013, Strasbourg, France, 27-31 May 2013 (Poster);

4. **Carlo Grazianetti**, Grazia Tallarida, Sabina Spiga, Marco Fanciulli, and Alessandro Molle, *"Effect of electric dipoles on Fermi level positioning at the interface between* Al_2O_3 *and* $In_{0.53}Ga_{0.47}As$*"*, E-MRS 2013, Strasbourg, France, 27-31 May 2013 (Poster);

5. **Carlo Grazianetti**, Grazia Tallarida, Sabina Spiga, Marco Fanciulli, and Alessandro Molle, *"Scanning tunneling microscopy/spectroscopy study of* Al_2O_3 *ultra-thin films on differently reconstructed* $In_{0.53}Ga_{0.47}As(001)$ *surfaces"*, ICN+T 2012, Paris, France, 23-27 July 2012 (Student Grant awarded) (Oral);

6. **Carlo Grazianetti**, Daniele Chiappe, Grazia Tallarida, Marco Fanciulli, and Alessandro Molle, *"In-situ characterization of silicon nanosheets grown on Ag(111)"*, ICN+T 2012, Paris, France, 23-27 July 2012 (Student Grant awarded) (Poster).

Acknowledgements

Many sincere thanks to all who contributed to this work. In particular, I would like to acknowledge Prof. Marco Fanciulli for the chance to do research in his group. I want to express my gratitude to Prof. Guy Le Lay, who agreed to referee this thesis, for fruitful discussions and suggestions about silicene.
I would like to thank my post-doc lab-partners and good friends Luca, Daniele, and Eugenio. I am especially indebted with Daniele for the almost three years spent together working on MBE and STM. I learned a lot and it has been a pleasure to make experiments with him and to share funny moments together.
Special thanks to the (by now former) PhD students Andrea, Guido, and Roberto for their advices. I would give my deep thanks to Grazia and Matteo for technical assistance with the STM and cryogenic set-up. I would like to thank Andrea and Paolo, those who showed me the world of STM for the first time.
I want to acknowledge collaborations with IMEC and with the consortium of 2D Nanolattices. In particular, thanks to Guy Brammertz, Clement Merckling, Guy Le Lay, Thanasis Dimoulas, Michel Houssa, and Emilio Scalise.
Last, but not least, I want to give a special thank to Alessandro for the supervision and the help with his countless advices throughout all these three years and also for proofreading this thesis.
I want to express my gratitude to everyone else from MDM not mentioned by name. I would like to thank the lunch-mates Andrea, Antonio, Daniele, Eugenio, Flavio, Federico, and Mario for "thoughtful" conversations and well-deserved distractions.
Thanks to my family and to my friends for the important things in life.